Ultra-fast Magnetic Resonance Imaging of intruders sinking into a concentrated suspension

Performed at the Laboratory of Energy Science and Engineering, ETH Zürich

Nikolay Kirov

TU Delft

Ultra-fast Magnetic Resonance Imaging of intruders sinking into a concentrated suspension

Performed at the Laboratory of Energy Science and Engineering, ETH Zürich

by

Nikolay Kirov

to obtain the degree of Master of Science
at the Delft University of Technology,
to be defended publicly on Tuesday January 18, 2019 at 1:00 PM.

Student number:	4278879	
Project duration:	November 27, 2017 – January 18, 2019	
Thesis committee:	Prof. dr. ir. B. P. Tighe,	TU Delft, supervisor
	Prof. dr. ir. C. Poelma,	TU Delft
	Dr. Ir. W. -P. Breugem,	TU Delft

This thesis is confidential and cannot be made public until January 17, 2019.

TU Delft

Contents

List of Figures

List of Tables

Acknowledgements

This work would not have been possible without the close aid and assistance of my daily advisers in the Laboratory of Energy Science and Engineering, D-MAVT, ETH Zürich - Christopher McLaren (ETH Zürich) and Alexander Penn (ETH Zürich), and without the constructive feedback of my supervisors Prof. Dr. Christoph Müller (ETH Zürich) and Prof. Dr. Brian Tighe (TU Delft). Furthermore, I sincerely want to thank Nicholas Conzelmann (ETH Zürich) for his critical comments, remarkable insights and ideas about the project.

Abstract

Surprisingly, liquid media of dispersed dry micron-sized particles can generate tremendous impact resistance, can grow solid protrusions when acoustically-vibrated and can cause a range of other peculiar phenomena to objects sinking in their interior, even though their appearance essentially remains 'liquid-like' [1] [2] [3]. These heterogeneous mixtures of undissolved particles, referred to as suspensions, can be found all around us: e.g. in paints, blood, mudslides, landslides, etc [2]. Moreover, due to some suspensions' shear-thickening behaviour their use has been investigated for liquid-like body armor applications, new damper designs and many more [1]. Yet, the core physical mechanism of their behaviour in its various regimes is still not completely understood. This thesis work employs the novel ultra-fast Magnetic Resonance Imaging methodology proposed by Alexander Penn, also a member of the ETH Zürich laboratory from which this work originates, to image non-intrusively into a shear-thickening suspension of cornstarch and water while a spherical intruder impacts and settles in its interior. First off, by fitting a rigid steel wire inside the settling object and imaging a marker on top of it with a high-speed camera, behaviours similar to those observed by von Kann *et al.* are evident: the intruder oscillates around a terminal velocity in the bulk of the suspension and experiences stop-and-go cycles near the container base. This act, however, inherently restricts motion by allowing the intruder to move only in the vertical direction [2]. Therefore, we utilize 1D and 2D MR imaging to obtain information about the intruder's horizontal and undisturbed vertical motion to draw conclusions that the object exhibits similar oscillations in amplitude and frequency also in the transverse component. In addition to those, we perform 2D velocity-encoded MRI scans to obtain the velocity and shear rate fields with sufficient time resolution to capture the suspension behaviour at the relevant phenomenological regimes. The data suggested that, on comparison with reference rheology experiments, the shear rates during the terminal velocity oscillations, resultant from the fluid inertia around the object as it settles, appear to be in close proximity to the critical shear rate for discontinuous shear thickening (DST, or an orders-of-magnitude jump in stress). To continue, 1D MRI measurements revealed a phenomenon new to us to be visible just after the impact: upon increasing mass, size, and drop height of intruders, the transient oscillations which transition to stable bulk oscillations were found to transform into several distinct stop-and-go cycles very much alike those that occur close to the container bottom. A qualitative physical mechanism was proposed based on the dependencies found in these behaviours. Last but not least, the effects of size while keeping the same buoyancy ratio were studied qualitatively. Direct evidence from all executed experiments confirmed secondary stable bulk oscillation regions for objects of larger size.

1 Introduction and Background Overview

Concentrated granular suspensions are heterogeneous mixtures in which the dispersed rigid particles do not dissolve, but get suspended throughout the bulk of the continuous phase. The particle sizes of such suspensions are larger than the colloidal scale, typically beyond 100 nm. Furthermore, in contrast to colloids, the particles in granular suspensions are large enough to sediment over time when undisturbed. They are extensively observed in our daily lives, e.g. they are seen in the cosmetic, food, pharmaceutical and paint industries, and also make a striking appearance in nature as avalanches, landslides, muddy water and blood [1] [2].

The combined behaviour of a suspension can be much more complex and counter-intuitive than the behaviour of the individual materials which comprise it; for instance, the resistance of a suspension to flow can exhibit dramatic change depending on the strength of the driving force. Therefore, two types of peculiar behaviour observed in suspensions are crucial to understand: shear-thinning and shear-thickening, both of which could be useful but also unfavorable, depending on the application. The former is the behaviour of paints (suspensions of micron-sized pigment particles) which flow easily when brushed, but resist flow when left to dry undisturbed. The latter is the exact opposite - the materials become more resistive when driven by a strong force, which is exactly the most evident behavioural regime of the cornstarch-water suspensions described in this work.

Observing these unique behaviours, researchers have been inspired to investigate the use of suspensions in applications ranging from ballistic woven fabrics for 'liquid/soft protective armor' to pipe cloggers for 'top kill' operations in overflowing oil wells (such as the BP Deepwater Horizon spill in the Gulf of Mexico in 2010) [3]. Speaking strictly of the soft protective armor applications, currently multi-layered armors with a front ceramic followed by an aramid fabric (Kevlar™) are most commonly employed worldwide against high velocity ammunition. The front ceramic layer shatters and spalls the bullet, while the intermediate Kevlar fabric dissipates the energy of both the bullet and the ceramic fragment [4]. Successful as Kevlar by itself is, tests of Kevlar formulated with colloidal suspensions have revealed a marked enhancement in performance [5]. According to studies performed at the University of Delaware, the velocity at which a 6.35 mm steel ball penetrates a single layer of Kevlar fabric is approximately 100 m/s, whereas the required velocity to penetrate Kevlar formulated with polymethyl-methacrylate colloidal particles is 150 m/s and the astonishing 250 m/s for a Kevlar layer enriched by silica colloids [1]. Even though the particles in concentrated granular suspensions are larger in scale than colloids, they also share this shear-thickening behaviour crucial for such protective armor applications and some are believed to be even more promising than colloids. These are just a few of the reasons why granular suspensions have grabbed the attention

of scientific and engineering societies - to learn how to control their behaviour, by taking advantage when it is useful and preventing it when it is unwanted. Even setting their practical importance aside, suspension behaviour is inherently interesting to scientists because it often defies our intuition [3].

To understand the physics of suspension performance we must first dig deep into the many factors that play a role. On the colloidal scale, effects such as van der Waals forces, Brownian motion, and electrostatic forces predominate and cause Non-Newtonian behaviour [6]. However, this work describes suspensions of larger characteristic dimensions of particles than the aforementioned colloids. Well, these still exhibit Non-Newtonian behaviour. One source is the tendency of particles to deform upon contact and therefore cause shear-rate dependent flow deviations. In essence, deformed particles store energy, which is the basic mechanism of visco-elastic behaviour [6]. Another source of non-Newtonian behaviour are hydrodynamic forces - if the particles are large enough, the inertial effects due to the flow deviation around them become more and more pronounced [6]. Because of this complex coupling between the liquid and the suspended particles, we still lack understanding of granular suspension behaviour in certain conditions. One reason for this is that, despite their deceptively simple components, they are inherently complex non-equilibrium systems. As a result of suspensions not being in thermodynamic equilibrium, their response to a driving force is sensitive to small alternation in the particle configuration, which can lead to strong hysteretic effects [3]. Furthermore, they are highly dissipative systems with complicated transient behavior, and yet most of the studies on suspensions have been performed under steady-state conditions, an approach which inherently restricts us to understanding only a certain fragment of the associated phenomena. And last but not least, they are highly sensitive to the particle packing fraction ϕ (defined as the volume of particles divided by the total volume of particles and liquid), meaning that small spatial heterogeneities can lead to considerable changes in behaviour and thus the underlying constitutive equations couple both compression and shear [3].

Before introducing the reader to the particular suspensions that are the main focus of this work, the study of flow of matter must be introduced. Specifically, this is the study of rheology, a particular branch of science that studies the flow behaviour of suspensions. Suspension rheology studies have been performed under steady-state conditions, measuring shear stress τ as a function of the applied shear rate $\dot{\gamma}$, and thus defining the viscosity of the suspension as

$$\eta_s = \frac{\mathrm{d}\tau}{\mathrm{d}\dot{\gamma}} \tag{1.1}$$

Physically, the viscosity characterizes the energy dissipation rate under shear. For Newtonian liquids, such as water, the viscosity is independent of $\dot{\gamma}$, i.e. it remains constant. In most suspensions, however, Non-Newtonian behaviours characterized by variable viscosity with shear rate are generally observed, as suggested earlier on. Shear-thinning behaviour refers to the decline of viscosity with shear rate, while shear-thickening identifies with the opposite behavior - an increase of viscosity with shear rate [7]. As a result, it has become a general practice in the scientific community to classify a suspension based on its most recognizable behaviour, even though often they exhibit all three of these types of behaviour under different shear rate regimes [1] [3].

The primary focus of this work will be on cornstarch-water suspensions, generalized as shear-thickening as this is their most pronounced and most recognizable behaviour [8]. This suspension shows by far the most counter-intuitive behaviour at elevated packing fractions. For instance, a quick search on the Internet shows people running on the surface of a large pool comprising of the suspension, only to sink once they stop in place. It is quite astonishing that a simple combination of water and such light particles like cornstarch can support normal forces large enough to counteract a full-grown man running on the suspension's surface and this has grabbed the attention of researchers around the globe (see figure 1.1) [9]. Another example which was found extremely interesting to scientists and people surfing the Internet, are the growing solid protrusions, referred to as 'cornstarch monsters', which occur at the suspension's surface when it is acoustically vibrated. This is illustrated in figure 1.2.

Figure 1.1: Running on a cornstarch-water suspension in a Youtube video: (https://youtu.be/Ja-6JtEZ7lk).

Figure 1.2: Non-Newtonian fluid on a speakercone. 'Cornstarch monsters' in a YouTube video: (https://youtu.be/3zoTKXXNQIU).

The shear-thickening behaviour in these suspensions appears in two variations - continuous shear-thickening (CST) and discontinuous shear-thickening (DST). The former occurs when the packing fraction is generally low and the increase in η_s with $\dot{\gamma}$ is gradual. Upon increasing the packing fraction to such an extent that random close packing (an empirical parameter characterizing the maximum volume fraction of solid objects resultant from a random packing) is approached, however, the spectacular DST phenomenon is observed - an orders-of-magnitude jump of the stationary

macroscopic stress when the strain rate crosses some threshold value [7] [2]. Cornstarch-water suspensions, possessing highly-irregular micron-sized particles, have been found to exhibit DST at packing fractions from 38% to 44% [10].

Multiple models have been developed to explain these types of shear-thickening. The sections to follow will provide a brief description on them and will attempt to summarize their advantages and short-comings. But before we can follow the models for shear-thickening we must first grasp the concept of jamming of granular systems which is of critical importance for this thesis.

1.1 Jamming of granular systems

While the most obvious examples for jamming remain the frustrating traffic jams we get ourselves into on highways exactly when we are in a hurry to go home after work, it is rather difficult to put those into the perspective of this work. Let us instead examine the flow of granular material into the constriction illustrated in figure 1.3. At a high enough volumetric flow rate we start to notice the formation of arch-like arrangements of granules near the opening, and if the particles are strong enough to bear the weight of their overhead neighbours, a restriction to the entire flow of particles occurs. In other words, the motion stops and the system reaches a 'jammed' state.

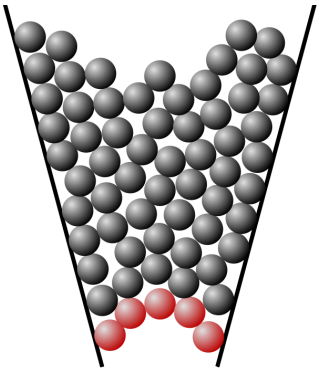

Figure 1.3: Granular jamming in a constriction

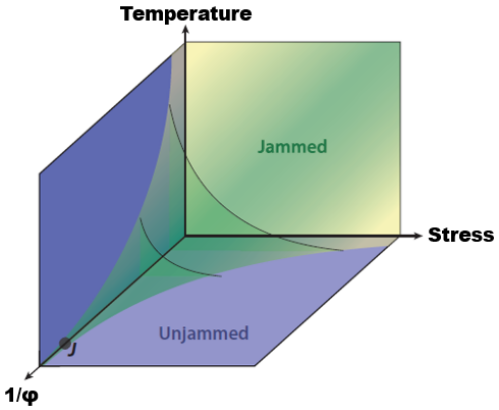

Figure 1.4: Unifying jamming phase diagram. Adapted from Liu and Nagel [11]. *Copyright 2010 Ann. Rev. of Cond. Mat. Phys.*

In the physical realm, the definition of a jammed material is a material which is structurally disordered but, in contrast to a Newtonian fluid, it possesses a yield stress. Such a material in the field of traditional condensed matter physics is essentially defined as an amorphous solid, while in the study of suspensions the use of the term 'jammed system' extends also to non-traditional materials such as granular systems, foams and colloids [12]. In fact, researchers have been originally comfortable enough to compare jamming with the freezing of a liquid into a glass, but in the case

of jamming the transformation occurs rather from a flowing to a solid-like jammed state [13]. Both phenomena involve amorphous systems of particles that lose their ability to flow when close to a certain threshold but remain amorphous nonetheless. In the present day, however, clear distinctions are found between the two transitional phenomena [11] whose details are not significant for this work.

Depending on the application, jamming can be useful but also harmful, hence the reason why every form of it requires our deep understanding in order to learn how to prevent it or control it. For instance, jammed grains in silos cause catastrophic failures, whereas in avalanches (a phenomenon of 'unjamming') the return of the equilibrium jammed state is favoured. The jamming phenomenon in granular matter poses fundamental challenges because there is no successful link or framework known that connects the microscopic grain level interactions to the macroscopic collective behaviour properties. Jamming is closely related to stress propagation, and therefore it depends on the nature of the stress source, i.e. it differs for materials subjected to shear and materials undergoing e.g. isotropic compression. Another factor adding to its complexity is the nature of the motion involved - it is important to distinguish the variance in the jamming process between systems of particles with finite kinetic energy in which motion is sustained, and systems at rest which are being slowly deformed [12].

The research into jamming experienced an enormous break-through when Liu and Nagel proposed a unifying phase diagram for all systems, even including the glass transition in supercooled liquids. This three-dimensional framework is shown in figure 1.4, comprising of three axes for temperature, shear stress and the reciprocal of the packing fraction [13] [14]. Examples of the functionality of this phase diagram are the capturing of solidification of liquids with low viscosity into a glass when the temperature is lowered, the transition to a rigid form of flowing foam when the applied stress is lowered, and the loss of the flow ability of colloidal suspensions when the packing fraction is increased. Research into all of the examples listed above show that upon varying a control parameter, the particular system is brought to a rigid phase while the structure does not suffer considerable change at the transition [11].

The proposed phase diagram has indeed been in good agreement with performed numerical simulations of particles that do not experience friction, however, the jamming transition behaves differently in systems comprised of frictional grains. This drawback lead Bi *et al.* to offer a modification to the diagram after executing experiments with frictional disk-shaped grains - specifically, a distinction was made between isotropic jamming and shear-jamming, the latter of which being essential for the understanding of the work of this thesis. For frictional grains, the experiments have

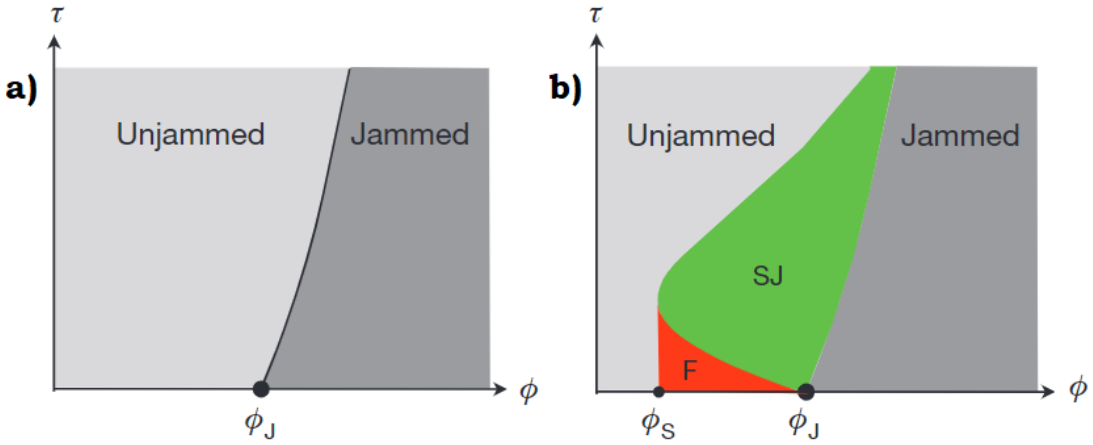

Figure 1.5: **a)** *Original Liu-Nagel jamming phase diagram in the $T = 0$ plane where the interface between the jammed and unjammed regions is the yield stress line.* **b)** *Generalized jamming diagram including the fragile (F) and shear-jammed (SJ) states. Adapted from* Bi *et al.* [15]. *Copyright 2011 Nature.*

shown that jamming can be induced by the application of shear stress at densities/packing fractions lower than the critical value at which isotropic or shear-free jamming is expected to occur. These prematurely jammed states experience a richer phenomenology than isotropically jammed states. For small applied shear stresses, a fragile state identifiable by a strong force network percolating in only one direction forms. At a certain minimum shear stress, however, robust shear-jammed states come into existence, possessing a strong force network which percolates in all directions [15]. According to Bi *et al.*, the transitions from unjammed to fragile states and from fragile to shear-jammed states are controlled by the statistically density-independent fractions of force-bearing grains. An important observation made was that the formation of fragile and shear-jammed states depends on the possibility of creating anisotropic contact networks in the grain structure. These networks or fabrics are essential to form a backbone for the stresses, and therefore the anisotropies of the stress tensor and the fabric tensor are intimately related in these states. Following from this observation, it was concluded that the minimum anisotropy in shear-jammed states vanishes as the density approaches the critical one from below, in a way which very much resembles an order-to-disorder transition [15].

1.2 Continuous shear-thickening

The continuous shear-thickening regime is essentially a smooth increase of the viscosity with the shear rate, and it generally occurs at low packing fractions. Two models have been proposed to explain this phenomenon, the first of the two involving an order-to-disorder transition in the particle arrangement [16], while the second focusing on the formation of particle clusters supported

by hydrodynamic forces [1]. While both models have been found promising, most contemporary research is focused on the hydrocluster model [3].

It is very well known that particles immersed in a liquid exert a force onto each other if they are in relative motion. This force comes from the fact that the motion of a particle imposes liquid flow deviations around it, which in turn influences the flow around other particles and their motion. The simplest case of two adjacent spherical particles of equal diameter d in a liquid with constant viscosity η was studied in the 1970s by Hocking [17]. When the particles move in the direction towards or away from each other with a relative velocity v_{rel} and interstitial spacing $\delta << d$, the force between them was exactly solved and given by equation 1.2. It essentially reads that at close range the hydrodynamic lubrication force is inversely proportional to the interstitial spacing between the surfaces of the particles and diverges to a singularity at the limit of $d \to 0$ (also shown in figure 1.6. Strictly speaking, when the two spheres are close to each other they are more difficult to separate [1].

$$F_{\mathrm{l}} = \frac{3\pi\eta d^2 v_{\mathrm{rel}}}{8\delta} \tag{1.2}$$

Observing figure 1.7 where the particles are in shearing motion relative to each other, we see that their trajectories can become coupled due to these hydrodynamic interactions and correlated 'orbits' tend to form around reference particles. Short-range hydrodynamics simulations of concentrated suspensions have shown that at high shear rates, particles close enough to each other remain strongly correlated, much resembling the closed trajectories seen in dilute suspensions. These flow-induced higher density groupings are known as hydroclusters because of the higher concentration of particles in them. Inside such clusters the fluid is under greater stress, leading to an increase in energy dissipation and hence higher local suspension viscosity [1].

A more detailed explanation on the hydrocluster mechanism requires first a definition of the Péclet number, i.e. the relation between flow shear rate and the particle's characteristic time scale of diffusion $t_d = d^2/D_0$ (defined as the time it takes for the particle to diffuse the distance of its radius), where D_0 is the diffusivity coefficient [1]. Note that in the thermal energy term $k_{\mathrm{B}}T$, k_{B} stands for the Boltzmann's constant and T is the temperature.

$$Pe = \frac{\dot{\gamma} d^2}{D_0} \qquad \text{, where } D_0 = \frac{k_{\mathrm{B}}T}{6\pi\mu d} \tag{1.3}$$

Figure 1.8 very clearly shows the microstructure undergoing all three sets of flow behaviour during colloidal dispersion - Newtonian equilibrium state, shear-thinning and shear-thickening. The

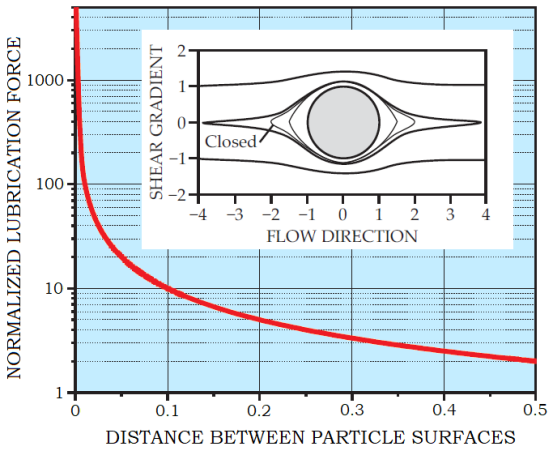

Figure 1.6: Required normalized lubrication force in order to drive two particles together at constant velocity. Adapted from Wagner and Brady [1]. *Copyright 2009 Physics Today.*

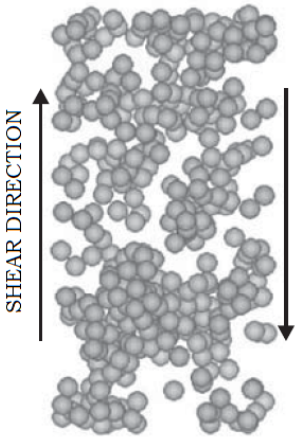

Figure 1.7: Particles in close proximity are being coupled by hydrodynamic interactions in simple shear flow. Adapted from Wagner and Brady [1]. *Copyright 2009 Physics Today.*

first ($Pe << 1$) is a result of stochastic and inter-particle forces (electrostatic and van der Waals forces) at balance, and it is not influenced by the hydrodynamics. Upon increasing the shear flow rate ($Pe \approx 1$), the particles rearrange themselves to reduce their interactions so that they can experience less resistance, following the formation of anisotropic microstructure, and therefore a reduction in viscosity. At even higher rates of shear ($Pe >> 1$), particles are driven closely together due to the high stresses and the lubrication hydrodynamics dominates: orbits of clusters are formed, the energy dissipation grows, and the shear-thickening behaviour develops [1].

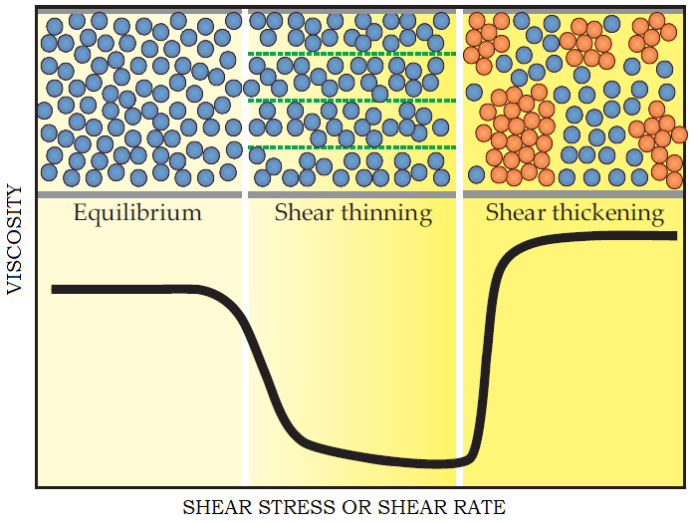

Figure 1.8: Change in microstructure. Adapted from Wagner and Brady [1]. *Copyright 2009 Physics Today.*

Hydroclustering has indeed been found to be in agreement with experimental observations and numerical simulations explaining the continuous shear-thickening regime occurring in moderate

packing fractions. However, the model was found to predict a rise in stresses only up to a factor of 2, and has been therefore been deemed insufficient to explain the sudden order-of-magnitude jump in those stresses during DST at higher local packing fractions by itself [18] [19].

1.3 Discontinuous shear-thickening

Some dense suspensions of particles are seen to exhibit discontinuous shear-thickening behaviour, i.e. orders of magnitude rise in viscosity upon exceeding a certain critical threshold shear stress. A couple of decades ago Bender *et al.* found that the DST process is completely reversible [20]. Since then the newly developed experimental techniques for probing the dynamical structure of the suspensions under shear in situ (such as the x-ray, MRI and neutron-scattering techniques) and the increased computational power (enabling faster simulations, larger system sizes and higher number of particles) have lead to significant progress on DST. But nonetheless, doubts have still remained on the very fundamental question asking what exactly is the main reason for the observed dramatic increase in shear stress during DST [19].

In a review by Brown and Jaeger, they argue that the DST regime is associated with a specific range of critical stresses $\tau_{\min}$ and $\tau_{\max}$ which are roughly independent of the packing fraction. It is illustrated in figure 1.9 that the former is the trigger for the shear-thickening regime, while the latter is the limit of DST above which shear-thinning, cracking and break-up of the tested cornstarch-glycerol-water suspension would take place [19]. The same representative rheological data plotted in the figure also shows that above a certain critical packing fraction ϕ_c, the system already possesses a yield stress like a solid, a property corresponding to a jamming transition [19]. This critical packing fraction very much depends on parameters such as nonsphericity and surface roughness of the particles - the higher these are, the lower the threshold ϕ_c [18].

Both the hydrocluster and the order-to-disorder transition mechanisms fall short in explaining the abrupt rise in stresses during DST. It does seem likely that hydroclustering is the source for the onset of shear-thickening in its gradual phase, yet the extremely high stresses observed in DST are too large to be solely due to lubrication forces. Brown and Jaeger suggested that a better explanation for DST are fabrics of stress paths that span the system and support normal stresses of similar magnitude as the shear stress [21] [19]. Fall *et al.*, on the other hand, associated the DST behaviour to a re-entrant jamming transition, stating that the onset of dilatancy during shear leads to a system wide jamming and a sudden rise in viscosity [8]. This mechanism of dilatancy was taken further by Brown and Jaeger to successfully predict the lower and upper shear stress bounds of shear-thickening (but not the thickening slopes) by employing the idea that dilation of

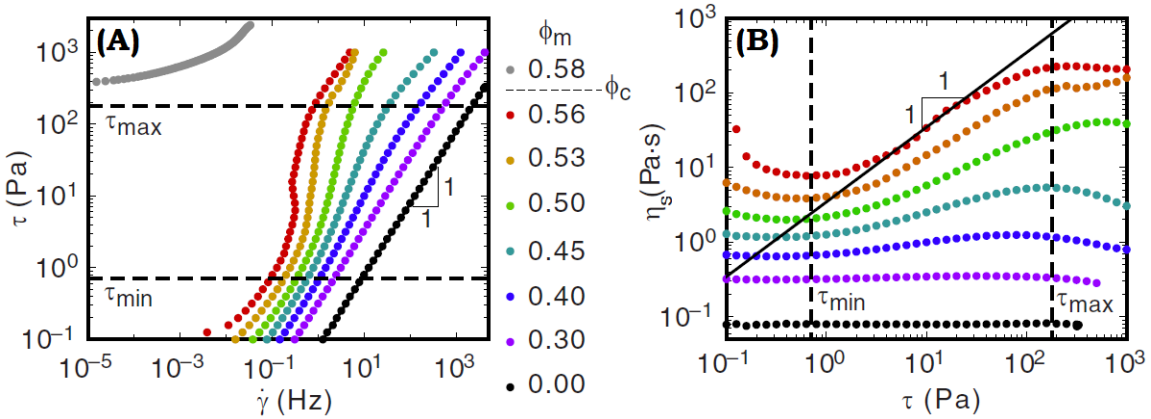

Figure 1.9: Evolution from continuous to discontinuous shear-thickening with packing fraction in a cornstarch-85%m glycerol-15%m water representative suspension. **(A)** *Shear rate $\dot{\gamma}$ versus shear stress τ in which shear-thickening regions are the ones with a slope larger than unity.* **(B)** *Shear stress τ versus viscosity η_s where a slope of one shows a discontinuous jump in η_s. Adapted from* Brown and Jaeger [19]. *Copyright 2014 Reports on Progress in Physics.*

granular shear flows becomes frustrated by the boundary conditions which confine the suspension causing the shear to generate normal stresses at the boundaries. As a result, a restoring force is generated by the confinement and transmitted through frictional grain contact networks to produce shear stresses proportional to normal stresses and enable the discontinuous shear-thickening regime [22] [19]. With this explanation, the background into shear-thickening under steady-state conditions is concluded and we shift towards the dynamic phenomena of shear-thickening which are the most relevant for this work.

1.4 Dynamic phenomena of shear-thickening

Most research work related to the dynamic phenomena observed in shear-thickening suspensions can be split into two categories: one which deals with the stable protrusions and holes generated in vibrated layers (previously shown in figure 1.2) and another which exploits the impact resistance and dynamic solid-like behaviour of suspensions [19]. The main focus of this thesis will be on the latter.

A quick estimation of how much stress a cornstarch-water suspension has to withstand when an adult of, say, 80 kg weight and 10×20 cm^2 surface contact area runs across it without sinking (as shown previously in figure 1.1), results in approximately 40 kPa. However, the predicted upper stress limit during DST at steady-state conditions by Brown and Jaeger is an order of magnitude lower, and the lubrication forces predicted by the hydroclustering mechanism do not come close [22]. In an experiment in which a metal rod hits the surface of a cornstarch-water suspension, Waitukaitis and Jaeger show the need for revisiting of the impact resistance dominated by shear-thickening. They

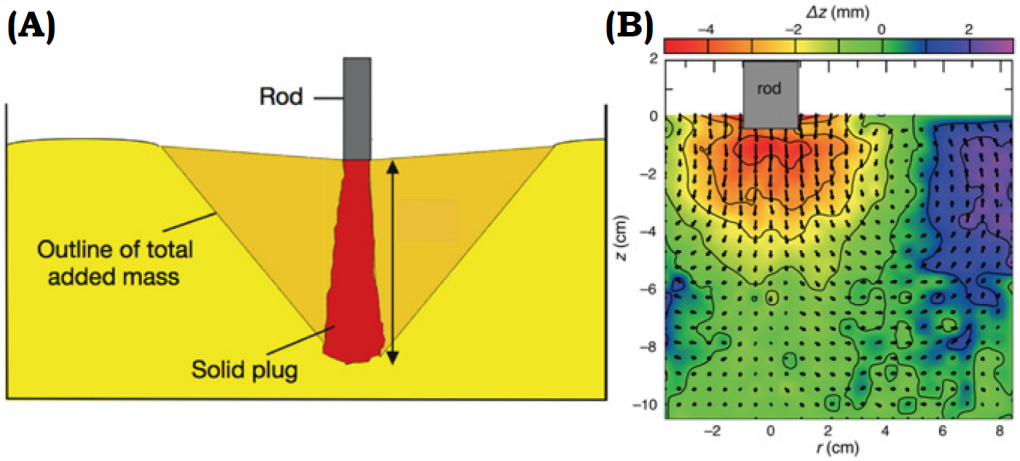

Figure 1.10: **(A)** *Impact-activated solidification front where the red colour depicts the solidified region and the surrounding orange represents the shape of the effective added mass.* **(B)** *Cross-section of the displacement field Δz obtained from x-ray images of tracers inside the suspension, taken 60 ms after impact. Adapted from* Waitukaitis and Jaeger [9]. *Copyright 2012 Nature.*

find that these high stresses originate from an impact-generated solidification front, or a solid plug as illustrated in figure 1.10, that transforms an initially compressible matrix of particles into a rapidly growing jammed region and ultimately leads to an extraordinary amount of momentum absorption [9]. Some of their most important conclusions are that the solidification process requires a finite amount of time to propagate through the suspension, and once it reaches the bottom boundary, forces propagate with no detectable delay through a now jammed solid-like region which bears stress and stores energy back towards the impactor. Transient as it is, the impact-activated solid has been found to exhibit a yield stress and elastic properties just before 'melting', in contrast to shear-thickened states that occur before yielding. Waitukaitis and Jaeger provided direct evidence that the large normal stress transmission between the moving object and the boundary is a result not of the presence of the boundary, but instead of the momentum transferred while the quickly growing jammed solid is pushed through the surrounding suspension by the impacting object [9].

Four years later, Peters *et al.* attempted to summarize the transition between shear-thickening to shear-jamming from an experiment that systematically explores both the steady-state and transient regimes of concentrated suspensions with the same experimental setup (rotating inner cylinder in a Couette-geometry). They suggest that the following mechanism takes place: at low shear stress the particles are not in contact with each other and lubrication forces prompt Newtonian behaviour. Beyond a critical stress, frictional forces generate a fabric of force chains, resulting in DST in which lubrication plays a negligible role (as suggested before in section 1.3) [23]. Instead of a fully-jammed state, they describe this as a fragile state that intermittently flows and gets stuck, but interestingly enough, the critical stress required for frictional contacts is believed to be independent

of packing fraction because it solely relies on the microscopic breakdown of lubrication [18]. With stress elevation, the force network becomes denser until a fully shear-jammed (SJ) state is reached. The role of packing fraction (also shown in figure 1.11) only comes into place to set the threshold for the critical shear stress leading to this SJ state, and to determine the transition to the isotropically fully-jammed state (J) [23].

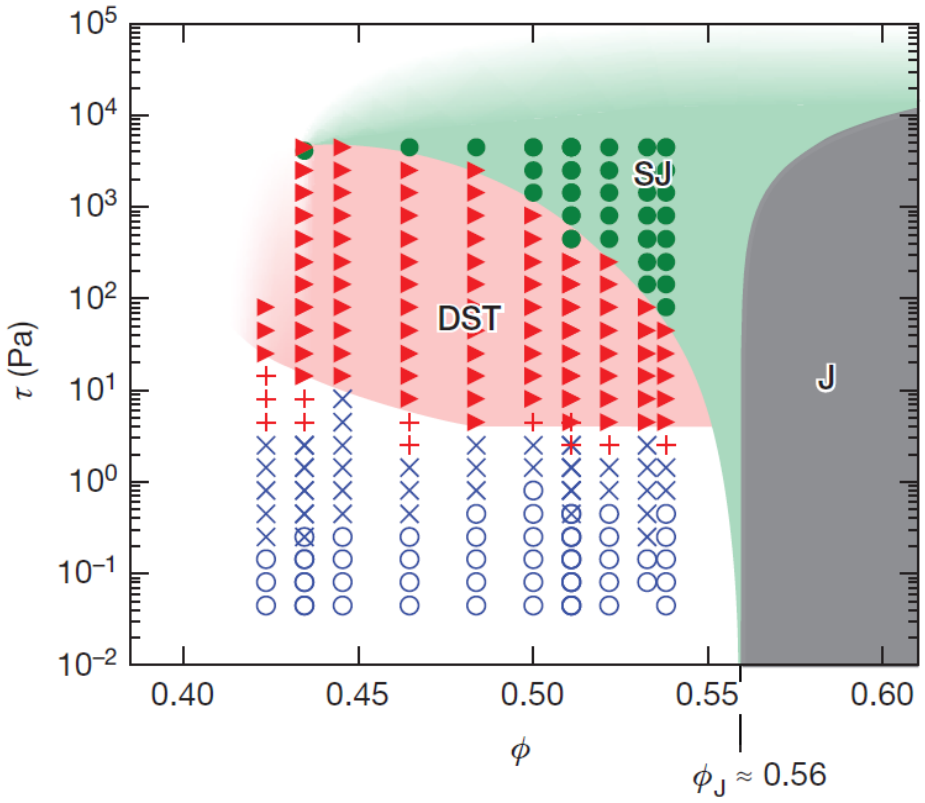

Figure 1.11: State diagram presenting the different suspension regimes: shear-thinning (blue circles), Newtonian (blue crosses), continuous shear-thickening (red crosses), discontinuous shear-thickening (red triangles), and shear-jammed (green dots). The shaded areas correspond to the original shear jamming state diagram, with isotropic jammed (J) and anisotropic shear-jammed (SJ) regimes presented in section 1.1. The regime of shear-thinning or Newtonian behaviour at stresses below the onset of DST corresponds to conditions in which stresses are too small to allow frictional particle–particle contacts. The regime of fragile states is identified with the DST regime. Adapted from Peters *et al.* [23]. *Copyright 2016 Nature.*

The experiment most closely related to this thesis is the work performed by von Kann *et al.*, in which they showed non-monotonic settling of objects in shear-thickening suspensions [2] [24]. Their experimental setup is disclosed in figure 1.12 which also illustrates the peculiar behaviour of the trajectory and sinking velocity of the settling objects. It can be seen that, in contrast to what occurs in Newtonian fluids, the intruder does not reach a terminal velocity to monotonically stop at the bottom, but instead oscillations around a terminal velocity dominate within the bulk and then the object goes through a series of stop-and-go cycles near the bottom of the container. Just

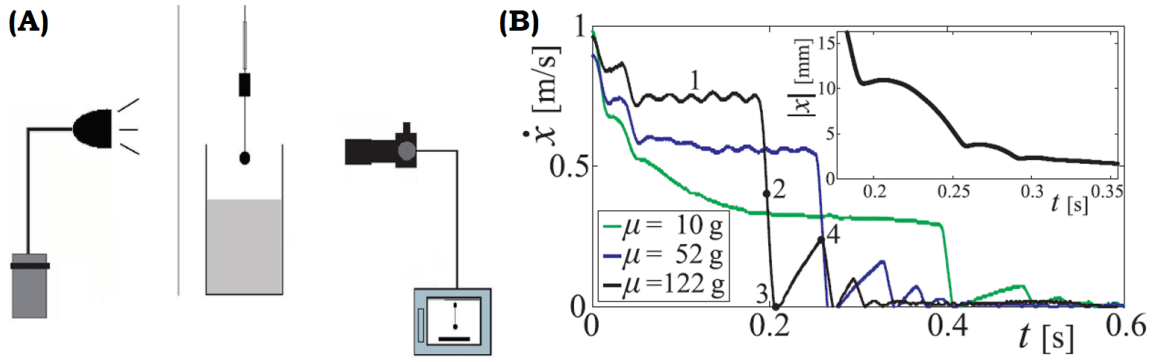

Figure 1.12: **(A)** *Schematic overview of the setup. A light source illuminates a diffusing plate on the left-hand side. A container filled with cornstarch suspension is placed in between the imaging device and the diffusing plate. A wire with a built-in marker which goes through an opening that restricts horizontal motion is attached onto the intruding ball. A high-speed camera is imaging the marker at 5000 frames per second.* **(B)** *A plot of time t [s] versus sinking velocity $\dot{x}(t)$ [m/s] of the settling sphere for three different buoyancy-corrected masses. The inset shows the trajectory of the sinking sphere during the stop-and-go cycles region. Adapted from* von Kann *et al.* [24]. *Copyright 2011 Physical Review E.*

before the stop-and-go cycles, the object reaches a certain velocity around the terminal, following an abrupt stop or just an immense slow-down. Then the object accelerates gradually to another maximum velocity before it comes to another abrupt stop a little closer to the container base. They observed that velocity re-acceleration peaks decrease in succession as the intruder progresses down through the medium in a cyclic manner. Finally, only after this process has been repeated about 6-7 times, the intruder reaches a complete full-stop at the bottom of the container. They found that these effects are not observed in a wide range of other concentrated suspensions which may be due to the particular shape and size distribution of the particles within (see figure 1.13) [24]. Furthermore, by varying the packing fraction they discovered that the effects disappear below $\phi \approx 0.38$ which lead them to a conclusion that contact forces are a necessary mechanism for the observed phenomena [24].

They captured the basic phenomenology in the bulk with a hysteretic phenomenological drag model which fails to link between the model parameters and the physical properties of the system. To summarize their model, first we show the second-order differential equation which governs objects settling in a fluid, where μ is the buoyancy-corrected mass combining the object mass m and the added mass $m_{\text{added}} = 0.5\rho_{\text{S}}V_{\text{sphere}}$ (see equation 1.4) [2].

$$m\ddot{x} = \mu g + D\left(x, \dot{x}, t\right) \tag{1.4}$$

The following equation is an assumption that the drag force scales with the drag coefficient multiplied by the sinking velocity, where the former is only a function of this same velocity and is divided into

two variants: B_1 for the falling and B_2 for the rising of turnover velocities u_1 and u_2 of the system, respectively [2].

$$D(\dot{x}) = -B(\dot{x})\dot{x} \tag{1.5}$$

The hysteretic model in its complete version is shown in the following set of equation 1.6, upon substitution of the latter into the first described differential equation and linearization [2].

$$B(\dot{x}) = \begin{cases} B_1, & \text{when } \dot{x} \text{ falls below } u_2, \\ B_2, & \text{when } \dot{x} \text{ rises above } u_2. \end{cases} \tag{1.6}$$

$$\dot{x} = \dot{x}_i + (u_i - \dot{x}_i)\exp\left[-\frac{\mu B_i}{m}(t - t_0)\right]$$

$$B_1 = \left(\frac{-u_2 + u_1}{\Delta t_1}\frac{m}{\mu} + g\right)\frac{1}{u_1}$$

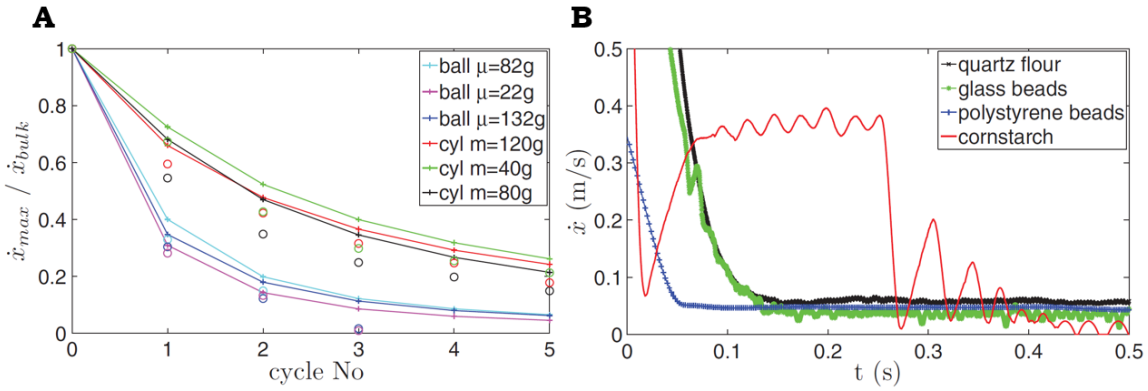

Figure 1.13: **(A)** *The maximum velocities reached during the stop-go cycles. Circles represent the experiment findings, while the lines correspond to the model results.* **(B)** *Velocity evolving with time of a steel sphere of diameter 1.6 cm in four suspensions of quartz flower, polysterene beads, glass beads, and cornstarch. Adapted from* von Kann *et al.* [2]. *Copyright 2013 Physical Review E.*

Finally, von Kann *et al.* developed a jamming model to capture the second peculiar phenomenon in relation with settling of objects in such suspensions - the stop-and-go cycles near the bottom of the container. To obtain this model, they modified equations 1.4 and 1.5 to the following system:

$$\begin{cases} m\ddot{x} = \mu g + D & \text{when } \phi < \phi_{\text{cr}} \\ \dot{x} = 0 & \text{when } \phi \geq \phi_{\text{cr}} \\ D = -B\dot{x} \end{cases} \tag{1.7}$$

They argued that the cornstarch layer below the intruder jams through pure compression, and thus included a term for the rate of change in packing fraction $\dot{\phi}$ that scales with the compression rate $-\dot{x}/x$ of the bottom layer and a term that decreases ϕ through a relaxation process towards its equilibrium value ϕ_{eq} (the packing fraction of quiescent cornstarch suspension), and multiplying both terms with proportionality constants c and k, respectively, as read by equation 1.8:

$$\dot{\phi} = -c\frac{\dot{x}}{x} - k\left(\phi - \phi_{\text{eq}}\right) \tag{1.8}$$

As demonstrated by their results in figure 1.13, the proposed jamming model was finally able to obtain the maximum velocities reached during stop-and-go cycles of the experiments with spherical and cylindrical intruders relatively well [2].

1.5 Probing granular systems with MRI

The opaque nature of granular systems has been a difficult challenge for experimental researchers for a long time. The main challenges have been to probe the granular dynamics in the interior of the 3D system and get adequate temporally-resolved images. Recently, clinical-science-developed techniques like x-ray Computed Tomography (x-ray CT) [25], Positron Emission Tomography (PET) [26], high-speed ultrasound [27], and Magnetic Resonance Imaging (MRI) [28] have been extended in their use to image the inside of 3D granular systems. However, x-ray CT and PET lack the possibility to track particle motion [29], while the high-speed ultrasound technique suffers from coarse spatial resolution and poor signal when air bubbles are present (air reflects echos) [27]. MRI, despite its low spatio-temporal resolution, has remained promising for development and research in granular matter [29].

Magnetic resonance imaging is essentially an application of Nuclear Magnetic Resonance (NMR) that was developed more than four decades ago and already has achieved an astonishing success in medical applications and research, marking 6 Nobel prize winners in its development [30] and a current industry market worth more than €4 billion and projected to grow by a total of exceeding 30% in the next 4 years [31]. To briefly explain the basic physics of MRI operation, we must first consider the fact that subatomic particles have the quantum mechanical property of spin, and certain nuclei, such as ^{1}H (having 1 proton), have non-zero spin and therefore possess a magnetic moment. Other nuclei with both even proton numbers and neutron numbers (like ^{12}C or ^{4}He) have zero spin and are consequently nuclear-magnetic-resonance-'invisible' [32]. The break-through that rendered MRI possible happened when atomic nuclei with non-zero spin were found to be able to absorb and

emit radio frequency (RF) energy when placed in a magnetic field. This was achieved by Rabi *et al.* [33] for which he received a Nobel prize in 1944. So essentially, e.g. the most frequently used hydrogen ^{1}H nucleus is used to generate a detectable RF signal which can be picked up by closely located antennas after pulses of radio waves have excited the nuclear spin energy transition, and magnetic field gradients have localized the signal in space. Then pulse sequences come into use to generate different contrasts between the relevant imaged objects based on the relaxation properties of the hydrogen atoms therein [30].

In medical applications MRI has performed exceptionally well in providing images of high spatial and low temporal resolution (on the order of minutes), but this low temporal resolution did not hinder it to become an indispensable diagnostic tool to routinely provide detailed non-intrusive information about our anatomy, physiology and pathology. MRI scan acceleration techniques have allowed to measure human physiology dynamics, such as blood flow and brain activation (fMRI) at temporal resolutions which are more than sufficient for the application at hand [34]. Granular dynamics, however, may require time scales which are orders of magnitude smaller, typically down to even milliseconds [35] [27]. But those are not all the challenges that granular dynamics researchers face when choosing to operate MRI scanners. They essentially are high-tech systems which consist of superconducting magnets, powerful gradient systems, RF and signal processing chains which require experts with extensive knowledge in system set-up, pulse sequences, hardware development, and more. These are all the more reasons why the immense product, maintenance, running and operating cost sometimes become an ultimate barrier for researchers. For instance, the superconducting magnets require continuous supply of helium which is not only expensive but also finite and scarce on the planet. Another challenge with MRI is the available space for imaging, which restricts granular system sizes. And last but not least, because of the strong magnetic fields, all samples, attached parts and devices used during experiments must be free from ferromagnetic elements and even non-magnetic metal parts which may disturb the imaging process with eddy-currents. This is an especial problem if systems are in the need to be locally agitated by a mechanical device, for example. In such cases researchers use motors or shakers which are driven by air pressure or placed adequately far away from the scanner [32].

The work in this thesis claims to have overcome all challenges accompanying the usage of MRI for granular systems applications and the main reason for this progress is the development of the MRI scan methodology that enables both spatially- and temporally-resolved measurements of intensity and velocity fields from the interior of the granular systems by Penn *et al.* of the Laboratory of

Energy Science and Engineering in ETH Zürich, and also the same laboratory from which this thesis research originates [29].

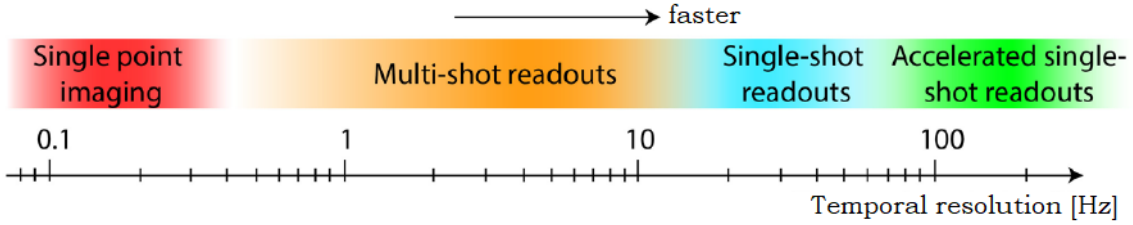

Figure 1.14: Temporal resolution of different MRI data acquisition schemes. Adapted from Penn [34]. *Copyright 2018 ETH Zürich.*

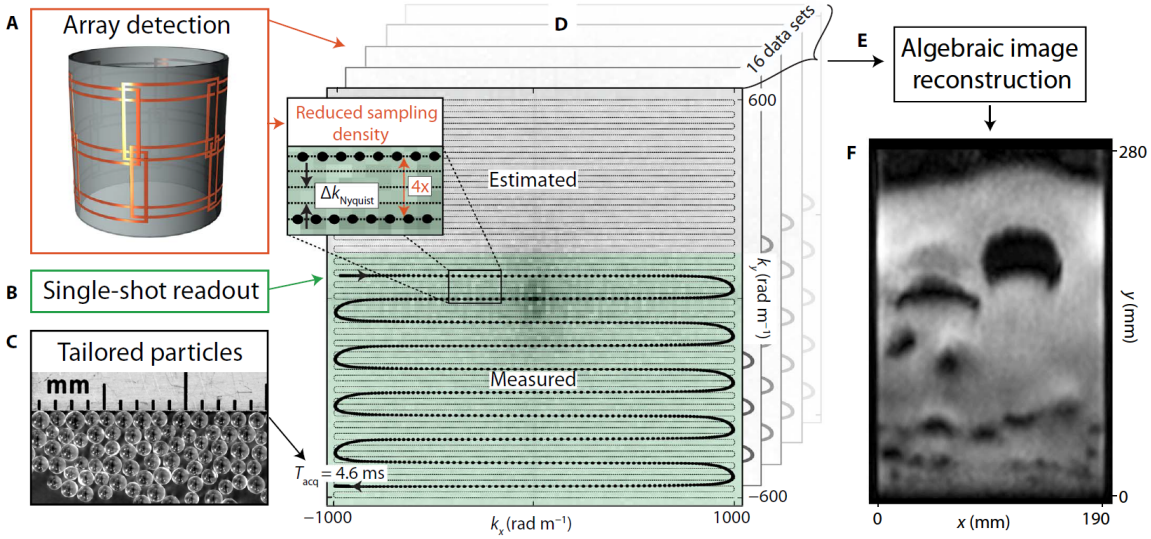

Figure 1.15: Enabling single-shot MRI of granular dynamics. **(A)** *Parallel MR detection using an array of* 16 *RF coils located closely around the region of interest* **(B)** *Single-shot echo-planar imaging (EPI) readouts applied for time-efficient k-space sampling within one spin coherence. The readout duration is further decreased by employing asymmetric partial Fourier sampling. The part acquired in k-space is illustrated in green, while the part that is estimated in the algebraic image reconstruction step is shown in gray.* **(C)** *Tailored oil-filled agar particles with enhanced MR signal intensity.* **(D)** *k-space representation of the single-shot EPI readout trajectory shown with bold black dots and arrows. The light dashed line shows the conventional EPI sequence sampled to the Nyquist limit.* **(E)** *Algebraic image reconstruction correcting for the undersampled, asymmetric k-space information via an exploitation of the varying spatial sensitivities of the 16 received channels used.* **(F)** *Reconstructed image with a temporal and spatial resolution of* 7 *ms and* 3 mm × 5 mm × 10 mm, *respectively, and an FOV of* 200 mm × 300 mm. *Adapted from* Penn *et al.* [29]. *Copyright 2017 Science Advances.*

Prior to the work of Penn *et al.*, MRI has been used in granular dynamics under the limit of time-averaged ($>10^2$ s) 2D images of particle velocity [28] [36] or rapid 1D measurements [29] [37]. These limitations in resolution were mainly due to the fact that to obtain images with sufficient signal-to-noise ratio (SNR), several excitations of nuclei per image were required. Such multi-shot readouts are time-expensive because a significant delay occurs in between excitations. Penn *et al.* instead presented a methodology to advance from multi-shot MR sequences to time-efficient single-

shot readouts that allow for repetitive intensity image production in systems large enough to allow for disordered complex flow every 7 ms, and also took this methodology one step further to allow for particle velocity imaging with a temporal resolution of 22.5 ms (see figure 1.14). This groundbreaking work effectively advanced MRI velocimetry of granular dynamics from temporally-averaged images that are four orders of magnitude larger in resolution to instantaneous snapshots [29]. This was achieved by placing 16 radio frequency (RF) receiver coils around the region of interest to perform the array detection of the MR. The spatially varying sensitivities of the receiver coils allow for a decrease in the sampling density of k-space (the Fourier transformed space that contains the raw MR image information prior to reconstruction) below the Nyquist limit [38], and thus effectively decreasing the acquisition time T_{acq} when compared to single-channel acquisition [29]. Figure 1.15 shows the methodology that Penn *et al.* undertook to perform real-time ultra-fast MRI of bubble dynamics inside a cylindrical 3D gas-solid fluidized bed.

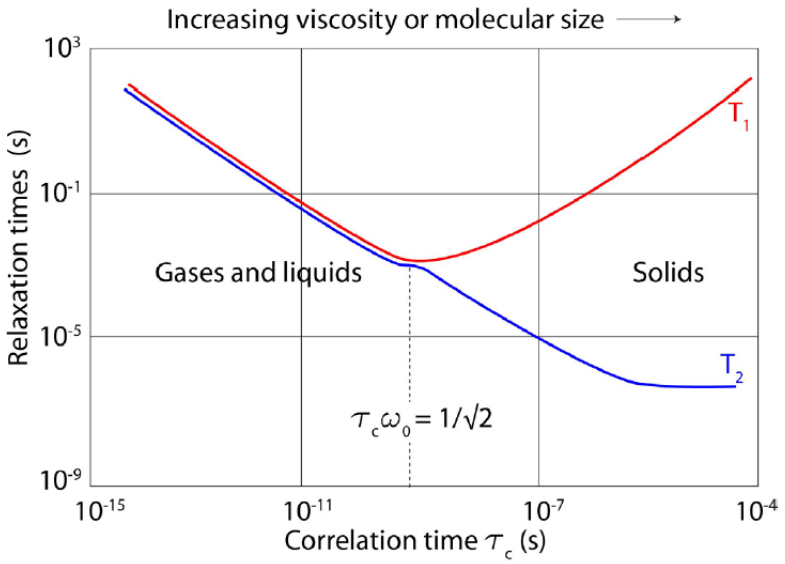

Figure 1.16: Dependence of nuclear magnetic resonance relaxation times T_1 and T_2 on the correlation time τ_c, where τ_c is the characteristic time needed for a molecule to rotate by one radian. Adapted from Bloembergen *et al.* [39] *and* Penn [34]. *Copyright 1948 Physical Review.*

The application of this methodology is not strictly restrictive to bubble dynamics and the tracking of granular particles which are doped for higher signal acquisition, but rather, can be utilized in many different ways, just so long that the transverse relaxation time T_2 of the imaged objects is sufficiently high. This is because the T_2 relaxation time, or the time constant in the quasi-exponential decay of the transverse components of magnetization $\mathbf{M_{xy}}$ (see equation 1.9b), sets the upper limit for the duration of a MRI signal acquisition readout after the spin excitation during echo-planar imaging (EPI). Figure 1.16 presents the behaviour of the longitudinal T_1 and transverse

T_2 relaxation times with the increase of viscosity, where T_1 is the time constant in the process by which the net magnetization $\mathbf{M}$ grows or returns to its initial maximum value ($\mathbf{M_0}$) parallel to the magnetic field $\mathbf{B_0}$ (see equation 1.9a).

$$\mathbf{M_z} = \mathbf{M_0}\left(1 - \mathrm{e}^{-\frac{t}{T_1}}\right) \tag{1.9a}$$

$$\mathbf{M_{xy}} = \mathbf{M_0} \cdot \mathrm{e}^{-\frac{t}{T_2}} \tag{1.9b}$$

A quick trace into the graphs in figure 1.16 shows that water, being a liquid, possesses relaxation times that are sufficiently long enough for accelerated parallel MRI scans, and therefore the proposed methodology by Penn *et al.* is deemed applicable for the research work of this thesis.

1.6 Overview of the thesis and objectives

If one conclusion can be made from the background overview presented, it is that there are still many uncertainties for the link between shear-thickening, dynamic shear-jamming and isotropic jamming. Particularly, the physical mechanism of bulk velocity oscillations and stop-and-go cycles occurring when an intruder sinks in a container filled with cornstarch suspension is still not understood. Simply, more data is required for the behaviour of the suspension itself during these phenomena. The work in this thesis takes the experimental observations found by von Kann *et al.* [2] [24] one step further by employing the MRI methodology developed by Penn *et al.* [29] to image non-intrusively the cornstarch-water suspension's interior during the impact and settling of a spherical intruder. First of all, the wire experiment suggested by von Kann *et al.* will be performed and used as a reference. Secondly, rapid 1D MRI measurements will be obtained to track the vertical motion of the undisturbed intruder. Lastly, 2D velocity-encoded MRI (EPI) scans will be executed to obtain the velocity field of the macroscopic fluid motion surrounding the intruder and its two-dimensional trajectory. With these experiments, a set of objectives are set for this work. They are listed as bullet points below.

- The wire experiment by von Kann *et al.* restricts horizontal motion and rotation of the settling object. This work will test whether the presence of these acts cause an effect on the trajectory and physics of the settling object during the bulk oscillations and stop-and-go cycles. It is hypothesized that the motion of the intruder will vary significantly because the intruder will try to find the 'easiest' path during settling.
- The behavioural regime of the suspension will be determined during the velocity oscillations occurring in the bulk of the suspension after examining the averaged shear rate and shear stress field below the intruder.

- A hypothesis will be tested asking whether the boundaries of the container play a role in the velocity oscillations via propagating waves of granular material sideways.
- The behavioural regime of the suspension will be determined during the stop-and-go cycles occurring near the bottom of the container after examining the averaged shear rate and shear stress field below the intruder.
- A direct observation will be performed on the phenomena occurring just after impact.

2 Experimental Setup

This chapter will discuss the experimental setups of the two types of experiments undertaken in this thesis work. Section 2.1 explains the methodology of intruder trajectory imaging with a wire and a high-speed camera. Section 2.2 tackles the setup and methodology of the MRI experiments.

2.1 Wire marker tracking

The experimental set-up for the experiment with the wire uses the same concept as proposed by von Kann *et al.* [2].

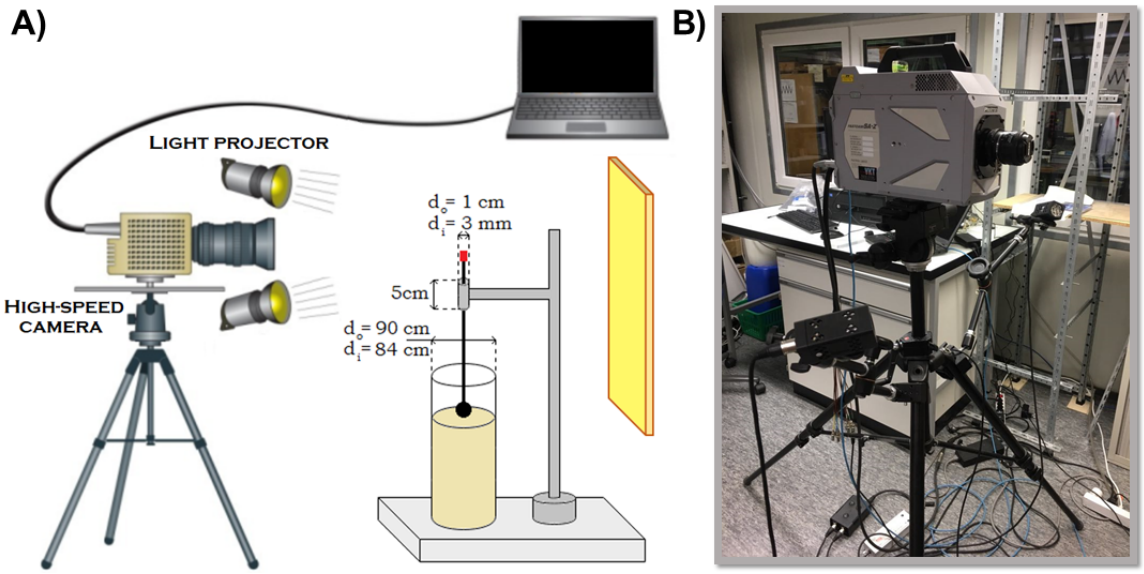

Figure 2.1: **A)** *Schematic of the wire experimental setup. Illustration of the high-speed camera adapted from* Kwon *et al.* [40]. **B)** *Photograph of the Photron FASTCAM SA-Z high-speed camera and light projectors.*

An opening was drilled through three hollow plastic balls of different sizes, through which they were filled with dry solid ZrO_2 (Zirconia) spherical granules of density $\rho_{ZrO_2} = 6000$ kg/m^3 and random close packing volume of approximately 64%, yielding a total intruder density of $\rho_{\text{filled, intr}} \approx 3200$ kg/m^3. Through the same opening, a stiff steel wire ($\rho_{\text{steel}} \approx 8000$ kg/m^3) with a radius of $R_w = 0.5$ mm and length of $L_w = 20$ cm was glued with a silicon-based adhesive in order to get fix-constrained to the intruder. A quick estimation for the wire weight gives $M_w = \left(\pi R_w^2 L_w\right) \rho_{\text{steel}} = 1.2$ g which is less than 10% the weight of the smallest used ball (11.7 g) and is therefore deemed negligible [2]. Once the wire has been extended through the opening of the ball, a 2-cm black tape was attached on top of it to serve as the marker which is to be imaged by the high-speed camera. A cylinder container of inner and outer diameters 8.4 cm and 9 cm, respectively, was filled with suspension of bed fill height $H_{\text{fill}} = 16.5$ cm and was placed in front of a 1-mm-thick beige sheet which was illuminated by 2 light projectors from both sides of the high-speed camera. A fixed clamp

support held a PVC rod of 1 cm outer diameter, 3 mm inner diameter and length of 5 cm vertically. The wire was placed through the rod and adjusted such that the ball reaches the bottom and the marker on top of the wire does not extend to more than the Field of View (FoV) of the camera, as illustrated by figure 2.1.

The high-speed camera model used was a Photron FASTCAM SA-Z, capable of providing images of 1024×1024 pixel resolution at up to 21000 frames per second (fps), and lower spatial resolution images at up to $2 \cdot 10^6$ fps. Naturally, before starting the experiment and turning off all external light, the camera is levelled in all directions, it is adjusted such that its focus is set on the marker placed in front of the illuminated sheet and it is connected to a computer which operates the TeamViewer™software. Using the software, the camera is set to image continuously at 3000 fps with an end-time trigger mode, meaning that when the experiment is finished, a remote controller is clicked and the last 52264 frames are saved. To perform the experiment, the operator lifts up the wire until the intruder reaches the desired drop height (17.5 cm for all intruder sizes), applies lubricant oil between the rod and the wire to reduce frictional effects and lets go of it in a single quick motion. When the bottom of the marker reaches the top of the PVC rod (meaning that the intruder is on the bottom of the container), the remote controller is clicked and the experiment data is saved. The data is then cropped, if necessary, and exported to an external hard drive. In total, the wire experiments were performed for two non-density-matched cornstarch-water suspensions of packing fractions $\phi_s = 0.41$ and $\phi_s = 0.44$, two density-matched cornstarch-aqueous solution suspensions (the aqueous solution was a mixture of water and CsCl that matches the density of cornstarch particles provided in the literature, specifically $\rho_{cs} \approx 1590$ kg/m^3 in order to level the densities and avoid sedimentation) of packing fractions $\phi_s = 0.41$ and $\phi_s = 0.44$, $100v\%$ water, $50v\% - 50v\%$ water-glycerol solution and $100v\%$ glycerol, all repeated twice at the same bed fill height and drop height.

2.2 Magnetic Resonance Imaging

All scans were performed on a 3 Tesla whole-body human MRI system (Achieva 3T, Philips Healthcare, Best, The Netherlands) with a bore diameter of 600 mm.

Detection of radio frequency signals in magnetic resonance imaging is achieved through Faraday induction in RF receiver coils which are tuned to the Larmor frequency ω_L of the probe nuclei in the particular static magnetic field B_0. In this work the probe nuclei are exclusively ^{1}H protons with a gyromagnetic ratio $\gamma = 2.675 \cdot 10^8$ rad T^{-1} s^{-1} and therefore provide a Larmor frequency at the 3 T static magnetic field of

$$\omega_{\mathrm{L}} = \gamma B_0 = 2\pi \cdot 127.8 \text{ MHz}. \tag{2.1}$$

The chain of events to obtain an MRI experiment image therefore happens as follows (see figure 2.2). First, an RF excitation pulse at the Larmor frequency ω_{L} is generated by an RF signal generator, amplified and sent to a large RF volumetric transmitter coil, which is integrated into the bore shell of the MRI system. The alternating current in this transmitter coil creates an electromagnetic field, which excites the spins of the probe nuclei homogeneously throughout the sample volume. Directly after their excitation, the spins relax into the initial spin configuration while sending out an electromagnetic field and thus inducing an electromotive force (emf or voltage) in the receiver surface coils which are located closely around the sample.

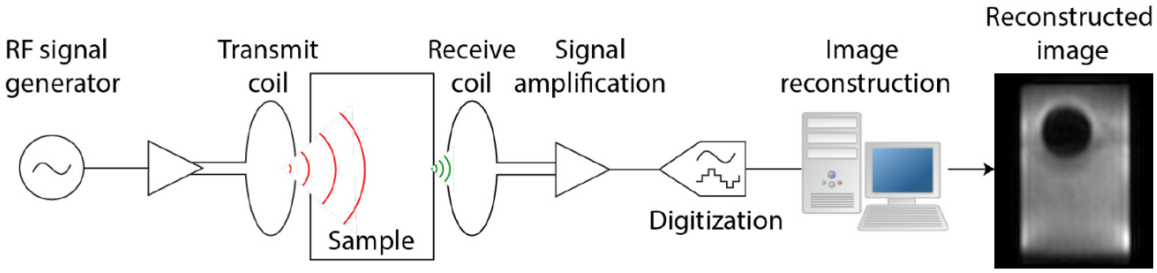

Figure 2.2: Schematic of the RF signal chain of an MRI experiment. An RF excitation pulse at the Larmor frequency ω_L is generated, amplified and sent to the RF transmitter coil. The alternating current in the loop coil creates an electromagnetic field, which excites the spins of the probe nuclei within the sample. Directly after their excitation, the spins relax into the initial spin configuration while sending out an electromagnetic field. This field induces a voltage in the receiver coil, which is also tuned to ω_L. Subsequently, the signal is amplified, digitized and sent to a computer, where the data is reconstructed to an MR image. Adapted from Penn [34]. *Copyright 2018 ETH Zürich.*

In this work, two lateral and two circular receiver coils are incorporated into a custom-built 4-channel RF receiver array and glued onto an acrylic tube with outer diameter 110 mm and inner diameter 100 mm using copper adhesive tape (see figure 2.3). Each individual coil is connected to a high-impedance pre-amplifier circuit (Philips 3 T high-impedance coil element boards) which allows tuning of each resonator to the Larmor frequency and matching its impedance to the noise-optimized impedance of the pre-amplifier to maximize power transmission. This is particularly important for MR image quality because the RF receiver electromagnetic field (Rx) is six orders of magnitude lower than the RF transmitter field (Tx), and the low μV amounts of voltage induced at the Rx field are amplified by a very sensitive signal amplifier. Having such sensitive signal amplifier adds to the complexity of the signal acquisition, because any noise introduced at this stage will be picked up, amplified and propagated along the remaining stages of signal acquisition and processing [29]. In particular, after the signal has been amplified, the digitization and the algebraic image

reconstruction stages follow, the latter of which depends on the type of measurement performed (1D EPI or 2D velocity-encoded EPI).

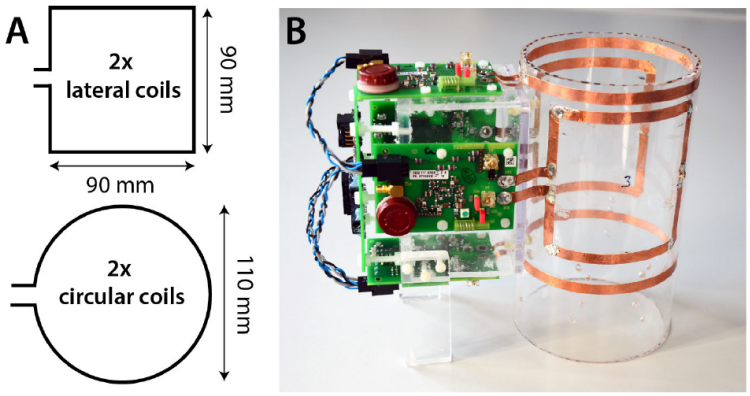

Figure 2.3: ***(A)*** *Schematic of the 4-channel RF receiver array showing 2 lateral coils and 2 circular coils.* ***(B)*** *Photograph of the receiver array. The coils are glued with copper adhesive bands onto an acrylic transparent tube of inner diameter* 100 mm. *The detuning cables of the circuit element boards are knotted to reduce forces induced during RF transmission. Adapted from* Penn [34]. *Copyright 2018 ETH Zürich.*

In order for the entire signal chain to be operational, the container filled with the suspension had to be positioned closely in the interior of the RF receiver coil array. The container was therefore the same one which was used for the wire experiments, specifically a cylinder with 8.4 cm inner diameter, 9 cm outer diameter and a height of 27 cm. The only difference was the method of releasing the intruder, because this had to be done remotely outside of the MRI system room.

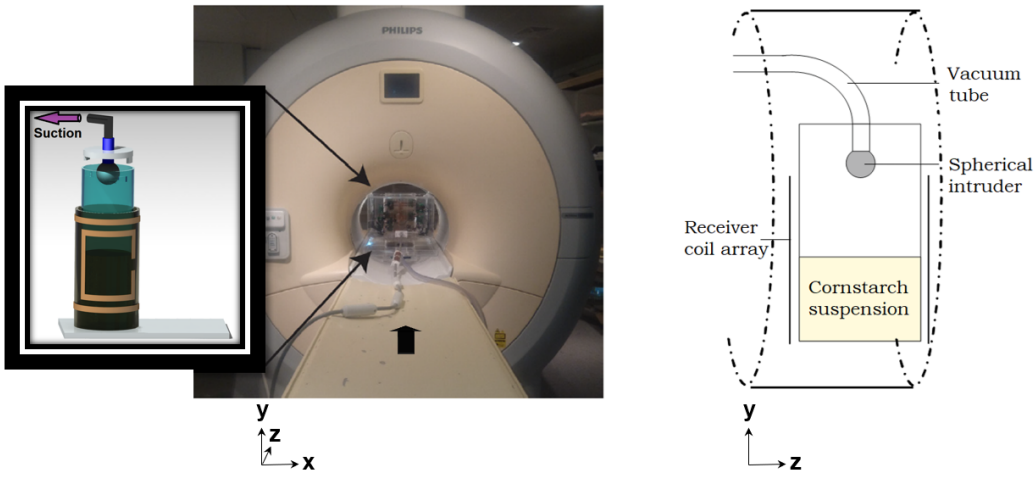

Figure 2.4: MRI experimental setup. From left to right: a CAD model illustrating the principle of positioning of the RF receiver array around the cylinder, a photograph of the setup located at the MRI bore shell, a schematic of the principle of intruder release into the suspension.

Figure 2.4 presents a schematic and a CAD model of the setup and the principle of intruder release. First, a large bottom plate and a container lid were constructed from Poly(methyl methacrylate) (PMMA) using the Epilog 36EXT Laser cutter in ETH Zürich's D-MAVT. Onto this lid, a 40

cm-long straight PVC tube connected to an elbow-type PVC tube were attached through a fixed 4 cm diameter opening in the lid. The elbow tube was turned towards the opening of the MRI bore (the negative $\hat{z}$-direction and attached to a 5-meter-long hose of a vaccuum pump located outside the MRI room.

Before an experiment is performed, continuous mixing takes place to avoid sedimentation in the non-density-matched cornstarch suspension, the ball is positioned on the bottom of the straight PVC tube at the desired drop height, while the 2000 kW vacuum pump is turned on to provide enough suction in order for the intruder to be fixed in place, hanging from the bottom of the straight tube. The lid is closed and bolted with plastic screws and the experimental setup is moved towards the bore of the MRI via a remote controller. All people setting up the experiment leave the MRI room and only then is the imaging initiated. On the mark of the person who is in charge of imaging control and operation, the hose of the vacuum pump is disconnected from the pump in an instant, the suction stops, and the intruder freely falls into the center of the suspension. The imaging stops when the intruder has reached the bottom of the container.

2.2.1 Rapid 1D EPI

Rapid 1D MRI measurements were performed to obtain the vertical trajectory of the undisturbed intruder, i.e. unlike the wire experiment, its motion was not restricted in the radial and tangential directions.

In total, four experiment sessions took place to image intruders of various sizes and masses in both density-matched and non-density-matched cornstarch suspensions of two distinct packing fractions $\phi_s = 0.41$ and $\phi_s = 0.44$. However, the experiment with density-matched suspension of cornstarch and aqueous solution of CsCl and water, which occurred on the 26th of March 2018, yielded an undetectable MRI signal. This phenomenon was later explained by the fact that the ions present in the CsCl salt interfere with the magnetic field and thus make the entire core region of the suspension (except for a small region near the edges of the cylinder) MRI-invisible. The successful measurements were therefore threefold: the Work-In-Progress (WIP) Single-Shot Fast-Field Echo (FFE) sensitivity-encoded (SENSE) 1D EPI which took place on the 22nd of January 2018, the Single-Shot FFE Constant LEvel AppeaRance (CLEAR) 1D EPI which occurred on the 8th of March 2018, and the WIP FFE 1D EPI which was executed on the 18th of May 2018. The need for these various imaging methods was due to the fact that for different suspension packing fractions and intruder masses, different spatial and temporal resolutions are required to capture the length and time scales of the observed phenomena. This is why several MRI imaging parameters (e.g. scan mode, spatial resolution, temporal resolution, flip angle, echo time and repetition time) were

modified during reference scans before performing the experiments with optimal spatio-temporal resolution and highest signal-to-noise (SNR) ratio for the particular conditions.

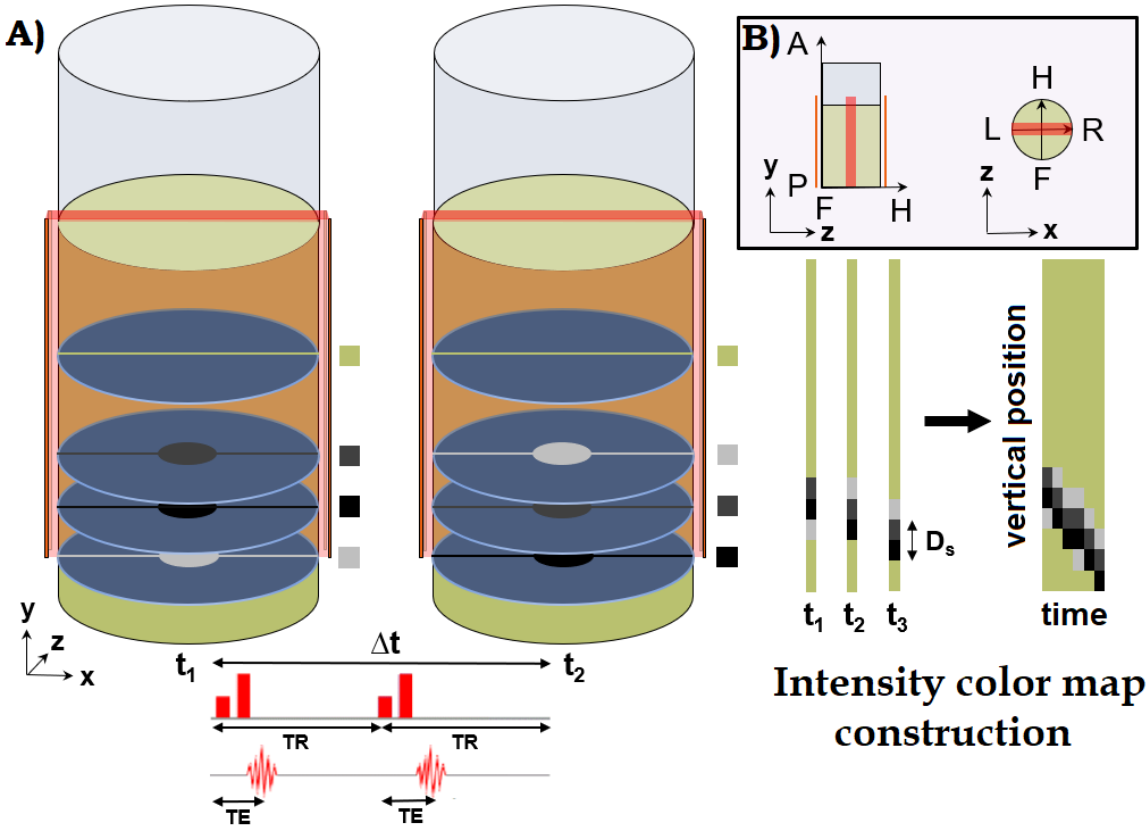

Figure 2.5: Schematic of the 1D MRI setup. **A)** *The principle of 1D image acquisition is illustrated. The red transparent region shows the Field of View of the imaging process. The circles in the vertical slices show the ball location and the horizontal lines show the averaged pixel intensity value, ranging from white (weakest) to black (strongest).* **B)** *The directions in MRI are illustrated for the container: Anterior-to-Posterior, Foot-to-Head and Left-to-Right*

All scans were performed for the region shown in red in figure 2.5: specifically, it is a XY 'plane' of a finite $\hat{z}$-direction size (10 mm), which averages the intensity signal in the positive $\hat{z}$-direction (Foot-to-Head or F-H) and the positive $\hat{x}$-direction (Left-to-Right or L-R), and thus, essentially, obtaining a single intensity value for a pixel of size which corresponds to the vertical spatial resolution and provides information about the vertical motion of the intruder (in the Anterior-to-Posterior, A-P or negative $\hat{y}$-direction). With time, the vertical signal changes as the intruder progresses down the medium, and therefore the image can be reconstructed into a color map consisting of time frame in the horizontal axis and vertical signal intensity, ranging from 0 to 1 in the vertical axis.

Table 2.1 summarizes the relevant chosen parameters and experimental conditions. In total, the intruders were either three different sizes of plastic spheres filled with ZrO_2 particles close to 64% random close packing volume or three different sizes of solid ZrO_2 balls of $\rho_{ZrO_2} = 6000 \text{kg/m}^3$

density. The aqueous solution in the non-density matched cornstarch suspensions comprised of $\phi_{vw} = 3.22\%$ volume fraction of Vasovist® contrast agent in demineralized water used to lower its T_1 longitudinal relaxation time such that its spin can be re-excited quickly. The quantities of water, cornstarch and contrast agent were calculated and weighted prior to the experiment in order to provide the desired packing fraction of cornstarch to aqueous solution and bed fill height in accordance to the following relations of mass, density and volume fraction.

Table 2.1: Rapid 1D EPI experiment setup. In the table, the flip angle parameter stands for the amount of rotation, in degrees, from the y-axis caused by the RF pulse that determines signal intensity, the repetition time is the duration of time between two RF excitation pulses, and the echo time is the duration between the RF excitation pulse and the peak of the measured MR signal.

Parameter	**Value**		
Experiment date	22.01.2018	08.03.2018	18.05.2018
Scan mode	1D Single-Shot EPI	1D Single-Shot EPI	1D Single-Shot EPI
Protocol name	WIP FFE 1D SENSE	FFE 1D CLEAR	WIP FFE 1D
Intruder Type	Filled ZrO_2 sphere	Filled ZrO_2 sphere	Solid ZrO_2 sphere
Intruder Diameter	[20, 30, 40] mm	[20, 30, 40] mm	[20, 30, 42.3] mm
Intruder Mass	[11.7, 44, 120] g	[11.7, 44, 120] g	[15.4, 84.8, 246] g
Packing fraction	0.41	0.44	0.41 & 0.44
Bed fill height	124 mm	165 mm	165 mm
PVC rod base height	255 mm	255 mm	255 mm
Temporal resolution	2.63 ms	3.1 ms	2.49 ms
Spatial resolution [y]	0.460 mm	0.262 mm	0.370 mm
FoV [AP]	140 mm	200 mm	200 mm
Flip angle	20°	20°	15°
Repetition time	2.63 ms	3.10 ms	2.49 ms
Echo time	1.21 ms	1.55 ms	1.14 ms

First off, knowing the desired bed fill height H_{sus} and cylinder radius, the total volume of suspension is first computed via $V_{tot} = \rho_{tot}\pi R_{cyl}^2 H_{sus}$. the densities of aqueous and the total solution are acquired, knowing the desired packing fractions ϕ_{vw} and ϕ_s via equation 2.2, and then allowing for the computation of the total mass of the suspension comprising of aqueous solution and cornstarch.

$$\rho_{aq} = \phi_{vw}\rho_v + (1 - \phi_{vw})\,\rho_w \qquad \rho_{tot} = \phi_s\rho_{cs} + (1 - \phi_s)\,\rho_{aq} \tag{2.2}$$

The individual masses of aqueous solution and cornstarch are then calculated by rewriting the volume fraction relation via

$$M_{aq} = \frac{M_{tot}}{\frac{\rho_{cs}}{\rho_{aq}}\frac{\phi_s}{1-\phi_s} + 1} \qquad M_{cs} = M_{tot} - M_{aq} \tag{2.3}$$

In an analogous fashion, the required amount of water in kg was calculated from the same equation as

$$M_{\mathrm{w}} = \frac{M_{\mathrm{aq}}}{\frac{\rho_{\mathrm{v}}}{\rho_{\mathrm{w}}}\frac{\phi_{\mathrm{vw}}}{1-\phi_{\mathrm{vw}}} + 1} \qquad M_{\mathrm{v}} = M_{\mathrm{aq}} - M_{\mathrm{w}} \tag{2.4}$$

where M_{aq}, M_{cs}, M_{w} and M_{v} are the desired masses of aqueous solution, cornstarch, water and Vasovist®, respectively.

2.2.2 Velocity-encoded 2D EPI

Velocity-encoded 2D echo-planar imaging was also performed for a single XY 'plane' spanning transversely along the height of the suspension. However, in 2D MRI, the signal is only averaged along the 10 mm $\hat{z}$-direction at the center of the suspension, while a 2D image was reconstructed from instantaneous snapshots in the XY plane.

Table 2.2: Velocity-encoded 2D EPI experiment setup

Parameter	**Value**		
Experiment date	08.03.2018	18.05.2018	18.05.2018
Scan mode	2D Single-Shot EPI	2D Two-Shot EPI	2D Two-Shot EPI
Protocol name	WIP EPI VEL SENSE	WIP EPI VEL	WIP EPI VEL
Intruder Type	Filled ZrO_2 sphere	Solid ZrO_2 sphere	Solid ZrO_2 sphere
Intruder Diameter	[20, 30, 40] mm	[20, 30, 42.3] mm	[20, 30, 42.3] mm
Intruder Mass	[11.7, 44, 120] g	[15.4, 84.8, 246] g	[15.4, 84.8, 246] g
Packing fraction	0.44	0.41	0.44
Bed fill height	165 mm	165 mm	165 mm
Drop height	256 mm	256 mm	256 mm
Temporal resolution	65.50 ms	62.00 ms	62.28 ms
Spatial resolution [x,y]	[0.781,0.781] mm	[2.080,2.080] mm	[2.080,2.080] mm
FoV [AP,FH,RL]	[175,10,200] mm	[200,10,125] mm	[200,10,125] mm
Phase enc. velocity [$v_{\mathbf{x}}$,$v_{\mathbf{y}}$]	[12,12] cm/s	[50,50] cm/s	[15,15] cm/s
Flip angle	50°	40°	40°
Repetition time	21.50 ms	10.13 ms	10.34 ms
Echo time	5.684 ms	3.680 ms	4.690 ms

Magnetic resonance phase contrast velocimetry was realized by applying bipolar-motion-encoding gradients prior to the EPI readout. These motion encoding gradients yield a residual phase shift when the imaged fluid (water in the suspension) has a non-zero velocity. The difference in the phase of the measured signal as compared to that from a measurement without flow-encoding gradients is proportional to the displacement of the fluid particles in between flow-encoding gradients. Assuming that the velocity of the particles is approximately uniform across the short interval of time between flow-encoding gradients, the velocity is determined as the displacement divided by the time interval. Finally, this phase-contrast method in combination with conventional echo-planar imaging was used

to generate maps of fluid particle velocity. In the Single-Shot EPI measurements run in this study, three datasets were acquired in order to obtain in-plane velocity components v_{x} and v_{y}: one for each direction of motion and one reference dataset without phase encoding. To obtain each separate dataset the pulse sequence shown in figure A.2 was rerun, and therefore the temporal resolution of image acquisition was roughly three times the repetition time of two subsequent RF pulses, TR. In Two-Shot EPI, each dataset in k-space was filled via two separate spin excitations, and therefore yielding a total of six repetitions of the pulse sequence and two times higher temporal resolution between successive velocity field images. Nevertheless, some experiments with the solid ZrO_2 balls required Multi-Shot EPI due to off-resonances in the static magnetic field B_0 [41]. Table 2.2 presents all relevant settings of the MRI measurements performed with their specific date. In the table, the phase encoding velocity is really the encoded field of flow in $\hat{x}$ and $\hat{y}$ directions.

2.2.3 Algebraic image reconstruction

Figure 2.6 provides a representative schematic of the methodology developed by Penn *et al.* [29] and Pruessmann *et al.* [42] to algebraically reconstruct, accelerate the scan time and acquire the MR images in this work. Essentially, it is a combination between three techniques: Partial Fourier (FP) reconstruction, SENSE reconstruction and reduction of the spatial resolution.

First, Partial Fourier (FP) imaging was performed to reduce MRI scan time by sampling k-space data asymmetrically around the k-space origin. The missing data is estimated by assuming Hermitian symmetry (or conjugate symmetry) of k-space or

$$s(\boldsymbol{k}) = s\left(-\boldsymbol{k}\right)^{*} = \int_{V} \rho(\boldsymbol{r}) \mathrm{e}^{j\boldsymbol{kr}} d\boldsymbol{r} \tag{2.5}$$

where $s(\boldsymbol{k})$ is a k-space data point at position $\boldsymbol{k}$ and the symbol * indicates that its complex conjugate is taken. The main property of a Hermitian function is that its Fourier transform is a real-valued function $\rho(\boldsymbol{r}) \in \mathbb{R}$, and in MRI, spin density distribution of an object can be described by this real-valued function $\rho(\boldsymbol{r})$, whereas the data is acquired in its conjugate space, the k-space. The second technique undertaken was parallel imaging: the multiple RF receiver coils distributed uniformly around the container filled with suspension collect the FP reconstructed k-space data concurrently, and due to their different spatial locations, each coil element possesses different sensitivity to the signal emitted by the aqueous solution in the sample. The data acquired by each channel is weighted according to the channel's spatial sensitivity profile, and then the SENSE reconstruction algorithm [42] is used to exploit the information encoded in the sensitivity of the coils in order to reconstruct unaliased images from sets of data which violate Nyquist's minimum sampling density criterion

[38] [34]. The final scan acceleration technique applied was a reduction in spatial resolution. This was performed for the phase-encoding direction qualitatively by A. Penn, the operator of the MRI scanner during the experiment sessions, by varying the readout duration and choosing a value from which a prolonged time of acquisition no longer improves the apparent spatial resolution of the image [34].

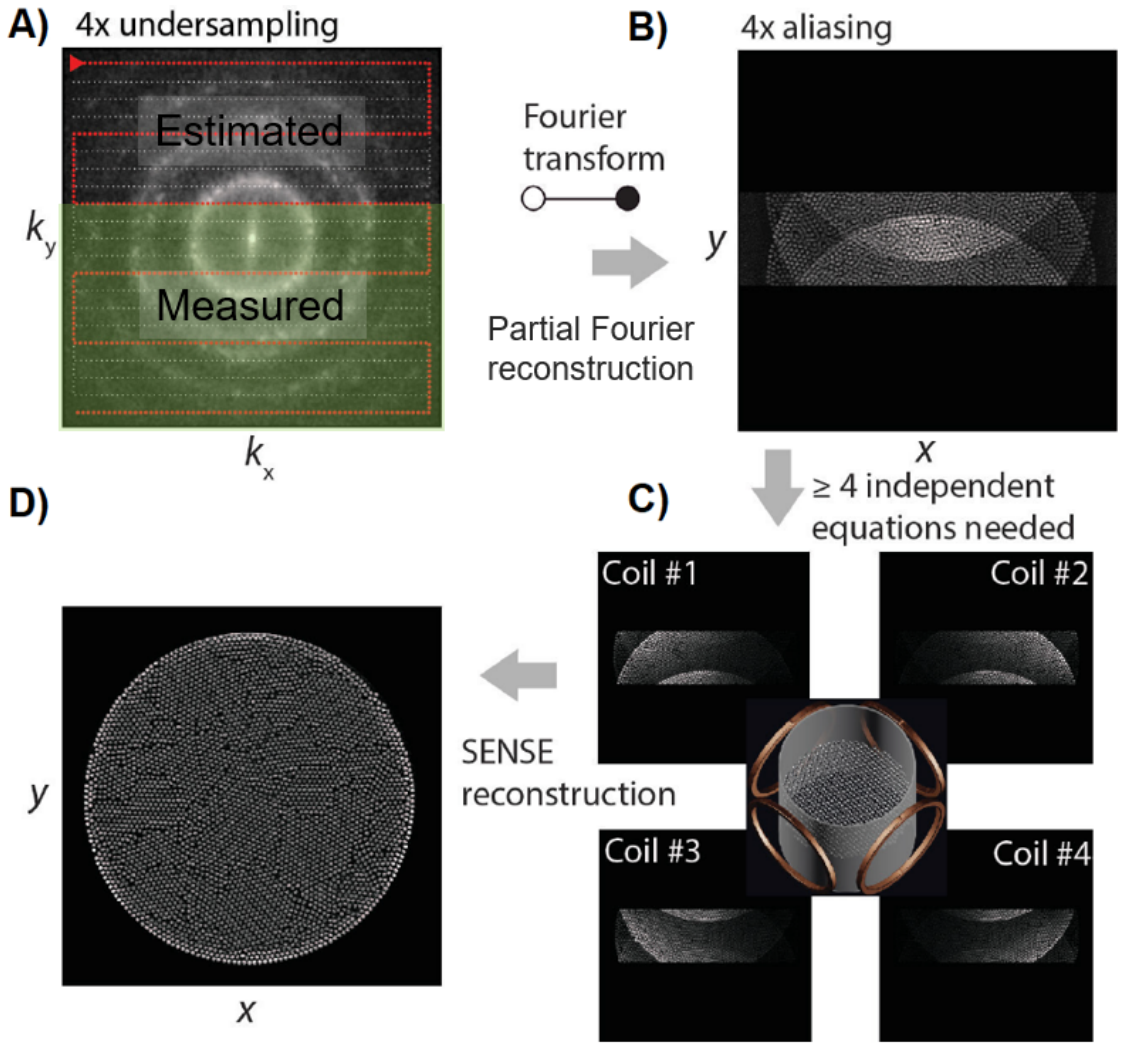

Figure 2.6: Algebraic representative image reconstruction during parallel imaging. **A)** *Sparse sampling of k-space with a density Δk_y, which is four times lower than $k_{Nyquist}$ [38].* **B)** *Strong aliasing artefacts in the MR image constructed by the undersampled k-space data set.* **C)** *The same reduced portion of k-space is acquired by multiple receiver coils which have distinct spatial sensitivities.* **D)** *By exploiting these different sensitivities of the coils, an unaliased image is reconstructed from the data using the SENSE reconstruction algorithm [42]. Adapted from* Penn [34]. *Copyright 2018 ETH Zürich.*

3 Signal Processing

All data acquired from the experiments was raw and needed significant image and signal processing which was carried out in MATLAB. The MRI data was processed using MATLAB in combination with the MRecon interface (ReconFrame 3.0, GyroTools LLC, Zurich, Switzerland). Section 3.1 will describe the steps taken to process the data of the wire experiments, while sections 3.2 and 3.3 will tackle the processing of the 1D and 2D MRI data, respectively.

3.1 Wire experiment processing

This section will deal with the image and signal processing involved in the analysis of the wire experiment. First, subsection 3.1.1 will provide the details of the signal acquisition of the raw images and the processing to obtain the vertical trajectory of the intruder. Then subsection 3.1.2 will focus on the signal processing involved to obtain the sinking velocity of the intruder.

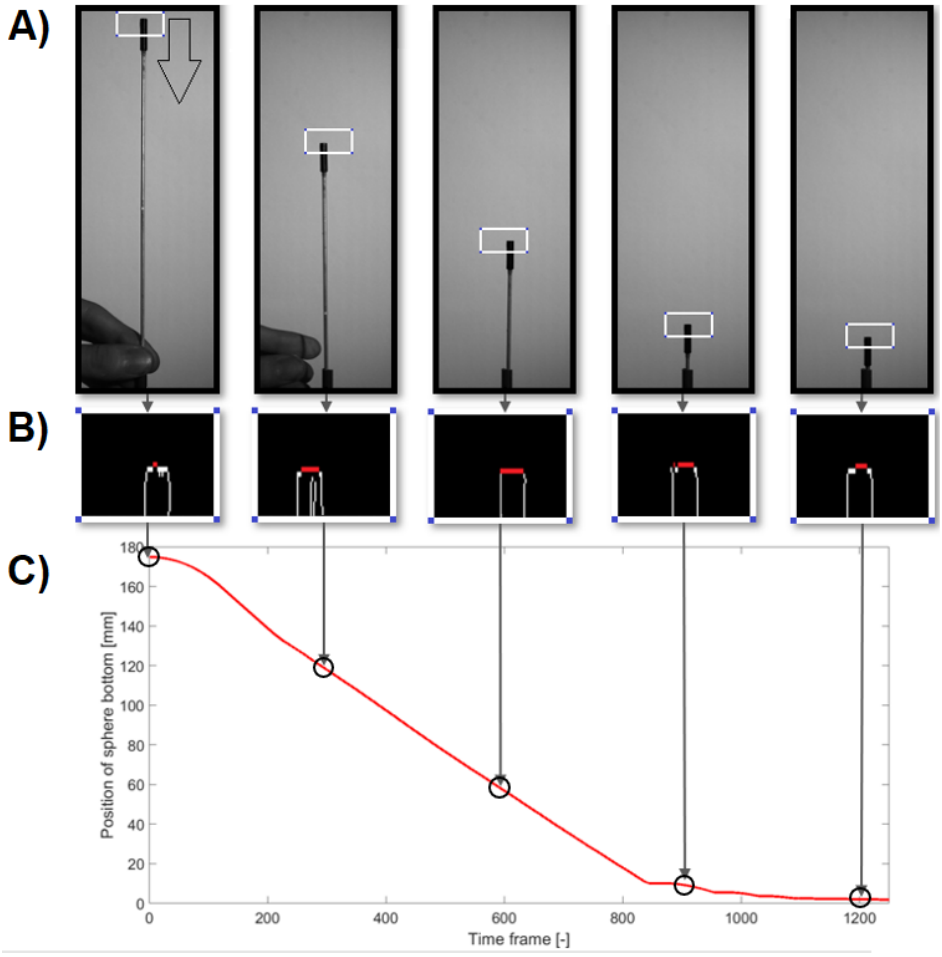

Figure 3.1: Representative wire experiment trajectory signal processing. **A)** *Raw .tif file images of every time frame recorded by the high-speed camera. The white square illustrates the bounding box for which* **B)** *Sobel edge detection algorithm was applied in order to obtain the top-most vertical position of the marker (shown in red).* **C)** *Construction of a plot showing time frame in the horizontal axis and vertical position in the vertical.*

3.1.1 Vertical trajectory

The high-speed camera essentially images a stationary Field of View while the marker on top of the wire sinks through the PVC tube, as shown by the photographs found on the top of figure 3.1. First, the starting and ending frames are defined either by cropping the video during the data export stage from the computer onto the hard drive or in the MATLAB code if more time frames than necessary were saved. Secondly, an initial bounding box is chosen to capture the top marker interface before starting the loop that reads the .tif image files of the individual frames.

The Sobel edge detection algorithm is performed for each frame for the image in the bounding box in order to detect the vertical position of the highest marker edge because of its higher overall accuracy when compared to simple thresholding of the grayscale image. Another reason for choosing the more diverse (independent of image brightness) but also more time-expensive edge detection algorithm is that illumination from the light projectors was not evenly distributed across the field of view, and the marker would reflect more light at certain positions, meaning that the signal intensity read by the camera is altered and a false detected edge may occur unless the threshold is manually changed for different sets of time frames. Instead, Sobel's algorithm is a gradient method which detects edges by looking for the maximum and minimum in the first derivative of the image. It uses two 3×3 kernels, one for changes in the horizontal direction and one for changes in the vertical direction. These kernels are convolved with the original image to calculate the approximations of the derivative as shown in equation 3.1, where $\boldsymbol{G}_{\mathrm{x}}$ and $\boldsymbol{G}_{\mathrm{y}}$ are two images that contain the horizontal and vertical derivative approximations and $\boldsymbol{A}$ is the original source image [43].

$$\boldsymbol{G}_{\mathrm{x}} = \begin{bmatrix} 1 & 0 & -1 \\ 2 & 0 & -2 \\ 1 & 0 & -1 \end{bmatrix} \cdot \boldsymbol{A} \qquad \boldsymbol{G}_{\mathrm{y}} = \begin{bmatrix} -1 & -2 & -1 \\ 0 & 0 & 0 \\ 1 & 2 & 1 \end{bmatrix} \cdot \boldsymbol{A} \tag{3.1}$$

The measure of an edge is therefore computed from the gradient matrices' amplitude and angle [43]:

$$\boldsymbol{G} = \sqrt{\boldsymbol{G}_{\mathrm{x}}^{\boldsymbol{2}} + \boldsymbol{G}_{\mathrm{y}}^{\boldsymbol{2}}} \qquad \theta = \arctan \frac{\boldsymbol{G}_{\mathrm{y}}}{\boldsymbol{G}_{\mathrm{x}}} \tag{3.2}$$

After an edge is detected and converted to binary, the highest vertical index of the edge signal is retrieved as shown by the red-colored region in section **B** of figure 3.1. The position of the bounding box whose horizontal and vertical dimensions are kept constant is then adjusted accordingly for the next iteration. In essence, the bounding box is shifted together with the edge of the marker

with a single time frame delay. After all vertical positions of the marker are acquired, the vertical trajectory of the intruder is constructed as shown by section **C** of figure 3.1.

3.1.2 Vertical velocity and acceleration

Velocity and acceleration are determined by taking the derivative of the trajectory of the intruder at time t using first-order or second-order central difference schemes. The trajectory signal, however, suffered from relatively lower spatial resolution than the temporal resolution at hand, and therefore two methods for dealing with this issue were employed. The first method would simply undersample the signal before taking the time derivative, while the second would apply a smoothing low-pass filter prior to undersampling to artificially create a finer spatial resolution.

Undersampling

The first employed method was undersampling and figure 3.2 shows its performance in velocity estimation for various undersampled time intervals.

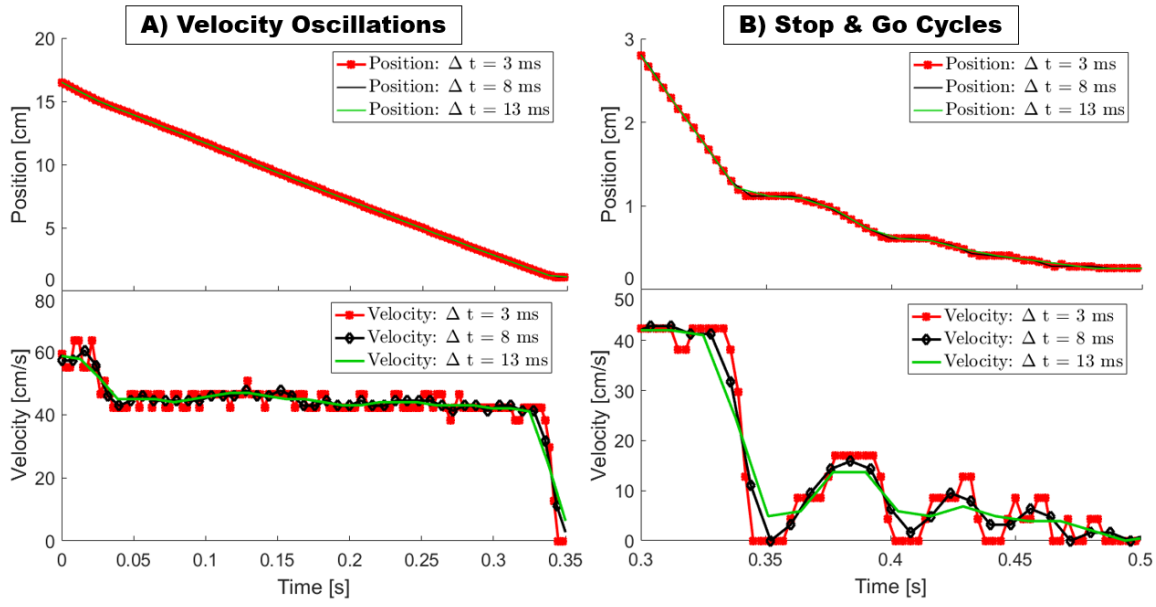

Figure 3.2: Representative wire experiment velocity estimation via undersampling. **A)** *Estimated velocity plots during the bulk velocity oscillations and* **B)** *the Stop & Go cycles for three different time interval lengths.*

It can be seen that it is not trivial to retain the peaks (velocity maximums and minimums) with simple undersampling, because the estimation of velocity over large time intervals results in aliasing, while small time intervals, although capturing the peaks quite well, retain a large portion of the noise in the signal. Second-order central differencing has been found to be of little help for this issue, and thus it was decided to combine low-time-interval undersampling with a separate low-pass

filter on the trajectory data prior to the calculation of velocity.

Undersampling combined with Savitzky-Golay smoothing

The filter chosen for this process was the Savitzky-Golay smoothing low-pass filter [44]. It is a particularly successful filter to smooth the signal in order to reduce noise while still managing to approximately maintain the shape and height of the peaks [45]. It is defined by two parameters, K and M, the former being the order of the polynomial approximation, and the latter defining the number of points in the interval length. It can be used as a weighted moving average, i.e. a smoothing finite impulse response (FIR) filter, but also as a differentiation filter. In this work, the filter has only been employed as the former.

It is essentially a method of data smoothing based on the fit of a local polynomial which minimizes the squared error E of a data subset of adjacent points and evaluation of the resulting polynomial at a single point within the approximation interval according to

$$p(n) = \sum_{k=0}^{K} c_k n^k \text{ fit to minimize the squared error } E = \sum_{n=(1-M)/2}^{(M-1)/2} \big(y(n) - p(n)\big)^2 \tag{3.3}$$

where $y(n)$ and $p(n)$ are the observed data and the fitted polynomial, respectively, at a point in time n along the signal, while with c_k the convolution coefficients are denoted. Savitzky and Golay suggested that so long that the data points are equally spaced, a single set of convolution coefficients can be obtained from the analytical solution of the least-squares criterion (obtained by substituting the polynomial equation into the squared error, taking its derivatives with respect to the convolution coefficients and setting them to zero) [44].

$$\frac{\partial}{\partial c_k}\left[\sum_{n=(1-M)/2}^{(M-1)/2}\left(y(n) - \left(\sum_{k=0}^{K} c_k n^k\right)\right)^2\right] = 0 \tag{3.4}$$

This single set of convolution coefficients can be applied to all data subsets as the filter progresses along the signal by taking the next adjacent point after $(M\text{-}1)/2$ points to the right and removing the last data point of the subset (found $(M\text{-}1)/2$ data points to the left) [44] [45]. All filter specification values are summarized in table B.1.

3.2 1D MRI processing

This section will deal with the image and signal processing involved in the analysis of the 1D MRI measurements. All processing was performed in MATLAB.

3.2.1 Vertical trajectory

The raw MRI data comes in a three-dimensional matrix form of size $N_y \times N_t \times N_{dyn}$. Because of the overlapping field of view of the four RF coils during parallel imaging, the matrix needed to be stitched together in order to obtain a single time versus vertical intensity image as shown by **A)** of figure 3.3.

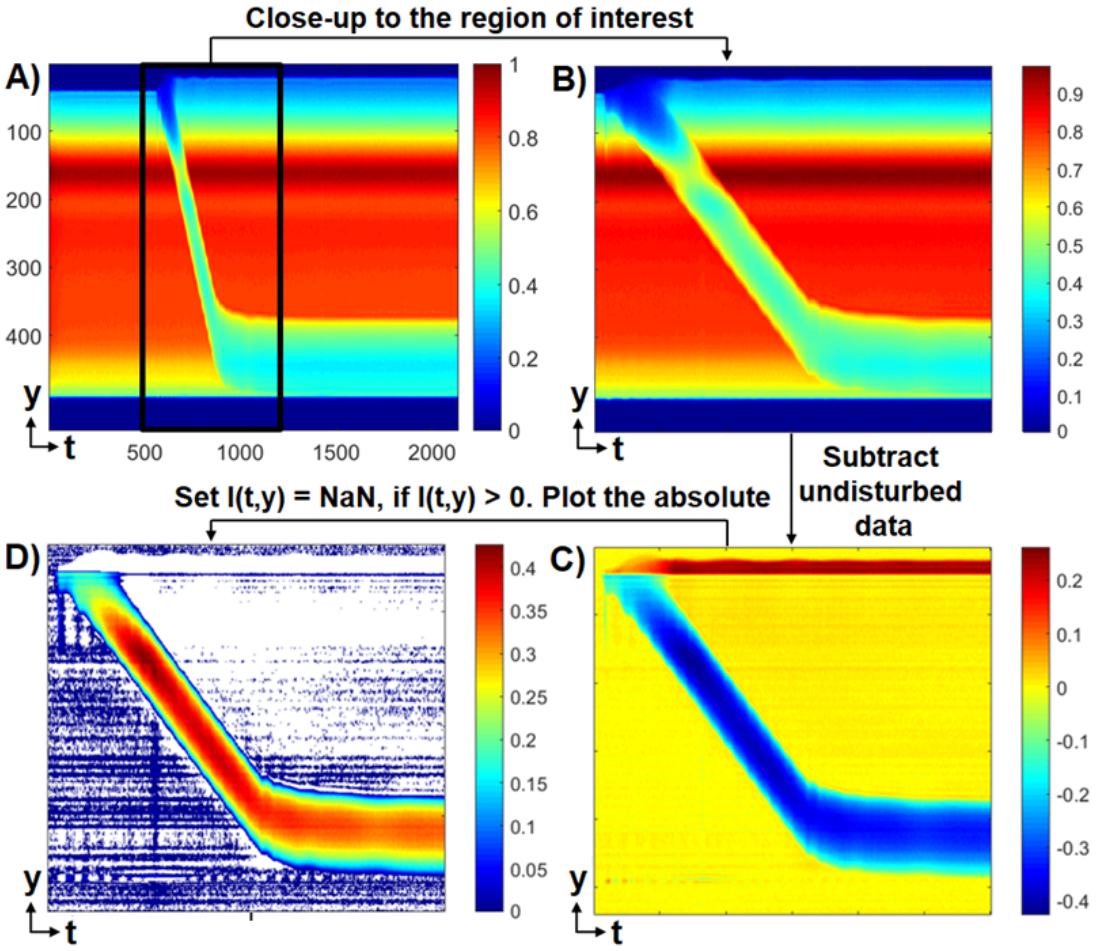

Figure 3.3: Sequence in 1D MRI Filtering. **A)** *Stitched MRI image.* **B)** *Close-up image to the region of interest.* **C)** *All vertical intensity undisturbed data during $t = 0$ s is subtracted from the entire domain along the time axis. All pixel intensity values above 0 are set to 'NaN' and shown in the image in* **D)** *where the 'NaN' values are depicted in white.*

After a close-up to the desired image from which information about the vertical trajectory of the intruder can be obtained, the initial undisturbed vertical intensity y-column at time $t = 0$ s prior

to penetration is subtracted from the entire image domain along t. This act yields an image which shows the desired signal of the intruder with intensity $I(t, y) < 0$. Therefore, in order to filter out the rest of the intensity map and get rid of the surface waves that form on the top of the suspension (shown in distinctive red colour in part **C)** of figure 3.3), all intensity values which are positive are set to a designation 'Not a Number' (NaN). The absolute of all intensity-weighted pixels is then taken and the result is shown in part **D)** where the white colour depicts the NaN values. Because of the fact that the entire signal of the interested region used to be negative, this entire process up to and including part **D)** did not corrupt the signal at all. Even so, it can still be observed that a lot of noise remained in the bulk of the suspension, and this noise being of the same order of magnitude as the lower and upper signal intensity edges which represent the intruder surface causes an issue which needs to dealt with.

The first solution that comes to mind is simple thresholding of the entire image. However, with this method the edges of the intruder would get corrupted alongside with the removal of background noise. The intensity in the interior of the intruder signal varies significantly, and therefore simple thresholding has been ruled out as a method of robustly finding the vertical trajectory from the 1D MRI signal. Instead, two alternative methods have been used to automatically filter out the data and obtain the time versus trajectory plots from the MRI signal.

Gaussian filtering

A two-dimensional Gaussian smoothing kernel was applied to the image. This method for smoothing and getting rid of background noise is essentially the widely used in image processing non-uniform low pass Gaussian filter whose kernel coefficients diminish with increasing distance from the center of the kernel. These kernel coefficients are sampled from the two-dimensional Gaussian function [46]

$$G(t, y) = \frac{1}{2\pi\sigma^2} \mathrm{e}^{-\frac{t^2+y^2}{2\sigma^2}} \tag{3.5}$$

where σ is the standard deviation of the distribution. It was modified manually for every image.

The method of trajectory detection using this filter was split into two regions as shown by figure 3.4. In the light-blue coloured area, the intruder has not yet penetrated fully into the suspension, thus the only visible Gaussian tail is the lower (found closer to the bottom of the suspension) one. For this region the detection algorithm is illustrated on the bottom left-hand side of the figure: specifically, the vertical position of the edge of the Gaussian tail is found for every time frame and

is then appended to a MATLAB array. In the region beyond the point where the intruder is fully submerged into the suspension, two particular methods were employed:

- Both Gaussian tails are obtained for every frame, and then the vertical position of the intruder is acquired by estimating the middle point between the two Gaussian tails.
- The median of the Gaussian is calculated by multiplying the found maximum intensity signal along the vertical direction $max\left(G(t)\right)$ at the particular time frame by a factor F (approximately ranging from 0.5 to 0.75 to avoid the noise below) and taking the middle point between the left and right limits.

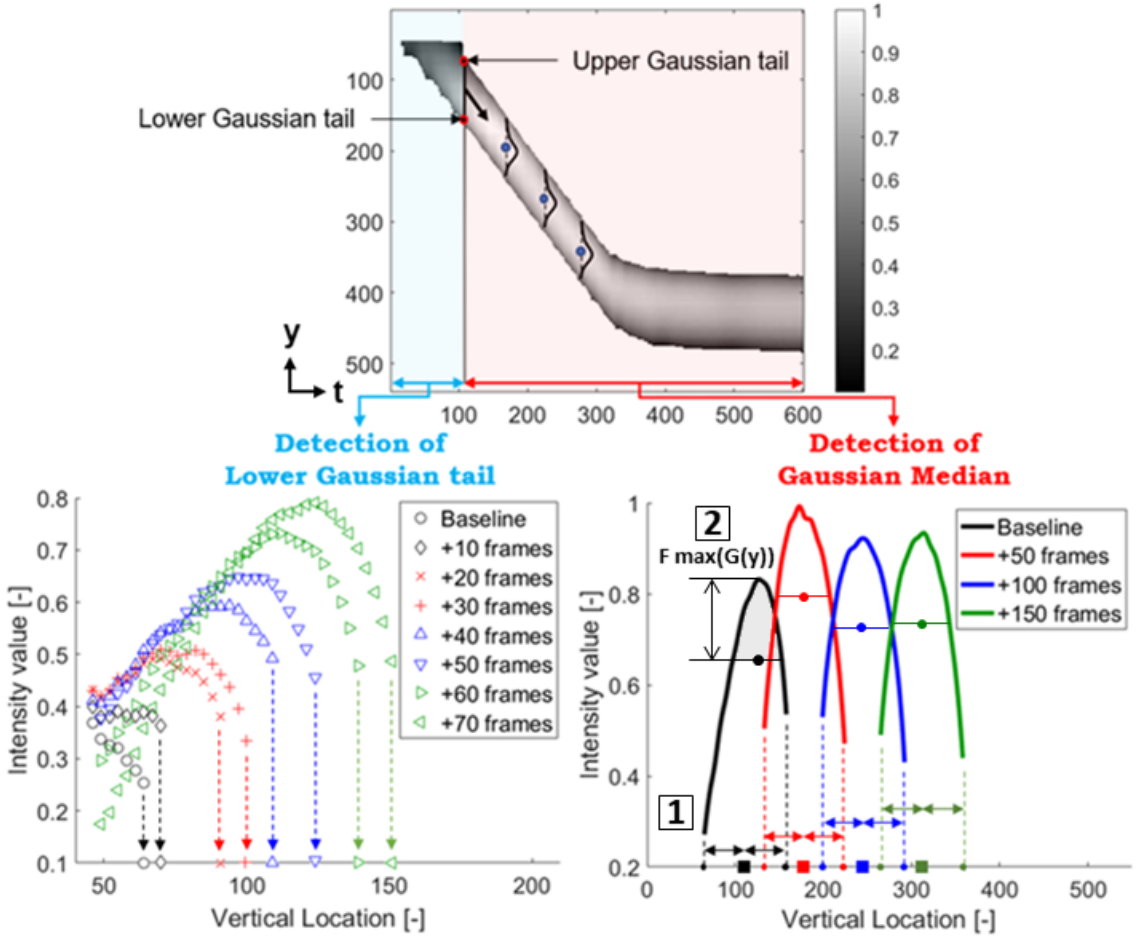

Figure 3.4: Gaussian filtering to obtain trajectory. An image showing a two-dimensional Gaussian filter performed on the data. In order to obtain the final vertical velocity plot, two distinct methods were used: detection of the Lower Gaussian tail up to the time frame at which the full size of the intruder has penetrated into the suspension, and a detection of the Gaussian Median beyond this frame. The latter was achieved in two ways, shown as in text boxes designated as '1' and '2'.

These methodologies for the second detection region were necessary because edge detection there would compromise the obtained trajectory in case the intruder undergoes $\hat{z}$-direction motion and leaves the XY plane. Moreover, they were employed instead of tracing the location of the maximum

intensity because it was found to vary significantly as a result of random noise.

Normalized cross-correlation algorithm

The second method for tracking the intruder trajectory in 1D MRI experiments was performed by setting up a one-dimensional kernel template spanning through the desired edge at the first point in time, and then applying the normalized cross-correlation algorithm to track the edge. The methodology was only employed for the first detection region, specifically for the time duration that the sphere is not yet fully-immersed in the suspension.

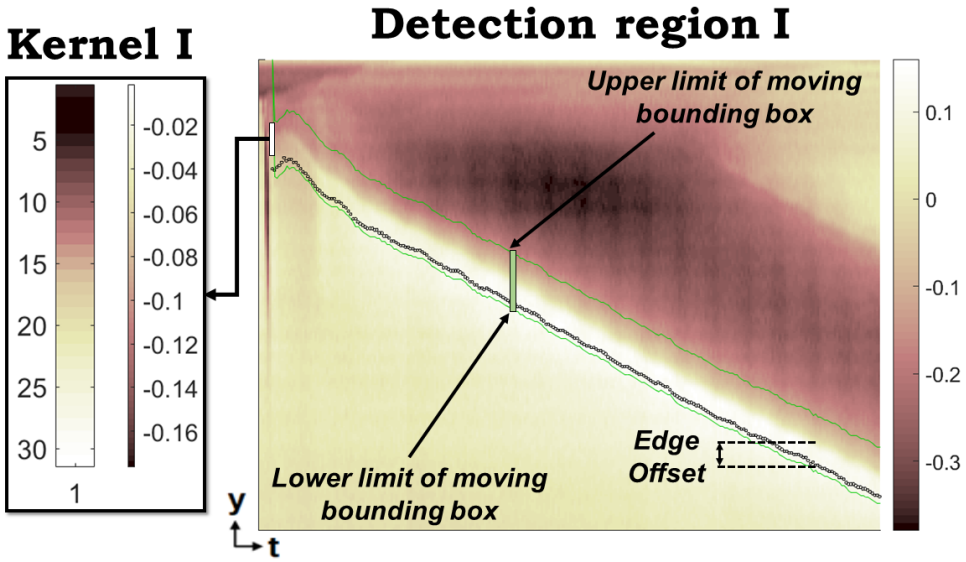

Figure 3.5: Normalized cross-correlation method to obtain trajectory. **A)** *In the first detection region the lower edge is detected using Kernel I after subtracting the vertical data from the domain.* **B)** *In the region after the intruder has fully penetrated into the suspension, the upper intruder edge is detected using Kernel II (shown in a white rectangular box) on the raw data.*

Letting $I(t, y)$ represent the intensity value of the image I of size $M_\mathrm{t} \times M_\mathrm{y}$ and the kernel to stand for the intensity $K(t, y)$ of the intruder template of size $1 \times N_\mathrm{y}$, in order to calculate the position of the observable edge of the intruder in the image $I(T_\mathrm{edge}, Y_\mathrm{edge})$ the normalized cross-correlation value γ is evaluated at each point (T, Y) as

$$\gamma = \frac{\sum_{t,y}\left[I(t,y) - \bar{I}_{T,Y}\right]\left[K(t-T, y-Y) - \bar{K}\right]}{\sqrt{\sum_{t,y}\left[I(t,y) - \bar{I}_{T,Y}\right]^2 \sum_{t,y}\left[I(t-T, y-Y) - \bar{K}\right]^2}} \tag{3.6}$$

in which $\bar{I}_{T,Y}$ denotes the mean of $I(t,y)$ within the area of the kernel K shifted to (T,Y) (estimated with equation 3.7), while $\bar{K}$ stands for the mean value of the kernel itself.

$$\bar{I}_{T,Y} = \frac{1}{N_\mathrm{t} N_\mathrm{y}} \sum_{t=T}^{(T+N_\mathrm{t}-1)} \sum_{y=Y}^{(Y+N_\mathrm{y}-1)} I(t,y) \tag{3.7}$$

Due to the normalization of the variance of the zero-mean image function $I(t,y) - \bar{I}_{T,Y}$ and the shifted zero-mean kernel function $K(t-T, y-Y) - \bar{K}$ in the denominator of equation 3.6, the normalized cross-correlation value $\gamma(T,Y)$ remains independent to changes in brightness or contrast of the image [47]. The desired position of the intruder edge $(T_\mathrm{edge}, Y_\mathrm{edge})$ is then just the maximum value of γ.

In order to apply this methodology, firstly, the stitched 1D MRI vertical intensity data from the first time frame is subtracted from detection region I in a manner shown in figure 3.4. A 1D kernel of size $N_{\mathrm{y,\ kernel}}$ is then manually chosen to track the lower edge of the intruder. The kernel is then applied to an image in a bounding box of size $N_{\mathrm{y,\ box}} = N_{\mathrm{y,\ kernel}} + N_{\mathrm{allowed\ movement}}$, where the latter is a fixed value of vertical pixels which restrict the intruder's movement. This is because, occasionally an edge is detected in a location far from the observable signal of the intruder. The bounding box shifts with one time pixel delay with respect to the next iteration in a loop which finds the location of the edge using the normalized cross-correlation algorithm.

3.2.2 Vertical velocity and acceleration

The vertical velocity and acceleration have been found using both a Savitzky-Golay filter and undersampling of the trajectory signal. The undersampling factor employed was not nearly as large as it was for the wire experiment because the temporal resolution of the 1D MRI experiments averaged $t_\mathrm{res} \approx 5.5$ ms which was significantly higher than the $t_\mathrm{res} \approx 0.33$ ms raw high-speed camera time duration of acquisition. All detection methods and filter specification values are summarized in table B.2.

3.3 2D MRI processing

This section will tackle the image and signal processing involved in the analysis of the 2D MRI measurements. All processing was performed using MATLAB in combination with the MRecon interface (ReconFrame 3.0, GyroTools LLC, Zurich, Switzerland).

3.3.1 Pre-processing of data

The raw 2D MRI position and velocity data come into three four-dimensional matrices of size $\boldsymbol{A}_{\mathbf{size}} = [96 \times 96 \times 250 \times 2]$, where the first two columns contain the parameter acquired in the $\hat{x}$ and $\hat{y}$ directions, respectively, and the third dimension denotes the number of dynamics (time frames). The fourth dimension in the position data switches the parameters between signal intensity and spin density, and between velocity component (v_{x} or v_{y}) and spin density for the two velocity-encoded data matrices.

In order to achieve a better spatial resolution for derivative smoothing and imaging purposes, the data was resized using MATLAB's 'imresize' function to matrix sizes for all three matrices of $\boldsymbol{A}_{\mathbf{size}} = [400 \times 400 \times 250 \times 2]$. This is achieved through a bicubic interpolation on four adjacent points using the model

$$f(x,y) = \sum_{i=0}^{3}\sum_{j=0}^{3} a_{i,j}x^i y^j \tag{3.8}$$

where $f(x,y)$ is the interpolated image and i and j span from 0 to the order of the interpolation [48].

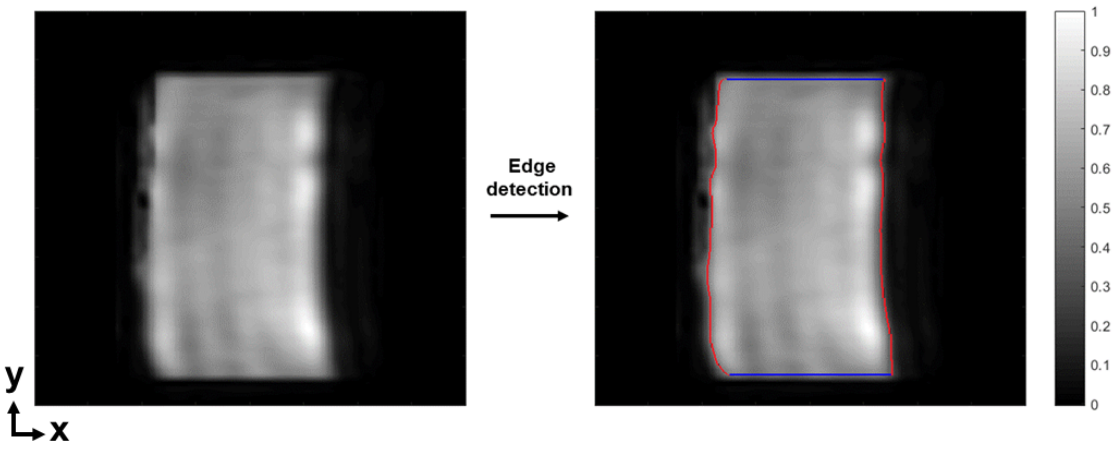

Figure 3.6: Edge detection for phase wrapped-around boundaries of the container achieved through thresholding for the experiments of May 2018 only.

The next pre-processing step taken was to set the boundaries of the suspension. While during the experiment sessions that took place in January and March 2018 (the tables of experimental data settings were shown in tables 2.1 and 2.2) the image only needed to be set field of view limits in the $\hat{x}$ and $\hat{y}$ directions, the experiment session that occurred in May 2018 required an edge detection algorithm to detect the edges of the container filled with suspension because the raw MRI signal

came distorted at its sides due to phase wrap-around artifacts. This particular MR artifact occurs whenever the dimensions of the imaged object exceed the prescribed imaging field of view by the operator. Nevertheless, this slightly pronounced artifact did not cause an issue to the legitimacy of the experiment session so long that the edges of the cylinder (as shown by figure 3.6) are detected and information from their exterior is excluded from the analysis. To detect these edges a simple thresholding factor ($\theta_{\text{cyl}} = 0.45$) was defined on the first frame of the signal intensity data from the position matrix $\boldsymbol{A}_{\text{position}}$ and two resultant arrays of left and right edge limit values in the x-direction, respectively, were obtained. The use of these limits setting the boundaries of the cylinder in the first frame has been extended to all other remaining time frames and the velocity-encoded data.

3.3.2 Intruder trajectory

Obtaining the trajectory of the intruder from the 2D MRI measurements has been a challenge to automate for all experiments. To tackle this challenge, an attempt was made to minimize all manual inputs for the data analysis of all the experiments. Specifically, the intruder's trajectory was obtained by manually setting up a two-dimensional kernel template image of the intruder at the point in time at which the intruder has penetrated deeply enough into the suspension, and then the intruder centroid was acquired via the normalized cross-correlation algorithm.

In this case $I(x, y)$ represents the intensity map of size $M_{\text{x}} \times M_{\text{y}}$ and the kernel intensity map $K(x, y)$ is manually set up to calculate the position of the centroid of the intruder in the image $I(X_{\text{cent}}, Y_{\text{cent}})$ via obtaining the local maximum of the normalized cross-correlation value γ using equation 3.6 rewritten as

$$\gamma = \frac{\sum_{x,y} \left[I(x,y) - \bar{I}_{X,Y}\right] \left[K(x-X, y-Y) - \bar{K}\right]}{\sqrt{\sum_{x,y} \left[I(x,y) - \bar{I}_{X,Y}\right]^2 \sum_{x,y} \left[I(x-X, y-Y) - \bar{K}\right]^2}} \tag{3.9}$$

where the bars above the variables stand for their mean values and are calculated in an identical manner as in equation 3.7. The estimated position of the centroid $(X_{\text{cent}}, Y_{\text{cent}})$ is obtained by horizontal and vertical position indices of the maximum value of γ.

The used kernel was defined manually for the time frame that provided the most pronounced signal of the intruder by looking qualitatively into the individual MR image dynamics. The normalized cross-correlation algorithm was then applied to all other image dynamics using the same kernel in order to obtain the locations of both horizontal and vertical positions of the centroid of the intruder. Upon acquiring these, an artificial mask of a perfect sphere with a diameter exactly

matching the physical size of the intruder is mapped with 'NaN' values on top of the intruder as shown by image 3.7.

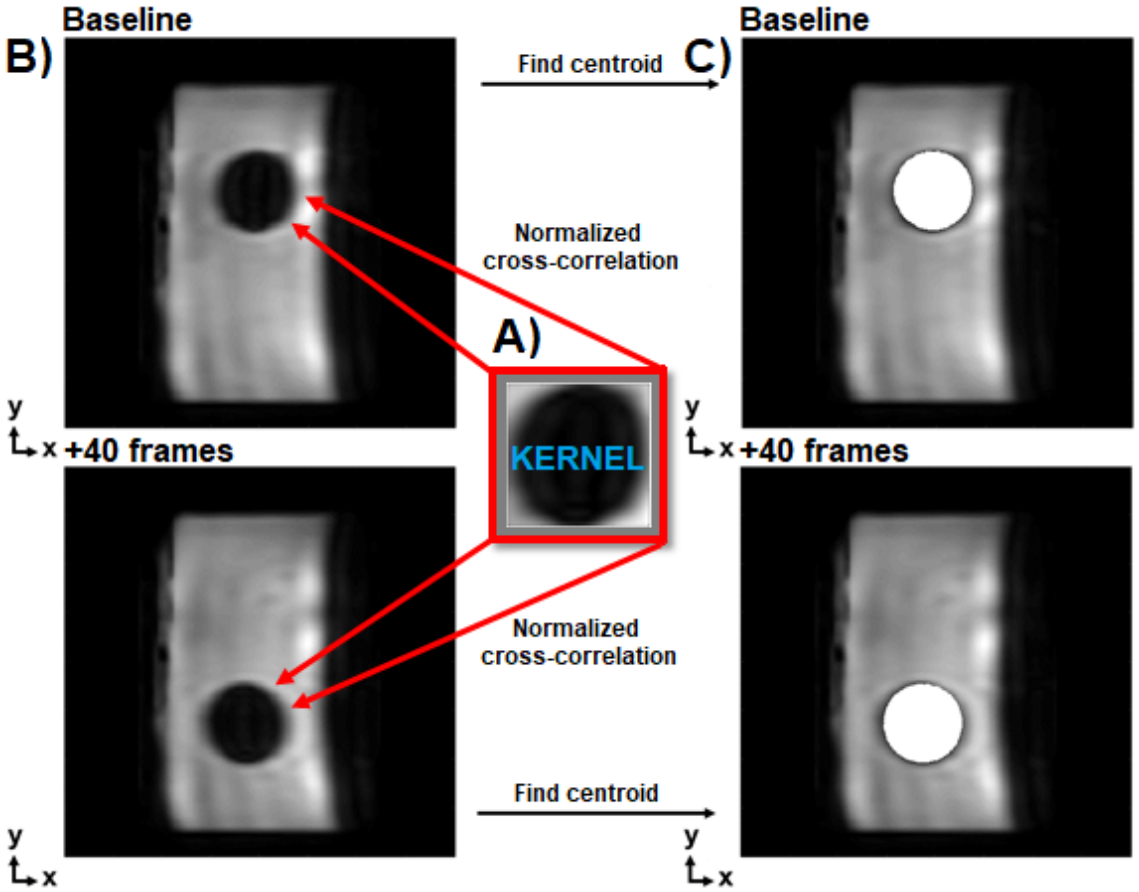

Figure 3.7: Masking sequence in 2D MRI. A kernel is chosen manually from a time frame that yields the most evident signal and is then applied via the normalized cross-correlation algorithm to the remaining time frames in order to obtain the centroid of the intruder. An artificial spherical mask of 'NaN' values is then constructed around the centroid and a number of adjacent pixels are added to it when computing velocity of the suspension.

3.3.3 Intruder velocity and acceleration

The intruder velocity and acceleration were calculated directly from first or second order difference for all MR measurements in both $\hat{x}$ and $\hat{y}$ directions, essentially avoiding the undersampling stage because the temporal resolution was already too large and, in fact, beyond the limit to capture the velocity oscillations in the bulk of the suspension.

3.3.4 Suspension velocity

The suspension velocity in the domain is a MRI measurement output which did not need any special signal processing treatment, except for a small extension of the mask described above by a certain amount of adjacent pixels $N_{\text{adj,px}}$ around it. This was particularly important because the

velocity-encoded data experienced phase wrapping inside the intruder, and therefore the velocities in the interior were measured an order of magnitude higher than their surroundings (clearly not physically expected to change at all).

4 Results & Discussion

This chapter will present the results of the data analysis of the experiments and will discuss whether the initial research goals and objectives have been met. First of all, relationships of shear stress, shear rate and viscosity obtained by reference rheology experiments documented in the literature will be provided and discussed in section 4.1. Section 4.2 will demonstrate and compare the intruder trajectories obtained from the wire, 1D MRI and 2D MRI trajectory measurements. After that, section 4.3 will show the velocity fields and shear rate patterns of the suspension beyond the point in time that the intruder has fully penetrated, and will accompany those with a brief qualitative discussion. Shear rate relations in the bulk of the suspensions are obtained and combined with the reference rheology experiments in the literature with the objective to establish a link to jamming in section 4.4. Finally, section 4.5 will provide a qualitative description of a novel hypothesized physical mechanism causing a newly-observed phenomenon just after the impact region.

4.1 Rheology of cornstarch suspensions

The cornstarch suspension rheological experimental results were obtained from Madraki *et al.*. They used several density-matched (cornstarch-water-CsCl) cornstarch suspensions, two of which $\phi_{\mathrm{s,\ ref}} = 0.41$ and $\phi_{\mathrm{s,\ ref}} = 0.439$ almost exactly matched the packing fractions of the non-density-matched suspensions used in this work, i.e $\phi_{\mathrm{s}} = 0.41$ and $\phi_{\mathrm{s}} = 0.44$ [49]. It has been observed previously by von Kann *et al.* that density-matched suspensions show equivalent results to non-density matched ones, so long that the latter is continuously stirred prior to the experiments, and therefore it has been assumed that the rheology data would not differ for both [2].

The reference rheological measurements were conducted with a DHR-3 rotational rheometer from TA Instruments using a serrated parallel plate geometry of 40 mm diameter with 90 degree V-shaped grooves of height 0.5 mm and width 1 mm (see part **D)** of figure 4.1). This geometry was particularly chosen by Madraki *et al.* in order to eliminate the wall slip effects. Essentially, the desired amount of material is sandwiched between the two crosshatched plates, a certain torque C and rotation rate Ω are generated by the device, and then the maximum shear stress and shear rate are determined from the relationships

$$\tau = \frac{2C}{\pi R^3} \text{ and } \dot{\gamma} = \frac{\Omega R}{h}, \tag{4.1}$$

respectively. The effective viscosity is consequently computed from $\eta = \tau/\dot{\gamma}$ [49]. The figures clearly illustrate the continuous and discontinuous shear thickening regimes and their transition point (the critical shear rate $\dot{\gamma}_{\mathrm{c}}^{0}$ at which the discontinuous jump in the effective viscosity occurs.

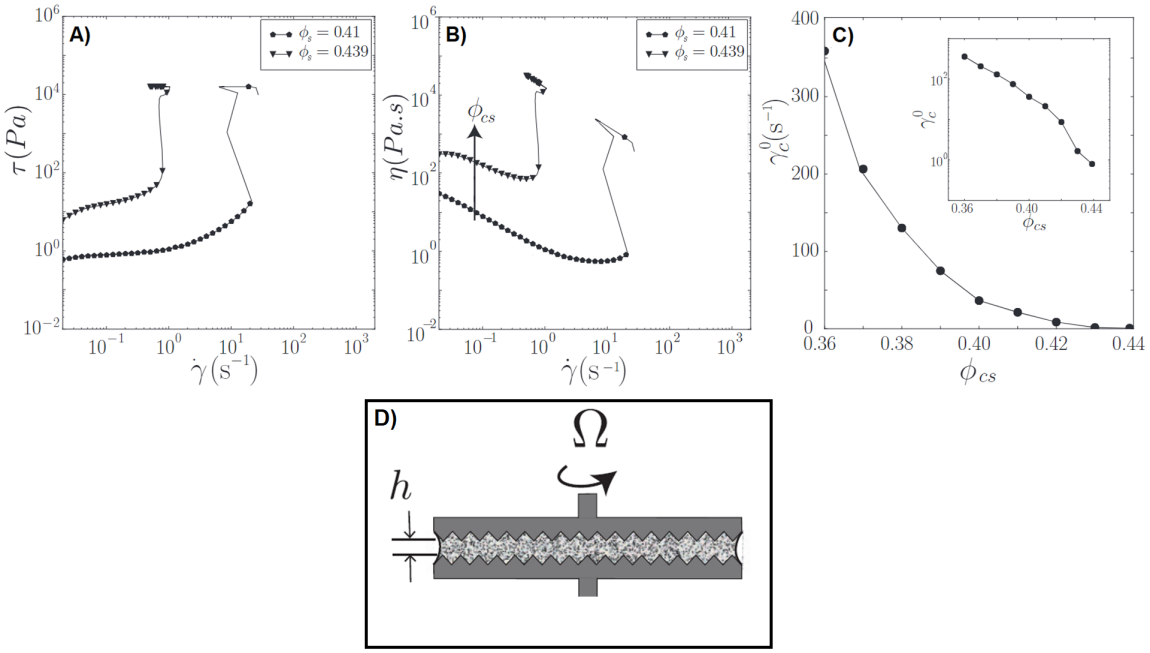

Figure 4.1: Rheology of cornstarch suspensions. **A)** *Shear stress* τ [Pa] *vs. shear rate* $\dot{\gamma}$ [s^{-1}] *and* **B)** *viscosity* η_s [Pa · s] *vs. shear rate* $\dot{\gamma}$ [s^{-1}] *for pure cornstarch suspensions at different packing fractions* ϕ_s. **C)** *DST critical shear rate* $\dot{\gamma}_c$ *vs.* ϕ_s. *The inset shows the same plot in a semilog scale.* **D)** *Sketch of the plate-plate rheometer exhibiting the manufacturing grooves. Adapted from* Madraki *et al.* [49]. *Copyright 2018 Physical Review Fluids.*

4.2 Intruder trajectory tracking

The trajectory was tracked in all types of experiments performed. Subsection 4.2.1 will present the results obtained from the wire experiments, in which the vertical motion of the intruder allowed to move only in the vertical direction is tracked. In subsection 4.2.2 the results for the undisturbed intruder motion obtained from the 1D and 2D MRI measurements will be presented. Lastly, the differences between the experiments and the new gained insights will be explained in subsection 4.2.3.

4.2.1 Trajectory acquired from the wire experiments

Several wire experiments were performed as a reference to qualitatively observe the vertical trajectories of intruders in cornstarch suspensions exhibiting intermediate to severe shear thickening. As previously discussed, MRI experiments are costly, thus it could not be afforded to adjust suspension packing fractions until achieving the optimum for the experimental conditions at hand during the scheduled MR scan sessions. This is why several packing fractions were tested with the same three plastic hollow balls of different diameters and buoyancy-corrected masses ($\mu = m_{\text{sphere}} - 4/3\pi r_{\text{cyl}}^3 \rho_{\text{sus}}$) filled with ZrO_2 granules, similar free fall heights (ranging between 1 and 1.5 cm from the top of

the suspension surface to the bottom of the intruder), falling into the same bed fill height of the suspension (16.5 cm) in the same cylindrical container. The main idea was to obtain a combination of suspension packing fractions and intruder properties for which two subsets of phenomena can be tested with the MRI:

- relatively fast, dynamic and clearly pronounced velocity oscillations and stop & go cycles, whose details are still possible to be fully-captured by 1D MRI temporal resolution.
- relatively slower and clearly pronounced slow-down behaviour near but below the critical packing fraction beyond which isotropic jamming occurs and the suspension starts to act as a yield-stress solid. This would be the closest possible regime that would enable the 2D MRI temporal resolution to also capture its details, in addition to the 1D MRI.

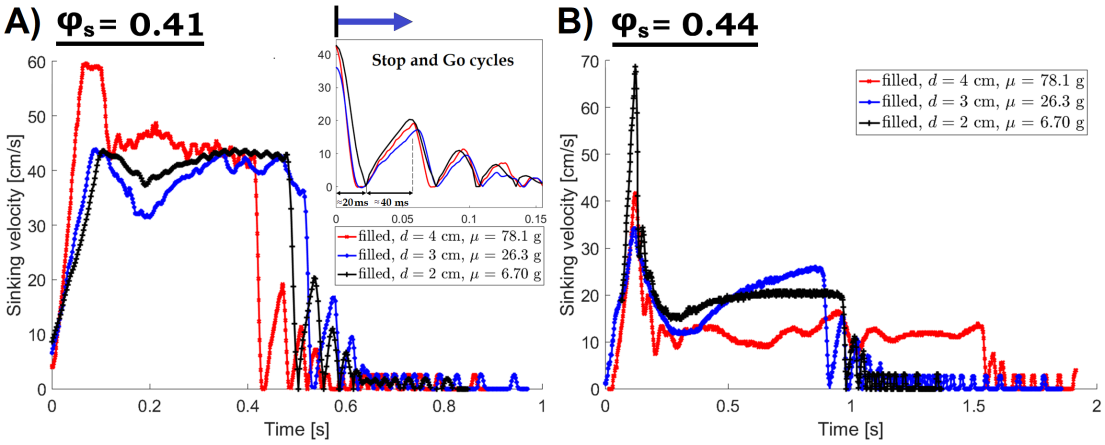

Figure 4.2: Wire experiments of three intruders of different sizes and buoyancy-corrected masses settling in cornstarch suspensions of packing fractions **A)** $\phi_s = 0.41$ *and* **B)** $\phi_s = 0.44$. *In the inset plot the first stop cycle is overlapped for the three intruders: similar amplitudes and frequencies of the rest of the cycles are observed.*

It was found that when the intruders settle in the suspension, the phenomena that were predicted by von Kann *et al.*'s experiments were indeed present: the ball reaches a certain impact velocity in a linear fashion during free fall because the air drag resistance is too small to take effect, an unstable regime of oscillations transitions into stable velocity oscillations around a terminal velocity before a sudden stop due to higher viscous effects near the container base occur. This motion stop is likely caused by compressive stresses building up to a point in which a jammed network of particles forms between the intruder and the container base. A relaxation process then takes place as the stresses build up in the network and the interstitial fluid, eventually triggering a Darcy's flow in the porous medium constructed by the cornstarch grains and allowing the system to relax through small particle rearrangements. The region unjams through this act and the object starts moving again only to stop a little closer to the container base [2].

In the suspension of packing fraction $\phi_s = 0.41$ one can notice that only the small filled ZrO_2 ($d = 2$ cm) and medium-sized filled ZrO_2 ($d = 3$ cm) spheres were released from the same height, i.e. approximately $H_{\text{free fall}} = 1$ cm, resulting in an impact velocity of $V_{\text{impact}} = 45$ cm/s. The difference of about 25% in impact velocity between the large filled ZrO_2 ball ($d = 4$ cm, reaching $V_{\text{impact}} \approx 60$ cm/s) and that of the other two sizes is clearly an issue for the unstable oscillations near the impact and the time duration of sinking. Furthermore, it cannot be judged whether the largest ball reaches terminal velocity (it is seen to decrease in time) within the time frame of the wire experiment in the low packing fraction. For these reasons no meaningful comparison can be achieved from this, and therefore we shift our attention to the small and medium-sized spheres.

It can be stated that the stabilized terminal velocity reached by the smallest object is higher than the reached terminal velocity by the medium-sized one for the same impact velocity. A larger amplitude of bulk oscillations is clearly visible for the larger intruders, while in the stop-and-go cycles region there is hardly any difference in the re-acceleration peak amplitudes or frequencies. All intruders' bulk velocity oscillations share an approximate time period of oscillations of 25 ms (or approximate frequency of 40 Hz), while near the bottom the initial stop occurs over an approximate 20 ms period and is followed by a velocity rise period spanning approximately 40 ms. The time scale of the stop and go cycles then gradually decays to about 10 ms after three or four cycles in a similar fashion for all intruders (see figure 4.2). Beyond this point, the spatial resolution is too small to capture any distinctive cycles.

In the denser suspension ($\phi_s = 0.44$, the small-sized sphere show a considerable difference in impact velocity relative to the others which may likely affect, once again, any comparisons made. A relevant observation from this data which can be made is that the large and medium-sized ZrO_2 sphere experimental results demonstrate very clearly that higher size and mass leads to a reduction in the oscillating velocity mean, therefore an increase in the time duration of oscillations and the overall time duration of sinking.

When comparing the behaviours in the two suspensions, it is generally seen that, for a larger packing fraction, terminal velocity is considerably lower for all intruders. Regardless of impact velocity differences, the sinking period in the $\phi_s = 0.44$ suspension is considerably higher than for the $\phi_s = 0.41$ suspension (note the difference in the x-axis limits). These comparison results are found to be in good agreement with the conclusions drawn from von Kann *et al* via examining packing fraction effects in the $\phi_s = [0.35 : 0.41]$ range for the same 1.6 cm diameter steel intruder [2]. By keeping a constant free fall height, they also observed an increase in amplitude and time period for both the velocity oscillations and stop-and-go cycles when the suspension is more packed.

These effects are not clearly seen in the wire experiments of the medium and small-sized intruders performed in this thesis work, and this is trusted to be due to the following issues in the setup:

- Due to the gap between the rod and the wire (refer back to section 2.1 for more details), a slight wobbling of the wire would have caused improper positioning of the marker when an asymmetrical stress acts on the intruder and causes it to move sideways. This gap was intentionally left to avoid friction between the rod and the wire, but it was not the optimal side.
- The undersampling and Savitzky-Golay filtering were performed in such a way to reduce noise in the signal prior to velocity calculation; although it does help with smoothing velocity, it may have harmed the peaks of the velocity oscillations.
- Sedimentation could have taken place due to difficulty to reach the container base while mixing. This issue was overcome in the MRI experiments by mixing more frequently (the MRI experiment cycle takes less time than that of the wire because it takes significant amount of time to unload the stored data from the high-speed camera onto the hard drive, while in the MRI this process happens instantaneously) and removing the suspension from the container every approximately 20 minutes to mix it in a larger one.
- Impact velocity differs considerably for the small-sized intruder (comparing the experiments with the two packing fractions).

Because of these issues, as reported earlier, the wire experiments were mainly used as a reference for intruder behaviour - to obtain time scales and know what to expect, while the 1D MRI experiments were used as criteria for qualitative comparison of the physical behaviour of the intruder.

4.2.2 Trajectory acquired from the MRI experiments

MRI experiments were carried out for settling spherical intruders in two distinct packing fractions: $\phi_s = 0.44$ for the filled ZrO_2 plastic spheres (diameters of [2, 3, 4] cm and density $\rho_{\text{filled}} \approx 3200$ kg/m^3) and $\phi_s = [0.41; 0.44]$ for the solid ZrO_2 spheres (diameters of [2; 3; 4.28] cm and density $\rho_{\text{solid}} = 6000$ kg/m^3).

In the MRI experiment data the maximum velocity of the intruder after the free fall has to be calculated as the MRI data only observes what happens after the impact. The free fall heights are measured from the bottom of the fixed PVC tube (located at 25.5 cm from the cylinder base) to the suspension surface, allowing for an impact velocity to be calculated as $V_{\max} = \sqrt{2gh_{\text{free fall}}}$ by assuming negligible air resistance. The measured free fall heights and estimated maximum velocities are illustrated in figure 4.3. For more information about the setup, please refer back to tables 2.1 and 2.2.

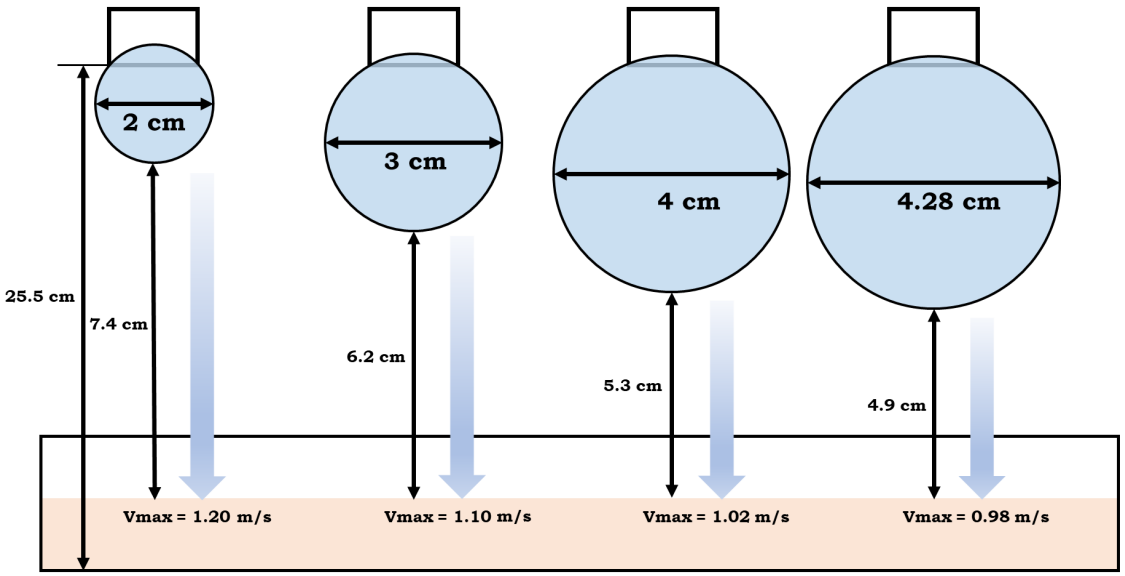

Figure 4.3: Drop heights and calculated maximum velocity in MRI experiments. The top of the spheres are sucked by the fixed tube of diameter 1.5 cm located at 25.5 cm. Therefore the free fall heights from the lowest point of the spheres to the suspension interface are are approximately $H_{free\ fall} = [4.9, 5.3, 6.2, 7.4]$ *cm, giving maximum velocities of* $V_{max} = [0.98; 1.02; 1.10; 1.20]$ *m/s for the intruders of diameters* $d = 2$ *cm,* $d = 3$ *cm,* $d = 4$ *cm and* $d = 4.28$ *cm, respectively.*

1D MRI: Filled ZrO_2 intruder settling in a $\phi_s = 0.44$ suspension

In total three experiments with the small filled ZrO_2 sphere, two experiments with the medium-sized filled ZrO_2 sphere and one experiment with the large filled ZrO_2 sphere were performed. However, due to the inhomogeneous RF excitation during this experiment session (March 2018) and the relatively short signal for the small and medium-sized intruders, the 1D MRI data for those measurements could not be properly filtered, specifically in the after-impact and the bottom region of the container. Figure 4.4 therefore only shows the sinking trajectory and velocity of the large filled ZrO_2 sphere ($d = 4cm$) which was tracked via the normalized cross-correlation algorithm for edge detection for both regions shown.

At first glance we clearly observe (by the black curve in the first region intensity map) that after the intruder has penetrated to about 15% of its total diameter, a bounce off the suspension occurs. After the subtle bounce, the sphere goes straight into a steady dive and makes a couple of oscillations of higher amplitude and then transitions into stable velocity oscillations, which, interestingly enough, vary for separate regions in terminal velocity. The oscillations clear out at 1.5 s entering a second phenomenological region of lower terminal velocity and then, at about 2.2 s, the intruder undergoes the stop-and-go cycles which are not clearly visible due to noise.

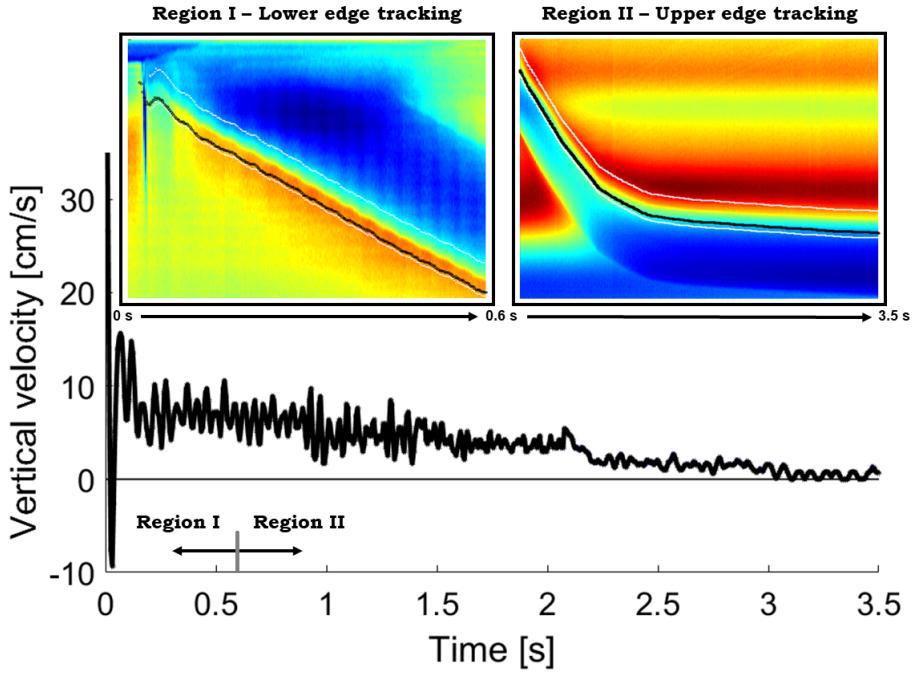

Figure 4.4: Large plastic sphere ($d = 4cm$) filled with ZrO_2 granules sinking in a cornstarch suspension of $\phi_s = 0.44$ with a bed fill height of 16.5 cm, released from a free fall height of 5.3 cm.

1D MRI: Solid ZrO_2 intruders settling in a $\phi_s = 0.41$ suspension

As suggested by von Kann *et al.*, by elevating the buoyancy-corrected mass μ for the same intruder size, a higher amplitude and lower frequency of bulk velocity oscillations and slightly shorter sinking time duration should be observed [2]. This is the reason why it was decided to use solid ZrO_2 balls, as the density is the highest of any easily-obtainable ceramic material, provided that metals could not be employed in the MRI experimental setup because of the strong magnetic fields, as previously explained. It must be noted, however, that these solid ZrO_2 intruder experiments (which showed the most clear behaviour) could only be achieved with the MRI system because the thin wire could not be attached to the ceramic ball.

The most dynamic and most evident bulk oscillations and stop-and-go behaviour out of the experiments completed occurred in the suspension of packing fraction $\phi_s = 0.41$, as depicted in figure 4.5.

In the full domain (part **A)** of figure 4.5), a clear trend is observed for the three differently-sized spheres with different masses but the same inner density ($\rho_{solid} = 6000 kg/m^3$): the overall sinking time increases with sphere mass and size. The stable velocity oscillations in the bulk (excluding the initial effects) have more or less similar frequency and amplitude but their terminal velocity decreases for higher intruder mass and size. Even though the spheres share similar frequency in the stop-and-go cycles region too, it is clearly seen in these particular measurements that the re-

acceleration peak velocities are, in fact, reduced when the mass is elevated by increasing the intruder size. In terms of phenomenology, in none of these regions does the intruder behave in any different manner than expected and previously reported.

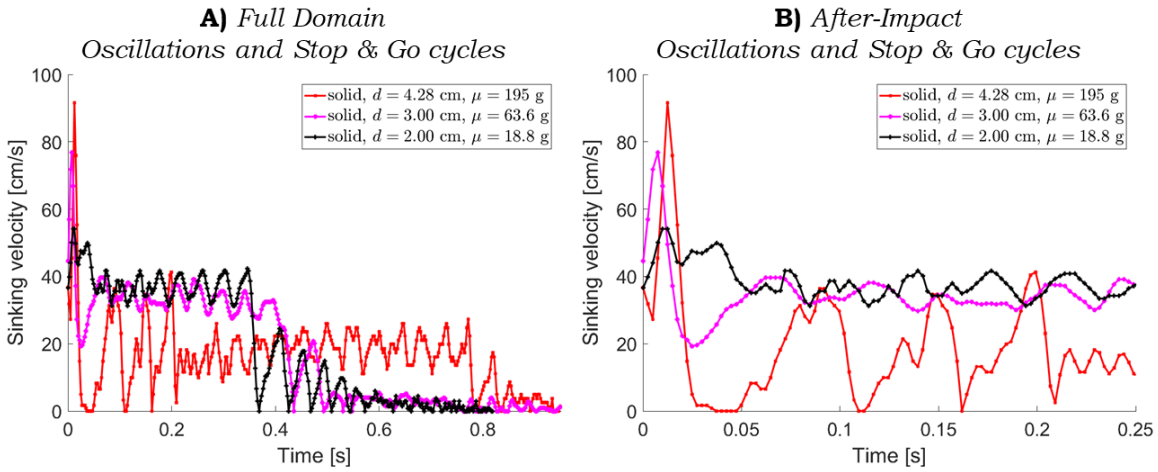

Figure 4.5: Solid ZrO_2 spheres ($d = 4.28$ cm, $d = 3$ cm, $d = 2$ cm) sinking in a $\phi_s = 0.41$ cornstarch suspension with a bed fill height of 16.5 cm. **A)** *Time vs. Sinking velocity of the different intruders for the full domain.* **B)** *Time vs. Sinking velocity of the different intruders for the time period just after the impact.*

However, a third phenomenological region which was not observed in any of the experiments before, makes a striking appearance: stop-and-go cycles develop just after impact. Here and from this moment on a distinction in this thesis work is made between after-impact transient oscillations (or stop-and-go cycles), stable oscillations around the terminal velocity and stop-and-go cycles near the container base. It is illustrated in part **B)** of figure 4.5 that these transient after-impact effects vary from weaker oscillations to moderate oscillations for the small and medium-sized intruders, respectively. The large ball of $d = 4$ cm, however, experiences three full-stop & go cycles before a single high-amplitude oscillation and, eventually, a transition to stable bulk oscillations. From this single set of observations, a conclusion is made that these after-impact effects depend on either the intruder size, the intruder mass or both. More insight is gained about them from the analysis and discussion of the remaining measurements to follow.

1D MRI: Solid ZrO_2 intruders settling in a $\phi_s = 0.44$ suspension

As suggested by the wire experiments performed (described in section 4.2.1), with the rise of the packing fraction ϕ_s it is expected to observe significantly higher settling times for the behaviour of the intruder in the full domain, lower frequencies of stable velocity oscillations in the bulk and lower terminal velocity. If we, for a moment, think about Newtonian fluids, it is expected that this would be the case because the terminal velocity achieved there scales with $\sqrt{\frac{\rho_{intr}-\rho_{fluid}}{\rho_{fluid}}}$, and thus

for higher density fluid the difference is less, resulting in lower steady velocity achieved in the bulk. In suspensions this effect is expected to be even more pronounced because of the non-linear increase in viscosity when it is undergoing shear (CST and DST behaviours). And indeed, part **A)** of figure 4.6 shows that when switching from the $\phi_s = 0.41$ suspension of density $\rho_s \approx 1244$ kg/m^3 to the $\phi_s = 0.44$ suspension of density $\rho_s \approx 1262$ kg/m^3 an astonishing drop of terminal velocity from initially $\approx 40cm/s$ to $\approx 6cm/s$ (85% of its initial value) occurs in the small-sized ball, for instance. This reduction happens despite the fact that the density difference is less than 2%, pointing out the suspension behaviour's extreme dependence on packing fraction local or global changes.

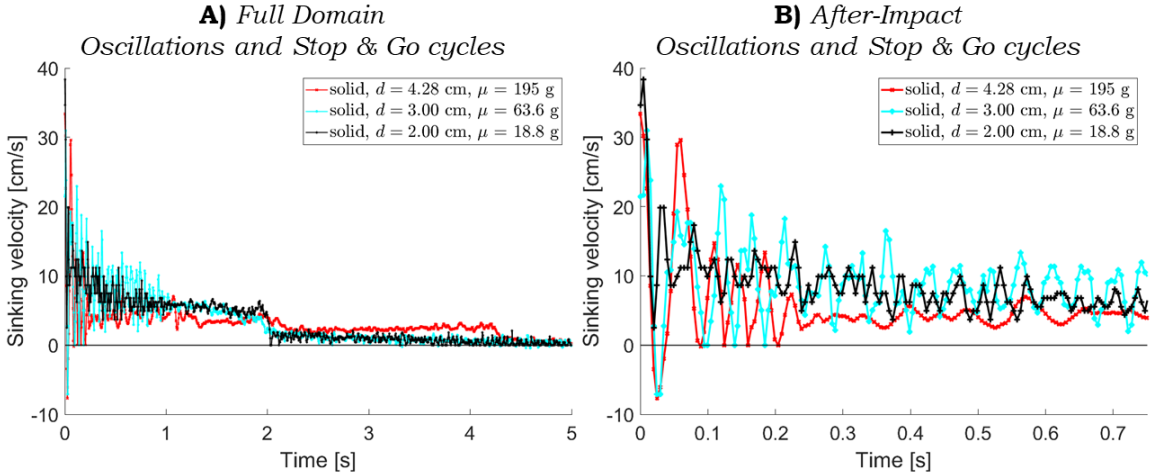

Figure 4.6: Solid ZrO_2 spheres ($d = 4.28cm$, $d = 3cm$, $d = 2cm$) sinking in a $\phi_s = 0.44$ cornstarch suspension with a bed fill height of 16.5 cm. **A)** *Time vs. Sinking velocity of the different intruders for the full domain.* **B)** *Time vs. Sinking velocity of the different intruders for the time period just after the impact.*

The trends observed relative to the intruder size and mass remain the same as for the lower packing fraction, specifically: the overall sinking time is increased and the terminal velocity and magnitude of the velocity peaks in the stop-and-go cycles are decreased when the intruder mass is elevated via increasing size (and once again, keeping the inner density of the intruders constant). Just like the experiment of the large filled ball ($d = 4$ cm), in this experiment, it is also seen that the stable oscillations are split into two distinct regions of two oscillation velocities for the large solid intruder ($d = 4.28$ cm) only. This is a peculiar and unobserved behaviour in the literature. It is hypothesized that this transition to another stable velocity oscillation region around a lower terminal velocity is due to:

- possible movement of the intruder sideways due to rotation or sliding. With closer proximity to the side walls, viscous wall effects may cause a higher shear rate at the side of the wall just below the intruder due to a faster lubrication film layer accelerating upwards around the sphere. As suggested by von Kann *et al.* the velocity oscillations *weaken* in amplitude and

the terminal velocity reduces for experiments of the same conditions but decreased container width. This phenomenon is suspected to be more pronounced for the higher packing fraction because of the lower average settling velocity: the intruder has more time to adjust transversely in the suspension as a result of asymmetry in transverse stresses. In the trajectory tracking subsection of the 2D MRI experiments, it will be checked whether the act of side motion plays a significant role in the sinking of the intruder.

- possible sedimentation due to improper mixing causes the suspension to decrease gradually in local packing fraction from the top to the bottom. This is highly unlikely because extensive mixing took place for a good measure of 5 minutes before each experiment was executed. It was checked via another MRI experiment that at the 15 minutes point in time sedimentation effects become visible. A similar observation is also reported by Waitukaitis and Jaeger [9] and von Kann *et al.* [2].

Part **B)** of figure 4.6 depicts the newly observed after-impact behaviour of the three spherical intruders of different diameters and masses. It is seen that the stop-and-go cycles phenomenon is retained for the large ball in the suspension of higher packing fraction, but now it is also captured in the medium-sized ball. By looking closely into the very first transient oscillation after impact, a vertical bounce off the suspension is observed. This gives a new insight into the phenomenon, which confirms the theory proposed by Waitukaitis *et al.* [9], specifically that the dynamic jamming front beneath the intruder (depicted with red color in figure 1.10) has propagated much faster than the transient motion of the intruder, creating a solid-like jammed region below the sphere while the sphere in this time frame has retained a lot of its energy in order to bounce up the quasi-V-shaped solid-like surface. Although having this initial impact physically explained with the rapidly growing jamming front and cone-like region of added mass that Waitukaitis and Jaeger proposed [9], it does not explain the stop-and-go cycles which occur slightly after that because their experiments show that the relaxation of the solid jammed region take place within milliseconds.

As far as the lightest sphere is concerned, it also does exhibit stronger oscillations with respect to the lower packing fraction and therefore it is safe to assume that at an even higher packing fraction below the critical one for isotropic jamming ($\phi_c \approx 0.46$, as suggested by Peters *et al.* [23]), if released from the same free fall distance, it would most probably also undergo stop-and-go cycles before the decay to stable oscillations.

2D MRI: Filled ZrO_2 intruder settling in a $\phi_s = 0.44$ suspension

The findings of the wire and 1D MRI experiments with filled ZrO_2 spheres suggested that the relative time scales of the oscillations and stop-and-go cycles occur below 50 ms. This is why it was expected that trajectory obtained from 2D MRI would not be sufficient because of its temporal resolution of 65.5 ms. Nevertheless, it is seen in a comparison between 1D MRI and 2D MRI for the large sphere in figure 4.7 that the terminal velocity is retained, and essentially, aliasing is present on the quasi-sinusoidal decaying bulk oscillations. However, the after-impact effects were not captured and the stop-and-go cycles appear as a gradual slow-down.

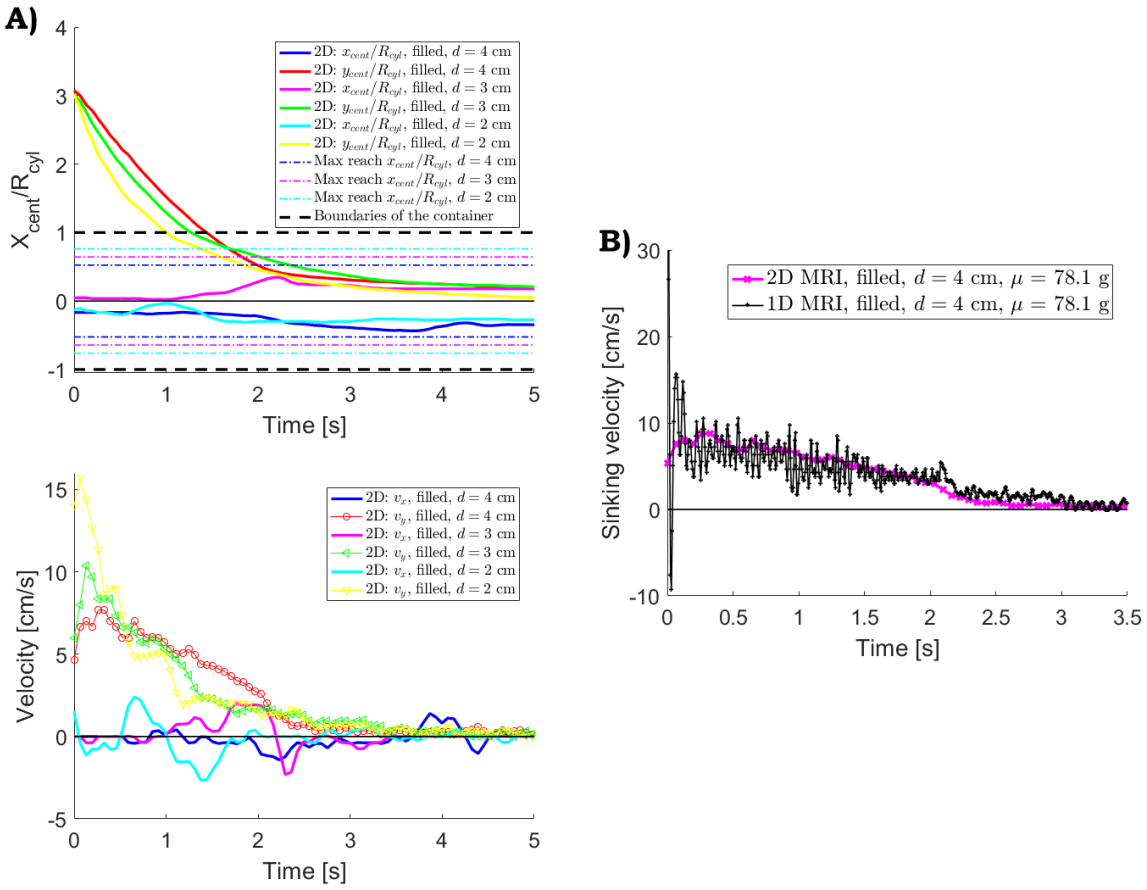

Figure 4.7: Filled ZrO_2 intruders' trajectories and velocity plots in a $\phi_s = 0.44$ cornstarch suspension obtained by 2D MRI measurements. **A)** *Time vs. intruder centroid trajectory non-dimensionalized by the radius of the cylinder ($X_{cent}/R_{cyl} = [x_{cent}; y_{cent}]/R_{cyl}$) and velocities for intruders of diameters $d = [2, 3, 4]$ cm and buoyancy-corrected masses $\mu = [6.7, 26.3, 78.1]$ g.* **B)** *Time vs. sinking velocity comparison between the 1D and 2D MRI signal for the large filled sphere under the same experimental conditions but different spatio-temporal resolution and different tracking methods.*

The experiments undertaken therefore were useful to check whether the motion in the transverse (x) direction is substantial and whether it plays a role in the trajectory of the intruder. In the top

part **A)** of the figure, horizontal and vertical trajectories of the centroid of the intruder are plotted against time as a dimensionless parameter which scales them with the radius of the cylinder. The limits shown in dashed lines are the maximum reachable points by the centroid of the intruder x_{cent} before the surface of the sphere reaches the wall.

In the region of initial impact there is hardly any motion, possibly meaning that the effects there are mostly due to compressive stress below the intruder and confinement of angled shear stresses from the lower left and right sides of the sphere. Yet at the core of the suspension a substantial movement is observed for all settling objects, noting the close proximity they reach to the walls especially pronounced in the large and medium intruders. What is more, a particular interesting trend can be pointed out from the velocity plots: before any (aliased) vertical velocity v_{y} oscillation, an oscillation in horizontal velocity v_{x} occurs as accompaniment of similar magnitude. This verifies the interpretation that the velocity oscillations are not due to pure compression below the suspension, but shear effects due to motion around the walls have a significant impact on the oscillatory behaviour for both v_{x} and v_{y} components of velocity. The effects of these movements may very well be the cause of the reluctance to see the single terminal velocity settling in all experiments of filled ZrO_2 spheres in a $\phi_{\text{s}} = 0.44$ cornstarch suspension. To check whether this is a universal phenomena, however, more information needs to be obtained from the experiments executed with the solid ZrO_2 intruders.

2D MRI: Solid intruders settling in a $\phi_{\text{s}} = 0.41$ suspension

The 2D MRI experiments that took place in May 2018 were performed for the two suspension packing fractions $\phi_{\text{s}} = 0.41$ and $\phi_{\text{s}} = 0.44$ with a similar temporal resolution for the solid ZrO_2 intruders as the one used in the filled ZrO_2 measurements - around 62.3 ms. As once again expected, the motion of the intruder signal is heavily aliased in the suspension of lower packing fraction, especially at the impact and bulk regions (see figure 4.8). For instance, the medium-sized intruder's centroid is first captured when it has sunk already about 30% of the suspension's depth ($y_{\text{cent}} \approx 2.7R_{\text{cyl}} \approx 70\%H_{\text{bed}}$, where $R_{\text{cyl}} = 4.2$ cm and $H_{\text{bed}} = 16.5$ cm). For this reason, only the behaviour of the large solid sphere of diameter $d = 4.28$ cm which was found to have the longest sinking time, was recognized as somewhat expected. Since the low packing fraction essentially provides the least resistance (low sinking times), it was predicted that less motion would occur in the $\hat{x}$-direction. This is indeed the case for the largest intruder, retaining its trajectory sideways to less than 5% of the radius of the cylinder, and indeed, in this measurement it is seen that a terminal velocity is kept constant. This is in agreement with the hypothesized reason for the different distinct terminal velocity regimes seen before in the spheres of largest diameter.

2D MRI: Solid intruders settling in a $\phi_s = 0.44$ suspension

The experiments performed with solid intruders settling in a suspension of $\phi_s = 0.44$ showed the most prominent results, depicting what was already predicted by von Kann *et al.*: less frequent and more pronounced oscillations at the bulk when keeping the same intruder size while shifting to a denser inner medium (filled plastic spheres of ZrO_2 at a random close packing of 64% of approximate density $\rho \approx 3200$ kg/m^3 to a fully-packed solid ceramic spheres of ZrO_2 of $\rho = 6000$ kg/m^3). These experiments were analyzed only for the balls of diameters $d = 4.28$ cm and $d = 3$ cm due to loss of experimental data.

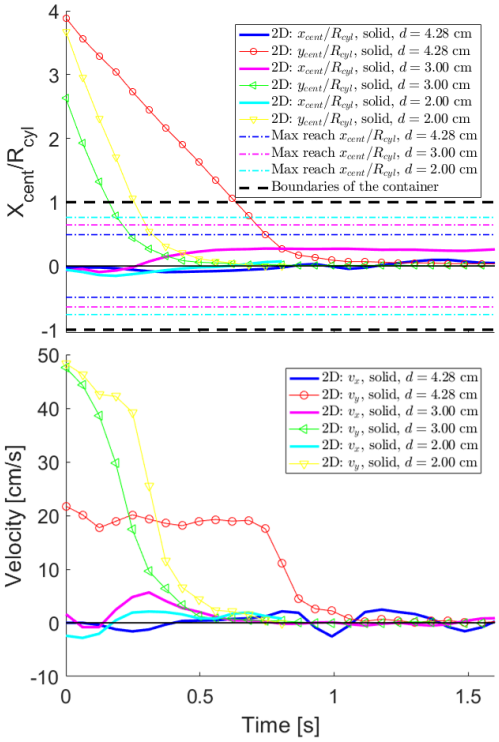

Figure 4.8: Solid ZrO_2 intruders' trajectories and velocity plots in a $\phi_s = 0.41$ cornstarch suspension obtained by 2D MRI measurements. Time vs. intruder centroid trajectory non-dimensionalized by the radius of the cylinder ($X_{cent}/R_{cyl} = [x_{cent}; y_{cent}]/R_{cyl}$) and velocity for spheres of diameters $d = [2, 3, 4]$ cm and buoyancy-corrected masses $\mu = [18.8, 63.6, 195]$ g.

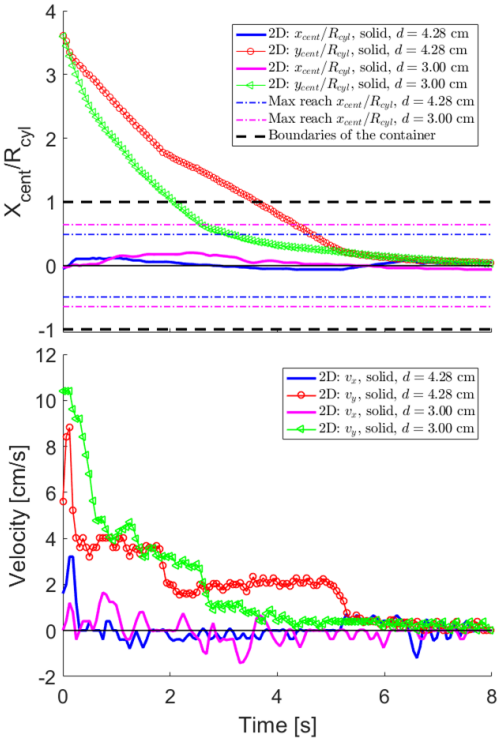

Figure 4.9: Solid ZrO_2 intruders' trajectories and velocity plots in a $\phi_s = 0.44$ cornstarch suspension obtained by 2D MRI measurements. Time vs. intruder centroid trajectory non-dimensionalized by the radius of the cylinder ($X_{cent}/R_{cyl} = [x_{cent}; y_{cent}]/R_{cyl}$) and velocity for spheres of diameters $d = [2, 3, 4]$ cm and buoyancy-corrected masses $\mu = [18.8, 63.6, 195]$ g.

In the experiments involving the large sphere, more clearly is shown than in any other that the bulk oscillations develop over two distinct stable oscillatory regions: necessarily, about 0.5 seconds after impact, any transient behaviour decays into oscillations around the bulk, a slow-down then

happens to put the intruder into another stable oscillatory region of lower amplitude and more frequent oscillations. This cannot be confused with the stop-and-go cycles because of the very large time duration over which it progresses. Specifically, approximately 3 seconds later (or 40% of the length of the sinking time) at a penetration depth of approximately 88% from the top surface, the intruder undergoes stop-and-go cycles which are aliased. Although seeing a clear movement of the heavy ball's centroid in the $\hat{x}$-direction to about 15% R_{cyl} just before the shift in oscillations, it is not merely sufficient to explain a decrease in terminal velocity of more than a double. It must be noted, however, that the motion in the $\hat{z}$-direction could not be observed via this MRI methodology, because, as explained previously the imaging takes placed over an averaged $\hat{z}$-direction 'plane' region. Further explanation on the phenomena observed from these particular experiments will be treated in sections 4.4 and 4.5.

4.2.3 Comparison of trajectories obtained from the different experiments

Comparisons were made between the various experimental results produced by different experimental methods in order to look qualitatively for trajectory behaviour explanations.

1D MRI and wire experiments in similar conditions

As explained earlier on, the wire experiments could only be completed for the plastic spheres filled with ZrO_2 granules. Keeping this restriction in mind and the fact that the 1D MRI experiments employing the intruders of diameters 2 cm and 3 cm yielded an unreadable signal, we are left with only one viable experiment for comparison purposes. Shown in figure 4.10, the experiment with the large $d = 4$ cm filled ball settling into a $\phi_{\text{s}} = 0.44$ cornstarch suspension is compared for the wire and 1D MRI measurements. It must be noted that the release height was significantly varied different for the two spheres. In spite of the suggestion by von Kann *et al.* that release height should not have a large influence on the overall settling behaviour in the bulk and beyond [2], it does have an effect on the after-impact transient oscillations for the reason that higher energy is dissipated by the system and consequently influences the overall sinking duration. Since it was already observed from the 2D trajectory experimental results that in all experiments the transverse motion is damped for the initial after-impact effects, there is no reason to expect any difference between the wire and 1D MRI data for the behaviour just after impact. Clearly, while the intruder dropped from a lower release height penetrates deep into the suspension, the other bounces off the depressed surface first before diving back into it. Furthermore, the re-acceleration velocity just after the first lower peak is steeper, just as discovered in part **B)** of figure 4.5 (examining the after-impact effects for the different intruder sizes), meaning that this phenomenon must be caused by transfer of

momentum between the suspension and the intruder's bottom. Having a network of particles acting back towards the intruder due to Newton's third law of motion would explain the object's increase in re-acceleration for the higher energy impacts.

In the rest of the domain, there are distinctive differences for the two experiments which cannot be explained in their full extent. Although it is hypothesized that lateral motion would have a positive impact on the frequency of bulk oscillations due to more disturbance pulses that can be felt by the intruder as it moves sideways in addition to its downward motion (by finding the lightest path through the suspension's interior), the difference is too high to form any conclusions based on these findings. What is more, since the 2D MRI experiment of figure 4.7 also verifies the substantially lower terminal velocity reached under the same conditions almost exactly, it must be recommended that the wire experiment is repeated.

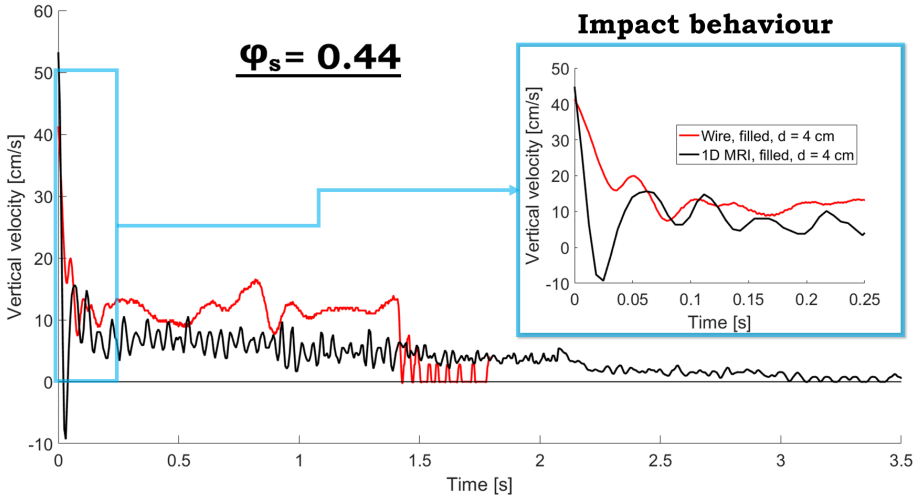

Figure 4.10: Large plastic sphere filled with ZrO_2 ($d = 4cm$) sinking in a cornstarch suspension of $\phi_s = 0.44$ with a bed fill height of 16.5 cm, released from free fall heights of 1 cm and 5.3 cm for the wire and 1D MRI experiments, respectively. Inset closes up on the curious impact behaviour for the two experiments.

Qualitative comparison of patterns observed for variable object size

Prior to this thesis work, the effect on the phenomena observed when an object settles into a cornstarch suspension were studied for variable suspension packing fractions, container sizes, object shapes and, finally, for variable object mass through increased object density. In this work, as suggested earlier on, the object's interior density was kept constant and therefore mass effects were studied by exploiting different intruder sizes, but keeping the same shape. This qualitative comparison was studied via the 1D MRI measurements only, because of the higher spatio-temporal resolution than the one exploited in the 2D MRI methodology.

The effects were split into four regions of phenomena: the full domain, the after-impact oscillations, the stable bulk oscillations and the stop-and-go cycles near the container bottom and summarized in table 4.1. Regarding the entire sinking process, a larger time duration is discovered when the mass is increased via increasing intruder size. This is an effect that is trusted to come from the direct observation that the stable oscillating bulk velocity decreases via increasing size. This is exactly the opposite to what happens when mass is increased via elevating the inner density of the object, and therefore it is concluded that the size boost on a spherical intruder has a negative forcing on terminal velocity. Strictly concerning the stable oscillations, no other evident differences were noticed: specifically, both amplitude and frequency around the terminal remained similar for the various sizes. Since they did, in fact, alter in von Kann *et al.*'s experiments, this leads to the verification of their observation that these oscillations are mainly driven by density differences [2]. In spite of sharing similar frequency in all experiments performed, the stop-and-go cycles phenomena near the bottom of the container exhibited a reduction in re-acceleration peak velocities to the contrary of the behavioural trends recognized in the wire experiments of different intruder densities. This nonlinear effect is interpreted as follows: via the proposed jamming model of von Kann *et al.* (found to work quite well in describing re-acceleration speeds for their experimental conditions), it was suggested that the term $\frac{\mu_{\text{intr}}}{m_{\text{intr}}}g$ is dominant relative to the drag force term $D = -B\dot{x}$ acting onto the intruder during the stop-and-go cycles (refer back to equation 1.7 for more details) and therefore the latter was neglected; however, in the experiments performed by the 1D MRI, the buoyancy ratio $\frac{\mu_{\text{intr}}}{m_{\text{intr}}}$ was kept constant to approximately 0.79g. Therefore, the decline in acceleration peak velocities must be coming from the difference in the drag term, whose absolute value is believed to increase for an increase in object's exposed surface area (scaling with $A_{\text{exp}} \sim r^2$ from classical mechanics. Decreasing the drag term (note that the term is negative by default) in the proposed model, in fact, slightly decreases the acceleration achieved and hence explains the re-acceleration peak values in the 1D MRI set of measurements. In the wire experiments of von Kann *et al.*, the effect is more negatively pronounced because of the positive forcing in the dominant buoyancy ratio term [2]. Even in their work, in spite of capturing quite well the very first stop cycle, they tend to overestimate the peak velocities and the frequency of the cycles, implying that the counteracting term of re-acceleration should not be universally neglected in the jamming model.

In the after-impact oscillations, similar tendencies are noted in all experiments: the first minimum velocity and the reactant re-acceleration speed are generally more pronounced with the elevation of impact energy, meaning that for higher amount of momentum is absorbed and the compressed particle matrix below the intruder grows into a jammed region faster and reacts back onto the

intruder. A new hypothesis for the entire physical mechanism causing these after-impact effects will follow in section 4.5 after obtaining a good view on how the interior of the suspension behaves.

Table 4.1: Qualitative comparison table of trends observed from the data in figures 1.12, 4.5 and 4.6: the von Kann *et al. wire experiment for variable intruder mass via varying the density inside a fixed-diameter spherical intruder* [24]*, the $\phi_s = 0.41$ 1D MRI experiment for variable intruder mass via varying its diameter with constant density, and the $\phi_s = 0.44$ 1D MRI experiment for variable intruder mass via varying its diameter with constant density, respectively. All experiments were performed in non-density-matched cornstarch suspensions.*

Phenomenon	**Wire, $\phi_s = 0.44$, $d = cst$: Increasing mass via density**	**1D MRI, $\phi_s = 0.41$, $\rho = cst$: Increasing mass via size**	**1D MRI, $\phi_s = 0.44$, $\rho = cst$: Increasing mass via size**
Full domain	Reduced sinking time T_{sink}	Increased sinking time T_{sink}	Increased sinking time T_{sink}
After-impact oscillations	No stop-go cycles observed Higher re-acceleration velocities on average More pronounced first minimum	Stop-go cycles: $d = 4.28$ cm Slightly higher re-acceleration velocities on average More pronounced first minimum	Stop-go cycles: $d = [3, 4.28]$ cm Slightly higher re-acceleration velocities on average More pronounced first minimum
Stable bulk oscillations	Increased amplitude of oscillations Increased terminal velocity Decreased frequency of oscillations	Similar amplitude of oscillations Decreased terminal velocity Similar frequency of oscillations	Similar amplitude of oscillations Decreased terminal velocity Similar frequency of oscillations
Stop-and-go cycles near bottom	Increased reacceleration peak velocities Similar stop-and-go cycles frequency	Decreased reacceleration peak velocities Similar stop-and-go cycles frequency	Decreased reacceleration peak velocities Similar stop-and-go cycles frequency

4.3 Suspension velocity and shear rate behaviour

The 2D velocity-encoded MRI methodology enabled probing in the interior of the suspension's to extract horizontal and vertical velocity images of the fluid in motion. As explained previously, this signal was generated by exciting the hydrogen protons in the water, so essentially, these images do not show the movement of the particles but illustrate the water's movement. As far as it is known, such high resolution images of sinking intruders in cornstarch suspensions have not yet been observed in the literature, mainly due to the obstacle of highly dynamic motion in the interior therefore requiring significant spatio-temporal resolution to be captured.

Figure 4.11 shows the suspension's velocity behaviour for four carefully picked time frames of the 2D MRI experiment exploiting a large $d = 4.28$ cm sphere intrusion into a well-mixed non-density matched cornstarch suspension of packing fraction $\phi_s = 0.44$. Particularly, spanning from left to right, quiver plots on top of the velocity magnitude are demonstrated for the first stable oscillatory region of lower frequency, the second stable oscillatory region of higher frequency, a region that can be considered as a full-stop within the uncertainty of the measurements, and lastly, a snapshot during a re-acceleration period scanned by the MRI.

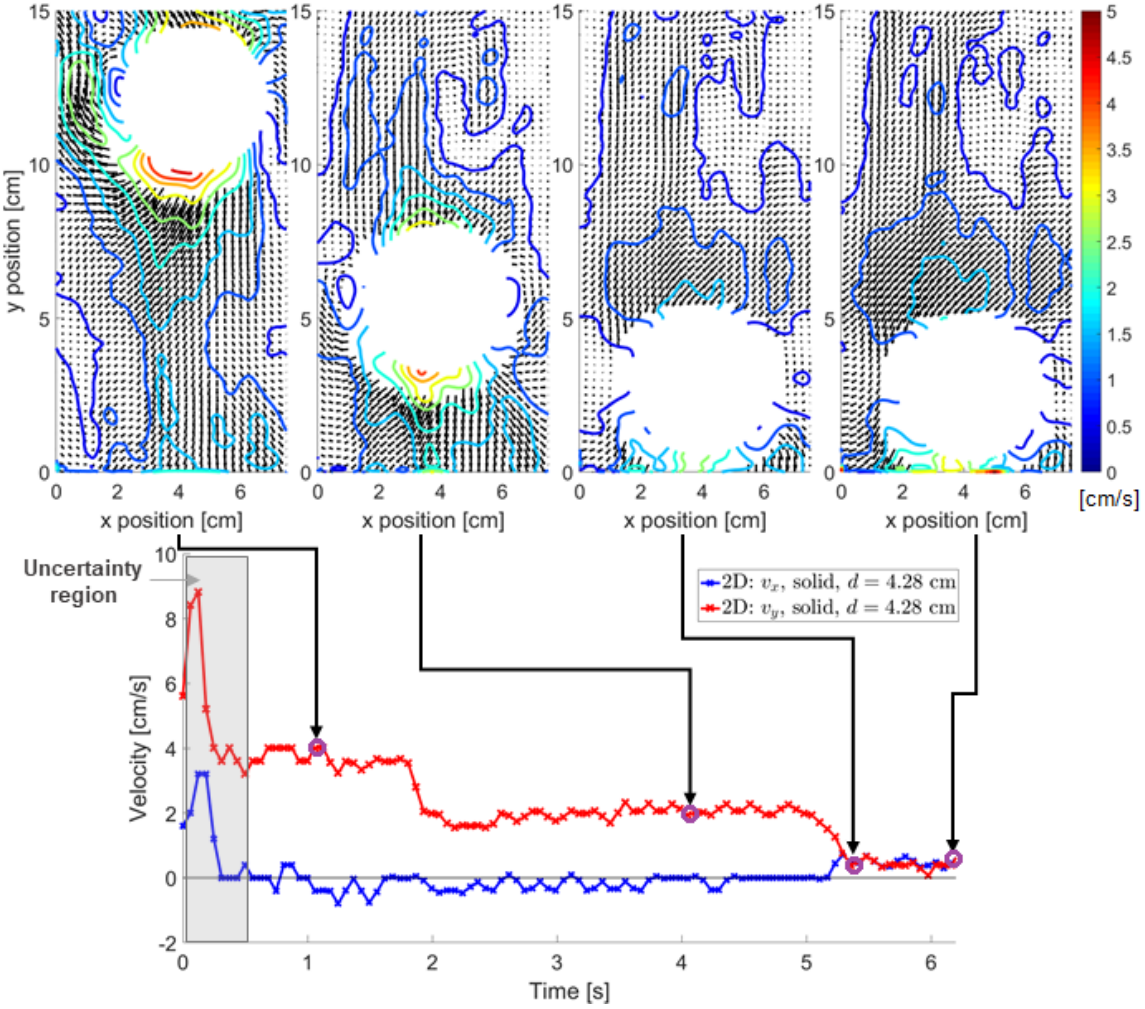

Figure 4.11: Velocity quivers of the suspension plotted on top of a velocity magnitude contour obtained via 2D velocity-encoded MRI measurements for the large solid ball of diameter $d = 4.28$ cm sinking into a $\phi_s = 0.44$ cornstarch suspension at four distinct time frames. As shown in the lower graph these time frames were carefully chosen to present the behaviour of the suspension at four regions of interest: specifically, during first stable bulk oscillations, second stable bulk oscillations, a full-stop and a re-acceleration period. Note in the graph below the 'uncertainty region' for which suspension details could not have been obtained.

In the first stable oscillatory regime, the suspension exhibits the highest velocities of these four time frames spanning through the domain (note that no meaningful observations can be made from the first 0.5 seconds of the experiment due to measurement artifacts between the sphere and the container wall). As indeed expected by potential flow for a sphere sinking in a Newtonian fluid, the object sinks due to gravity effects, pushes liquid on the bottom and as it compresses, liquid shifts sideways and then upward around the sphere; then it is being dragged towards the sphere top finding the nearest path while it is being constrained by the surface tension of the suspension's surface. A considerable anisotropy in contrast to potential flow theory is observed in the in this time frame, however: specifically, a preferred motion to the left hand-side, which could be triggered by

an undergoing rotation of the object. However, the MRI signal does not produce any information of object rotation. In fact, the effect of rotation was attempted to be tested with another set of 2D MRI measurements through the course of this work via placing a hollow rod (holding water within) in the plastic spheres filled with ZrO_2 granules. In these measurement sets the signal was also not strong enough to judge rotation of the sphere.

In the second stable oscillatory zone, the average velocities are lower and a more isotropic behaviour of the curls around the intruder are seen. This is also shown in the comparison of vertical and horizontal velocity curves at this point where hardly any lateral motion can be detected, to the contrary of what was seen in the first time frame where vertical sinking was additionally accompanied by a transverse velocity shift.

The last two figures present the spheres at penetration depths 95.5% and 96.6% from the suspension's surface, respectively. This is regardless of what is actually observed on the figure's quiver plots which were essentially undersampled to qualitatively see the trends. Moreover, the intruder mask having 'NaN' values in its interior compromised the nearest quiver arrows' direction. Furthermore, as explained previously in section 3.3.4, the mask was extended by 5 to 6 different pixels for all experiments to avoid the high velocity effects due to artifacts generated in the Zirconia interior. As predicted, close to the full-stop, the motion beneath the ball is significantly reduced before enough fluid can unjam the suspension's lower layer. In the last frame, the highly viscous-dominated lubrication layer has caused a large increase in the $v_{\mathrm{x,sus}}$ component.

The absolute values of the shear rate $\dot{\epsilon}_{xy}$ and compressive rate $\dot{\epsilon}_{xy}$ components of the strain rate tensor for axisymmetry

$$\dot{\epsilon} = \begin{bmatrix} \frac{\partial u}{\partial x} & 0 & \frac{1}{2}\left(\frac{\partial u}{\partial y} + \frac{\partial v}{\partial x}\right) \\ 0 & \frac{v}{y} & 0 \\ \frac{1}{2}\left(\frac{\partial u}{\partial y} + \frac{\partial v}{\partial x}\right) & 0 & \frac{\partial v}{\partial y} \end{bmatrix}$$

are calculated with a second-order central differencing scheme on the bicubically-interpolated data and illustrated in figure 4.12 for the same four time frames that velocity fields were discussed. One can clearly see longitudinal stripes of alternating high and low rates of strain which may be either due to after-impact transient oscillation effects due to unidirectionally shear-jammed fragile states, or due to MRI artifacts. To check this, the undisturbed suspension data was carefully observed, and it was shown that there are velocities present in this stripe manner that amount to less than 2% of the velocity-encoded parameter v_{enc}, therefore the discussion of this experiment will continue, but it will be kept in mind that possible overestimation of the shear rate values may take place due to a probable amplification from the stripes caused by MRI phase wrapping-around effects. In general,

shear rate is highly pronounced for the bottom and top side regions at an angle of approximately 45% measured radially from the sphere's lowest point. This is expected due to the high difference in velocity that forms between the liquid being pushed vertically and the surrounding liquid that goes around the object. It is expected though, to see compression effects in $\dot{e}_{yy}$ just below the sphere but instead they are seen at an angle too. Having these effects concentrated at this position is trusted to be the reason for transverse trajectory movement for this particular time frame and its adjacent ones.

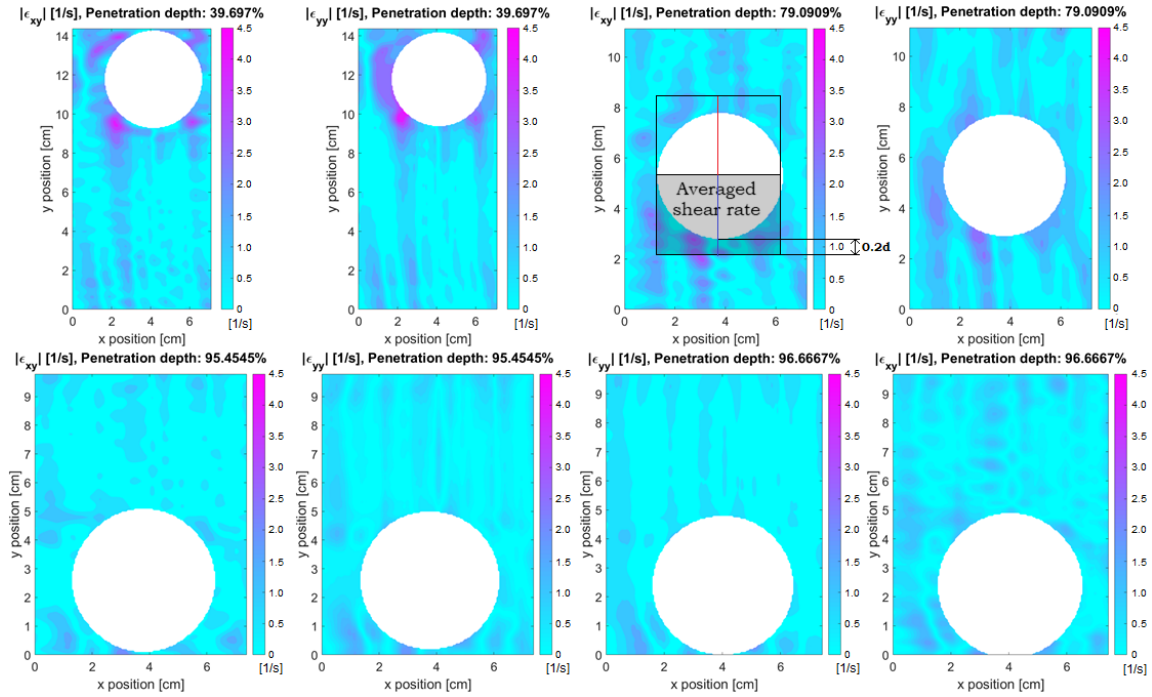

Figure 4.12: Contours of two components of the shear rate tensor $|\dot{\epsilon}_{xy}|$ and $|\dot{\epsilon}_{yy}|$ obtained via 2D velocity-encoded MRI measurements for the large ball of diameter $d = 4.28$ cm sinking into a $\phi_s = 0.44$ cornstarch suspension at four distinct time frames. The components are plotted two by two for the exact same four regions of interest as the velocity quivers. The rectangular box illustrates the region (extending 20% below the lower sphere bottom) at which shear rate was averaged.

Now that the reader is familiar with the observed patterns in velocity, shear and compression rate, we shift our attention to quantitative shear rate relations in the behaviour surrounding the intruder.

4.4 Shear relations in the suspension behaviour

As shown in the representative bounding rectangular box in figure 4.12, most of the analysis was performed for averaged quantity regions below and above the intruder, extending to a fixed limit of 20% the diameter of the individual intruder. This was performed for all 2D velocity-encoded experiments performed in the laboratory; however, because of the low temporal resolution

to capture the effects in the filled spheres and solid spheres at packing fraction ϕ_s, these will not be reported as very little information can be gained from them.

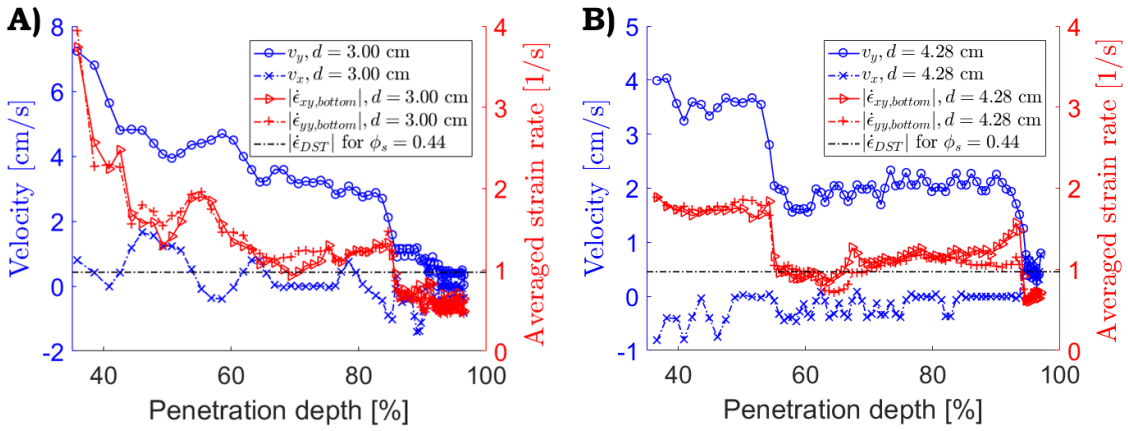

Figure 4.13: Penetration depth vs. averaged shear rate below the intruder for the 2D velocity-encoded MRI measurements of medium and large solid spheres of diameters **A)** *3 cm and* **B)** *4.28 cm, respectively, sinking into a $\phi_s = 0.44$ cornstarch suspension. The sphere's v_x and v_y components of velocity are plotted in the left blue axis in order to correlate suspension behaviour to different regimes of sphere motion. The right red axis, on the other hand, sets the limits for the compression and shear rate.in units of $[s^{-1}]$. The black dashed line is the critical DST shear rate obtained from the rheology data of* Madraki *et al.* [49].

The average shear and compression rates, as well as intruder velocity are demonstrated in figure 4.13 for the variance in penetration depth measured from $\frac{d}{H_{\text{sus}}} \cdot 100\%$ of the suspension fill height to 0% (meaning that the very bottom of the spheres is tracked). The results presented are those of the solid ZrO_2 medium and large intruders in a $\phi_s = 0.44$ cornstarch suspension by 2D velocity-encoded MRI. Clearly, we can follow that both the shear rate and compression rate behaviours closely match the trends seen in velocity. In essence, they also decrease until a minimum is reached during stop-and-go cycles near the container base, change abruptly at transition points between phenomenological regimes and fluctuate around a terminal value during stable sinking periods. But one peculiar observation is that before a sudden change in sinking velocity v_y, the anisotropic shear rate $\dot{\epsilon}_{xy}$ follows a slight decrease and then a steady increase towards a peak, which is significantly higher than that of the compression rate. This is an indication that, within the uncertainty of the measurements, jamming is caused by a combined effect of shear and compression stresses with a dominance of the former acting specifically at a certain angle below the intruder due to the suspension's inertial effects. The critical shear rate required for DST suggested by Madraki *et al.*'s rheology experiments for $\phi_s = 0.439$ density-matched suspension $|\dot{\epsilon}_{\text{DST}}| \approx 0.95\ s^{-1}$, is almost exclusively overcome throughout the initial penetration but is seen to stabilize around it during the stable bulk oscillations between 60 and 90% penetration depth for both experiments.

To gain more insight into the cause of the shear and compression rates' behaviour, the sinking velocity is plotted against it for both intruders in part **A)** of figure 4.14. Reading the plot from the top right (the first point in time), the rates of shear and compression decrease non-monotonically. To state it in a different manner, more than one value of strain rate in the bottom region corresponds to a given velocity (seeing these circular patterns where bulk oscillations take place). To make a qualitative comparison, the overall resistance force, which we will call drag force is calculated from the Newton's third law of motion for a settling sphere in a liquid

$$D(x, \dot{x}, t) = (m_{\text{intr}} + m_{\text{added}})\ddot{x} - \mu g \tag{4.2}$$

and is then plotted against sinking velocity too in part **B)**. Note that the added mass is calculated as $1/2\rho_{\text{sus}}\pi d_{\text{intr}}^3/6$ and the acceleration is estimated from the aliased signal frequency for the medium-sized sphere. Nevertheless, a qualitative comparison of the two plots demonstrates that the drag term, being similar in magnitude to the buoyancy term in the equation, can be slightly altered by compression and shear rate below to result in significant acceleration increase.

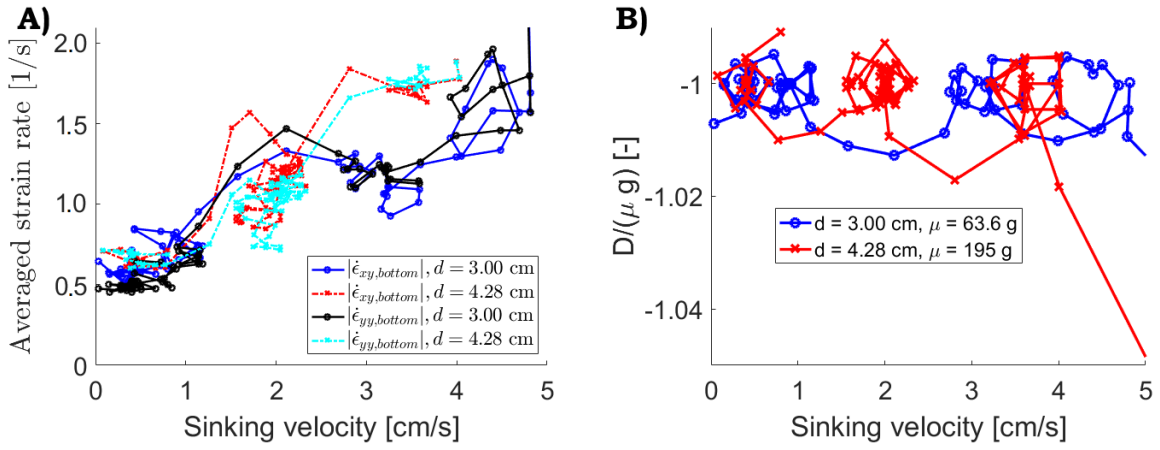

Figure 4.14: **A)** *Sinking velocity vs. averaged shear rate below the intruder for the 2D velocity-encoded MRI measurements of medium and large spheres of diameters $d = 3$ cm and $d = 4.28$ cm, respectively, sinking into a $\phi_s = 0.44$ cornstarch suspension.* **B)** *Sinking velocity vs. Drag normalized to buoyancy computed from Newton's second law of motion $D(x, \dot{x}, t) = (m_{intr} + m_{added})\ddot{x} - \mu g$*

We switch our attention now to figure 4.15 where the relative action of shear rates in the top left, top right, bottom left and bottom right are presented. It is a particularly important figure to illustrate the relative effects of the bottom and top region at the transition periods between phenomenological regimes. During stable sinking it is seen that the top and bottom rates of shear share similar magnitudes, implying that oscillations occur due to a competition between the suspension's stresses developed at an angle on the top and bottom of the intruder as a result of suspension

inertia. Furthermore, the data suggests that the oscillations occurs around the critical shear rate region for discontinuous shear thickening. This also possibly suggests that any added-up difference in shear rate due to local anisotropy in the top or bottom regions would cause a significant change in stress, slowing down or accelerating the sphere. In any case, this needs to be revisited by performing another set of MRI velocity-encoded measurements or high-speed ultrasound for higher temporal resolution imaging via applying a transducer on the bottom of the container.

Lastly, it is seen that at the transition between the two regions of stable oscillations, the abrupt rise in bottom shear rate is only accompanied by a slight elevation in rate of stress on the top region. This is predicted as the critical shear stress necessary for discontinuous shear thickening or shear jamming was expected to be dominant in the bottom layer because of the combination of shear and compression rates being higher as a result of gravity and the confinement of the walls. This is also the case for the first stop-cycle of the large intruder where the averaged top layer rate of shear is approximately kept at a constant value.

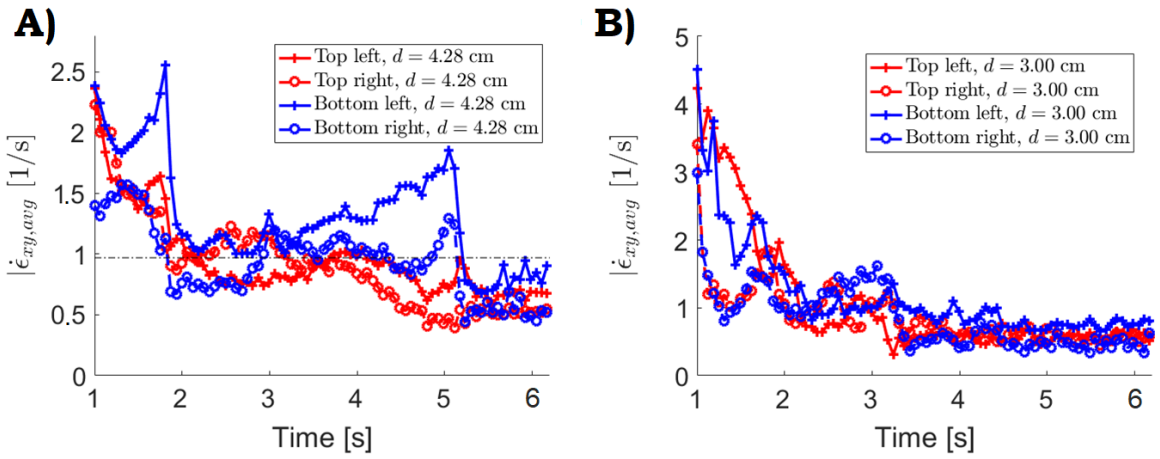

Figure 4.15: Time vs. averaged shear rate in all regions around the intruder extending to 20% of its diameter for the **A)** *medium-sized ($d = 3$ cm) solid sphere and* **B)** *the largest solid sphere ($d = 4.28$ cm).*

Having analysed the patterns in velocity, shear rate and compression rate behaviours, it is possible to make a physical interpretation of the mechanism that drives the newly-observed after-impact transient phenomena.

4.5 Proposed physical mechanism for the after-impact effects

In order to interpret the mechanism causing the after-impact transient oscillations of the intruder's motion up to a point that repetitive damped stop-and-go cycles are observed (see figure 4.16), first a summary will be made for the dependence of these behaviours on different variable pa-

rameters obtained from the experiments performed in this work, and if these do not provide enough information it will be looked for reference published work.

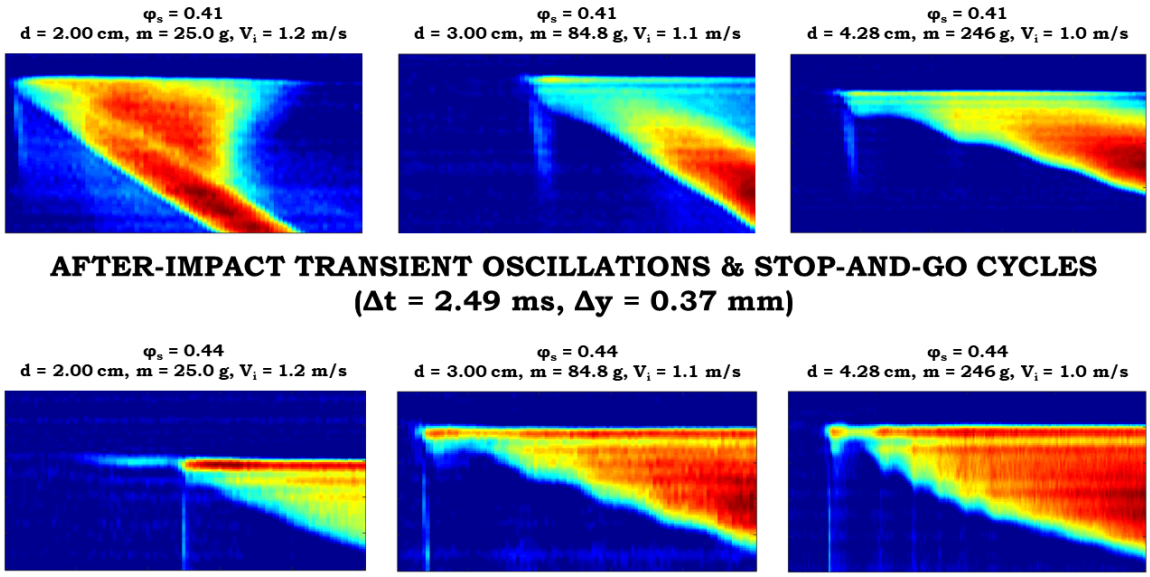

Figure 4.16: 1D MRI images of the transient oscillations and stop-and-go cycles occurring just after impact. Note that the images are not to scale, but used to optically observe the behaviour.

The dependencies are discussed in bullet points below.

- **Dependence on intruder mass via varying size at constant density:** Upon increasing mass by increasing the diameter of the spherical intruders (keeping the buoyancy ratio μ/m constant), an increase in amplitude follows for approximately similar impact velocities.
- **Dependence on free fall height:** The comparison between wire and 1D MRI experiments for different falling height uncovered the positive forcing on initial amplitude by the free fall height for the large ($d = 4$ cm) plastic sphere filled with ZrO_2 granules (see figure 4.10). The oscillations quickly decay into their stable mode.
- **Dependence on packing fraction:** As illustrated by figure 4.16, larger packing fraction yields more pronounced transient oscillations, meaning that more frequent and higher amplitude oscillations or stop-and-go cycles take place.
- **Dependence on container width:** In an experiment performed by von Kann *et al.* of the exact same falling steel ball ($d = 1.6$ cm) under the same impact velocity, they found that significantly lower initial slow-down velocity is observed for an intruder sinking in a cylinder of diameter $d = 5$ cm than in a rectangular container of size [12;12] cm, both of equal bed fill heights (see the behaviour in the cylinder in part **B)** of figure 1.13) [2].
- **Dependence on suspension height:** In an experiment of an accelerated rod into a suspension bed for different depth heights, Waitukaitis and Jaeger find that the primary peak

response is not a signature of depth, therefore lower boundaries do not play a role in its behaviour [9]. However, they find that a secondary oscillation in acceleration occurs sooner and higher in magnitude in lower bed fill heights which they strongly-correlate with force transmitted to the container base via a force actuator positioned there. They finally conclude that the primary response is not the result of stress transmission to the lower boundary but once solidification has reached the bottom, forces propagate with no detectable delay back towards the intruder [9].

- **Dependence on penetration depth:** In the 1D MRI experiments executed in this thesis work, it was shown that strong transient oscillations and stop-and-go cycles occur for all experiments only at penetration depths at which the intruder has not sunk completely into the suspension. The transition to stable bulk oscillation occurs once it is fully immersed.

The dependencies on mass, impact velocity and suspension height imply a phenomenon predicted by classical mechanics and the insights proposed by Waitukaitis and Jaeger [9] and Liu *et al.* [50]: for impact of faster and heavier objects, more energy is transmitted and dissipated by the system and dynamic jamming in the suspension is more prominent to occur. This is especially due to the direct observation of Waitukaitis and Jaeger demonstrating that the main cause of the large normal stresses generated, strictly concerning the very first impact peak, is the momentum transferred as the rapidly growing jammed solid (moving at a velocity of $v_{\text{front}} \approx k \cdot v_{\text{rod}}$) is pushed through the surrounding suspension by the impactor [9]. The dependence on container width suggests that confinement effects (by the side walls) due to suspension inertia may play an important role in the mechanism causing the pronounced transient oscillations or stop-and-go motion. Finally, the dependence on penetration depth, suggests that geometry and surface depression (due to conservation of mass in the globally incompressible $\nabla \cdot \boldsymbol{v} \approx 0$ suspension) may be the reason for the characteristics of the stresses exerted to and from the intruder. Now, having summarized the details of this complex phenomenon involving multiple effects from various sources, a physical interpretation of the mechanism causing this is suggested.

Upon touchdown of the intruder into the suspension compressive stresses beyond the critical act below it as momentum is transferred. This causes a dynamically jammed solid to propagate towards the lower boundary as the motion of the intruder stops or bounces off (note that the jammed front, moving at a linear speed of more than an order of magnitude greater than that of the intruder, does not need to have reached the boundary in order to stop the ball's motion, as explained by Waitukaitis and Jaeger [9]). Almost instantaneously after impact, while solidification has developed in one direction, due to conservation of mass system-wide, surface depression arises

due to elevated flow field sideways (this is also shown by a supplementary video in Waitukaitis and Jaeger's publication in [9]) and an added mass region below the intruder has extended in a cone-shaped region towards the side walls. A hypothesis follows that with the proximity of walls, if the development of the added mass region (due to conservation of mass) reaches the walls, jamming due to shear by the side of the ball can occur by allowing a much larger force chain to be transmitted from the boundaries. This hypothesis would explain why von Kann *et al.* did not observe the initial slow-down in the large container: their experiment was performed in a cornstarch suspension of packing fraction of $\phi_s = 0.42$, meaning that compressive stress alone from the 17 g steel ball of diameter $d = 1.6$ cm would not have been able to jam the suspension. As a result of this combined effect, the jammed region below the intruder relaxes through particle rearrangements (Darcy's flow in porous media) due to it being slowly compressed by the already stopped ball (or relaxed because of the air time of a bounce). The ball re-accelerates and sinks a bit deeper in the suspension (but not yet with its full size), compressive stresses build up once again causing suspension following a path by the container's sides again, high shear rate re-develops a little bit higher than before in the angled regions around the ball. This is shown in part **C)** of figure 4.17 by the yellow arrows. The cycle is repeated more times for the heavier and larger in size balls because of the larger momentum transfer and geometry constraints.

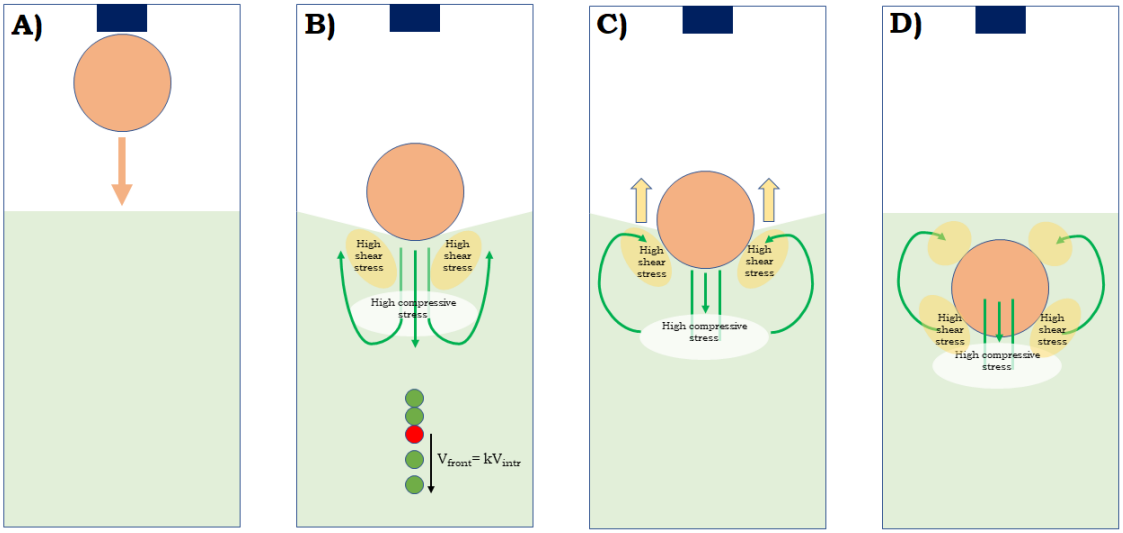

Figure 4.17: Schematic illustration of the proposed physical explanation for stop-and-go cycles just after impact. The intruder undergoes **A)** *free fall before* **B)** *it impacts, exerts a unidirectional compressive stress on the suspension below it and due to global conservation of mass causes flow in the upward direction, therefore constraining the surface to depress.* **C)** *During the propagation of the front the suspension's inertia sustains the jammed region by exerting shear stress on the sides of the intruder. The region of concentrated shear stress rises upwards as a cycle repeats and the intruder goes further down.* **D)** *Velocity pattern and stresses acting when the intruder has penetrated with its full size in the interior of the suspension.*

Finally, part **D)** of figure 4.17 explains why this is no longer observed when the ball has fully immersed in the stable oscillations region: shear stresses develop on top of it as well due to the surface tension leading to a transition from stop-and-go cycles to unstable oscillations and eventually to stable oscillations at the point in time that the sphere has sunk deep enough in order to allow for the fluid to be dragged along with it. The changes in velocity during the stable oscillations regime may very well be caused by a competition of these shear rates on the top and bottom where local anisotropies shift the viscosity from a shear-thinning to shear-thickening regime (see figure 4.1) and vice versa.

5 Conclusions & Recommendations

Novel experiments of wire, 1D and 2D Magnetic Resonance Imaging were undertaken through the course of the thesis in order to expand our knowledge concerning the sinking behaviour of spheres in a concentrated suspension of cornstarch and water. In the beginning, several objectives were set for this thesis. In particular, those were:

- to check whether undisturbed motion plays a role in any of the phenomena related to sinking of spheres in cornstarch suspensions;
- to determine the behavioural regimes of the suspensions during stable velocity oscillations and stop-and-go cycles near the container base;
- to provide evidence in order to answer the question whether boundaries govern the act of sinking in any of its regimes;
- to observe the sphere's behaviour just after impact.

To any reader it should have quickly become obvious that such complex state of the art measurement systems in combination with extremely complex behaviour of concentrated suspensions may yield uncertainties and measurement flaws that need to be dealt with. Overall, some issues were tackled in the most suitable and convenient manner to detect and observe new-found phenomena, peculiar trends in behaviour and to gain new insights of the physics governing these, while the rest remain a subject of future work.

First of all, wire experiments were performed for filled ZrO_2 spheres as means of reference in order to provide relevant time scales needed for MRI measurements and to provide comparison if the same conditions are met. The former was successfully achieved by obtaining two desired suspension packing fractions of $\phi_s = 0.41$ and $\phi_s = 0.44$ in order to capture dynamic motion at all regimes via 1D MRI and a slower response that is still meaningful for the smaller spatio-temporal resolution of 2D MRI scanning. When comparing the wire experiments within one another and with the 1D MRI results, several issues were pointed out:

- Friction occurred along the intersection of the rod and the wire due to dried cornstarch during the setup. To tackle this issue, the rod was extended in diameter and additional lubrication oil was applied prior to experiments.
- Wobbling of the wire sliding through the rod of higher diameter may have compromised the accuracy of the intruder's trajectory.
- The hand-picked wire release made it difficult to keep the same free fall height for all intruders, concluding that most wire experiments could not be compared to the MRI.

It is therefore recommended that the wire experimental setup is modified to avoid hand-picked release, but also to ensure that the sphere is being dropped in the center region of the cylinder.

2D MRI experiments have shown that the motion in the horizontal direction is not to be neglected for a sinking sphere in a cornstarch suspension of large packing fraction because this motion grows considerably within the bulk, especially during stable oscillations, and the stop-and-go cycles near the container base. It was directly observed that horizontal motion hardly appears in after-impact transient oscillations, possibly implying the role of stress confinement in all directions around the intruder. However, this was not the case for the largest solid intruder at the densest suspension, thus it is recommended to perform additional sets of measurements to test and verify this to a certain degree of confidence. In the rest of the domain it was demonstrated that anisotropic shear rate of the similar magnitude as the compression rate drives the horizontal trajectory change of the intruder. And finally regarding this transverse motion, direct evidence was provided that both vertical and horizontal velocity, although experiencing aliasing issues in most experiments due to poor temporal resolution of 2D MRI, share similar amplitude and frequency of oscillations.

In a novel comparison of behavioural trends in objects settling in cornstarch suspension for increasing mass via increasing the intruder's size (but keeping the same buoyancy ratio ratio μ/m), it was concluded that sinking time is in general increased due to a prominent decline in terminal velocity, the re-acceleration peak velocities during stop-and-go cycles were elevated with an increase in diameter. These effects were found exactly the opposite to what happens when mass is elevated via an increase in the object's interior density. From this observation, it was concluded that size boost on a spherical intruder has a negative forcing on terminal velocity, meaning that proximity of side wall boundaries must play a significant role in bulk oscillations. Regarding the stop-and-go cycles' re-acceleration peaks, it was found that small differences in the drag term of equation 4.2 cause significant effects on re-acceleration times, and therefore it shall not be universally neglected in the jamming model proposed by von Kann *et al.* [2].

Direct evidence was provided that upon increasing the packing fraction, free fall height and mass via size, stop-and-go cycles appear in the top region of the suspension as well. It was found that these effects are an extreme case of transient decaying oscillations and therefore are not always observed. For higher sizes and same density of the intruders, the first minimum was more pronounced and slightly higher re-acceleration velocities were achieved on average. For higher impact velocities this was also observed, concluding that mass and velocity, or momentum, are all positive influences of the pronounced behaviour just after-impact as predicted by classical mechanics. An own physical interpretation of the entire behavioural mechanism of this peculiar phenomenon was proposed in

section 4.5. It is recommended that more 1D and 2D MRI data of less than 10 ms temporal resolution is obtained to test the hypothesized physical mechanism for these effects in order to derive a jamming model for the re-acceleration peak velocity magnitudes scaled with the impact velocity, and their occurrence in time after impact.

Two regions of stable oscillations were found to develop in all experiments of spheres beyond 4 cm diameter (both filled and solid ZrO_2) in the suspension of the highest tested packing fraction. This was not previously reported in any of the available literature. The secondary oscillation region was found to exhibit more frequent oscillations and lower amplitudes. It was seen to appear in all types of experimental methodologies performed, although this effect was most evident in the solid sphere.

Lastly, The 2D MRI velocity data of the solid spheres settling into a $\phi_s = 0.44$ suspension of cornstarch and aqueous solution of water and negligible amount of contrast agent was found to exhibit MRI artifacts in the form of longitudinal stripes, causing a probable positive bias in both shear and compression rates. Nevertheless, the general behavioural trends in those rates were observed and it was found that via comparing them to the rheology results obtained by Madraki *et al.*, they maintain a value beyond the critical for discontinuous shear thickening in the initial stable oscillations, while in the secondary region of oscillations they happen around the magnitude of this critical shear rate. It is strongly recommended that own rheology experiments are performed to verify this. Indeed, this was initially planned but could not be executed due to lack of necessary rheology equipment in the laboratory.

Concerning the overall tendency of the averaged rates of compression and shear around the intruder, evidence was provided that the top and the bottom areas around the intruder undergo similar rates of stress during the stable bulk oscillations but differ substantially at transition moments between regimes. Precisely, the rates of stress in the bottom layer increase steadily to 100-200% of those on the top region until a point of an abrupt decline when the transition to a full stop takes place. In any case, another experiment session needs to be scheduled to confirm these observations after appropriately tackling the longitudinal stripes issue.

Lastly on the topic of 2D MRI velocity-encoded measurements, before concluding this thesis work, it is suggested that another set of MRI measurements is performed for a highly viscous Newtonian fluid with similar sinking time duration as the 2D velocity-encoded MRI data of large solid spheres in the densest suspension tested. The main function of these measurements would be to acquire reference shear and compression rate data (whose exact solution we know already) using the

velocity-encoded 2D MRI methodology before performing all other hypothesis-verification-related cornstarch experiments.

Appendices

A Pulse sequences

The Magnetic Resonance Imaging pulse sequences of the experiments are attached in this Appendix. First, the rapid 1D EPI pulse sequence is shown in section A.1. Section A.2 then displays the pulse sequence used for single-shot velocity-encoded 2D EPI.

A.1 Rapid 1D EPI pulse sequence

The pulse sequence used for Rapid 1D EPI measurements can be found in figure A.1.

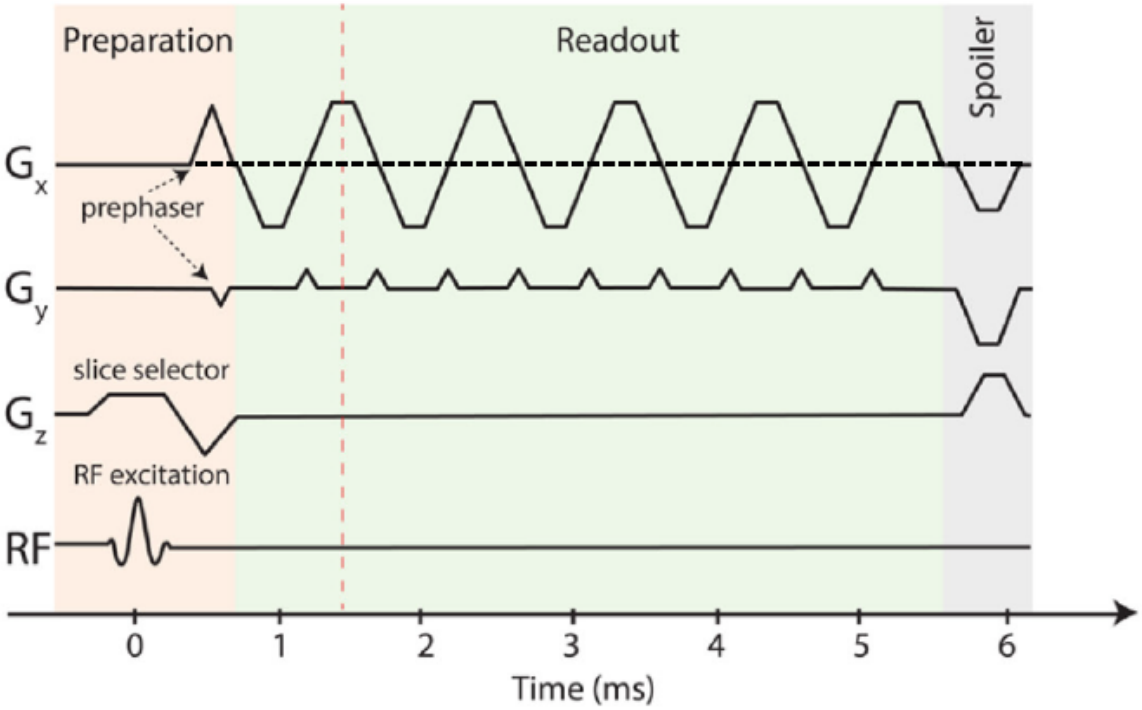

Figure A.1: Single-shot echo-planar imaging (EPI) pulse sequence without prephaser gradient G_x used for rapid 1D intensity measurements. It is divided into i) a preparation stage (red shaded areas), where the spins are excited and their phase is modulated to produce the desired contrast, ii) a readout stage in which data is acquired (green shaded areas) and iii) the spoiler phase, where remaining spin coherences are dephased (gray shaded areas). The dashed vertical lines demarcate the center of k-space. Adapted from Penn [34]. *Copyright 2018 ETH Zürich.*

A.2 Velocity-encoded 2D EPI pulse sequence

The pulse sequence used for 2D velocity-encoded EPI measurements can be found in figure A.2.

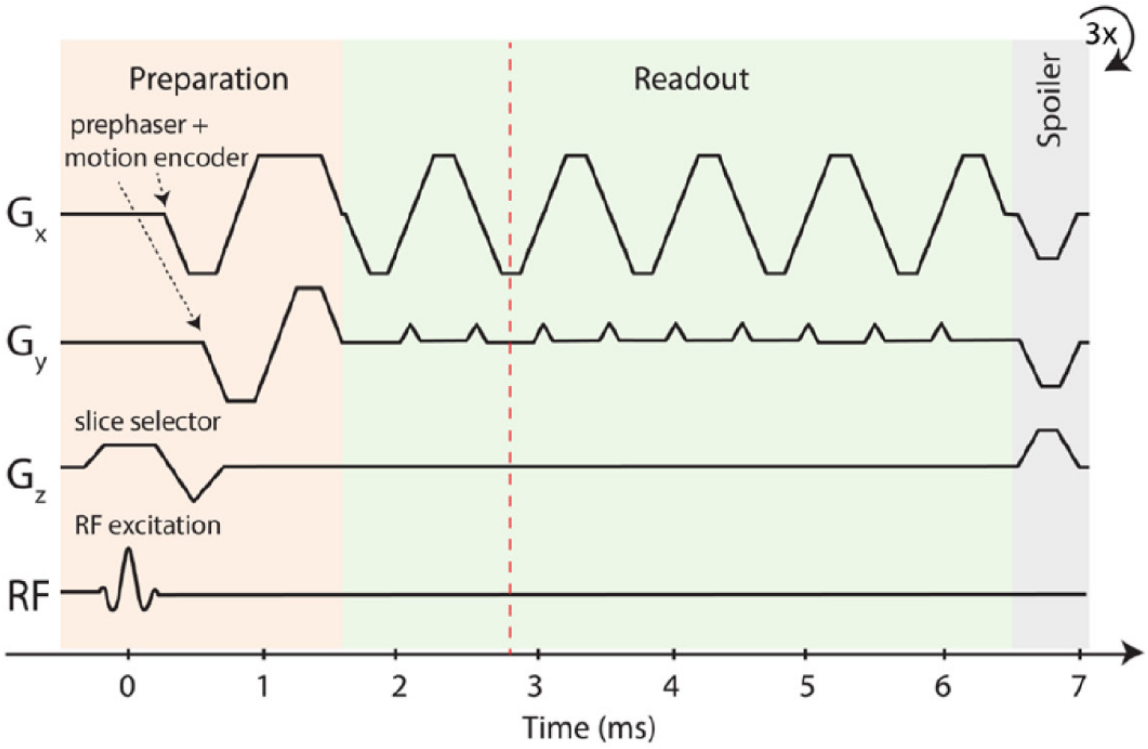

Figure A.2: Single-shot EPI phase contrast velocimetry pulse sequence used to determine both spin density and fluid velocity in the system. It is divided into i) a preparation stage (red shaded areas), where the spins are excited and their phase is modulated to produce the desired contrast and a bipolar motion encoding gradient is used, ii) a readout stage in which data is acquired (green shaded areas) and iii) the spoiler phase, where remaining spin coherences are dephased (gray shaded areas). The sequence is repeated three times in which the prephaser gradients G_x are switched on alternately to produce velocity information in x and y directions. The dashed vertical lines demarcate the center of k-space. Adapted from Penn [34]. *Copyright 2018 ETH Zürich.*

B Signal processing filters

B.1 Signal processing of wire experiments

The undersampling factors and Savitzky-Golay filter specification values used for the wire experiments are presented in table B.1.

Table B.1: Table of filter specification values used for the wire experiments. In the table 'SG' stands for the Savitzky-Golay filter. The specification values for the filter a provided as undersampling factor 'US', polynomial 'order' and moving 'window' frame length.

Experiment data	**S-G: trajectory**	**S-G: velocity**
$\phi_s = 0.41$; Filled ZrO_2, $d = 2$ cm.	Order: 1 Window: 21	Order: 2 Window: 9 US: 2
$\phi_s = 0.41$; Filled ZrO_2, $d = 3$ cm.	Order: 1 Window: 21	Order: 2 Window: 11 US: 2
$\phi_s = 0.41$; Filled ZrO_2, $d = 4$ cm.	Order: 1 Window: 21	Order: 2 Window: 11 US: 3
$\phi_s = 0.44$; Filled ZrO_2, $d = 2$ cm.	Order: 1 Window: 25	Order: 2 Window: 9 US: 2
$\phi_s = 0.44$; Filled ZrO_2, $d = 3$ cm.	Order: 1 Window: 25	Order: 2 Window: 7 US: 2
$\phi_s = 0.44$; Filled ZrO_2, $d = 4$ cm.	Order: 1 Window: 21	Order: 1 Window: 3 US: 2

B.2 Signal processing of MRI experiments

The detection methods, undersampling factors and Savitzky-Golay filter specification values used for the 1D MRI experiments are presented in table B.2. No filters were applied for the estimation of the 2D trajectory, velocity and acceleration data.

Table B.2: Table of detection methods and filter specification values used for the 1D MRI experiments. 'SG' stands for the Savitzky-Golay filter. The specification values for the filter a provided as undersampling factor 'US', polynomial 'order' and moving 'window' frame length. The tracking methods were two: Gaussian filtering and normalized cross-correlation algorithm (NormXCorr), applied to either the edge of the signal or for estimating its median. The median estimation was achieved via two methods: (1) and (2), and are extensively described in section 3.2 and figure 3.4.

Experiment data	**Tracking method**	**S-G: trajectory**	**S-G: velocity**
$\phi_s = 0.44$; Filled ZrO_2, $d = 2$ cm.	N/A	N/A	N/A
$\phi_s = 0.44$; Filled ZrO_2, $d = 3$ cm.	N/A	N/A	N/A
$\phi_s = 0.44$; Filled ZrO_2, $d = 4$ cm.	I: Gaussian edge; II: Gaussian median, (1)	Order: 1 Window: 5	Order: 0 Window: 1 US: 1
$\phi_s = 0.41$; Solid ZrO_2, $d = 2$ cm.	I: NormXCorr edge; II: Gaussian median, (2)	Order: 1 Window: 3	Order: 2 Window: 5 US: 1
$\phi_s = 0.41$; Solid ZrO_2, $d = 3$ cm.	I: NormXCorr edge; II: Gaussian median, (2)	Order: 1 Window: 3	Order: 1 Window: 3 US: 1
$\phi_s = 0.41$; Solid ZrO_2, $d = 4.28$ cm.	I: NormXCorr edge; II: Gaussian median, (2)	Order: 1 Window: 3	Order: 0 Window: 1 US: 1
$\phi_s = 0.44$; Solid ZrO_2, $d = 2$ cm.	I: NormXCorr edge; II: Gaussian median, (2)	Order: 1 Window: 3	Order: 0 Window: 1 US: 1
$\phi_s = 0.44$; Solid ZrO_2, $d = 3$ cm.	I: NormXCorr edge; II: Gaussian median, (2)	Order: 2 Window: 5	Order: 0 Window: 1 US: 1
$\phi_s = 0.44$; Solid ZrO_2, $d = 4.28$ cm.	I: NormXCorr edge; II: Gaussian median, (2)	Order: 1 Window: 5	Order: 2 Window: 5 US: 1

Bibliography

[1] N. J. Wagner and J. F. Brady. Shear thickening in colloidal dispersions. *Physics Today Vol. 62 Issue 10, 27-32*, 2009.

[2] S. von Kann, J. H. Snoeijer, and D. van der Meer. Velocity oscillations and stop-go cycles: The trajectory of an object settling in a cornstarch suspension. *Physical Review E, Vol. 87, 042301*, 2013.

[3] S. R. Waitukaitis. *Impact-Activated Solidification of Cornstarch and Water Suspensions*. University of Chicago, 2013.

[4] F. S. da Luza, E. P. Lima Juniora, L. H. Leme Louroa, and S. N. Manteiro. Ballistic test of multilayered armor with intermediate epoxy composite reinforced with jute fabric. *Materials Research. 2015; 18(Suppl 2)*, 2015.

[5] Y. S. Lee, E. D. Wetzel, and N. J. Wagner. The ballistic impact characteristics of kevlar woven fabrics impregnated with a colloidal shear thickening fluid. *Journal of Materials Science Vol. 38 2825-2833*, 2003.

[6] C. A. Garcia-Franco and R. M. Christensen. Non-newtonian behavior of suspensions. *Acta Mechanica 37, 85-97*, 1980.

[7] E. Brown, N. A. Forman, C. S. Orellana, H. Zhang, B. W. Maynor, D. E. Betts, J. M. DeSimone, and H. M. Jaeger. Generality of shear thickening in dense suspensions. *Nature Materials Vol. 9, 220-224*, 2010.

[8] A. Fall, N. Huang, F. Bertrand, G. Ovarlez, and D. Bonn. Shear thickening of cornstarch suspensions as a reentrant jamming transition. *Physical Review Letters 100, 018301*, 2008.

[9] S. R. Waitukaitis and H. M. Jaeger. Impact-activated solidification of dense suspensions via dynamic jamming fronts. *Nature. Vol. 487*, 2012.

[10] A. Fall, A. Lemaitre, and G. Ovarlez. Discontinuous shear thickening in cornstarch suspensions. *Physical Review Letters 100, 018301*, 2008.

[11] A. J. Liu and S. R. Nagel. The jamming transition and the marginally jammed solid. *Annual Review of Condensed Matter Physics*, 2010.

[12] B. Chakraborty and R. P. Behringer. *Jamming of Granular Matter*. Springer Encyclopedia of Complexity and System Science. Ed. Robert A. Meyers. Springer-Verlag. 4997-5021, 2009.

[13] A. J. Liu and S. R. Nagel. Nonlinear dynamics: Jamming is not just cool any more. *Nature. Vol. 396*, 1998.

[14] C. S. O'Hern, L. E. Silbert, A. J. Liu, and S. R. Nagel. Jamming at zero temperature and zero applied stress: The epitome of disorder. *Physical Review E. 68, 011306*, 2003.

[15] D. Bi, J. Zhang, B. Chakraborty, and R. P. Behringer. Jamming by shear. *Nature. Vol. 480*, 2011.

[16] R. L. Hoffman. Explanations for the cause of shear thickening in concentrated colloidal suspensions. *Journal of Rheology 42(1)*, 1998.

[17] L. M. Hocking. The effect of slip on the motion of a sphere close to a wall and of two adjacent spheres. *Journal of Engineering Mathematics, Vol. 7, No. 3*, 1973.

[18] R. Seto, R. Mari, J. F. Morris, and M. M. Denn. Discontinuous shear thickening of frictional hard-sphere suspensions. *arXiv:1306.5985v2* ***[cond-mat.soft]*** *URL: http://arxiv.org/abs/1306.5985v2*, 2013.

[19] E. Brown and H. M. Jaeger. Shear thickening in concentrated suspensions: phenomenology, mechanisms and relations to jamming. *Reports on Progress in Physics 77*, 2014.

[20] J. Bender and N. J. Wagner. Reversible shear thickening in monodisperse and bidisperse colloidal dispersions. *Journal of Rheology 40, 899*, 1996.

[21] H. M. Jaeger and S. R. Nagel. Granular solids, liquids, and gases. *Reviews of Modern Physics, Vol. 68, No. 4*, 1996.

[22] E. Brown and H. M. Jaeger. The role of dilation and confining stresses in shear thickening of dense suspensions. *Journal of Rheology 56, 875-923*, 2012.

[23] I. R. Peters, S. Majumdar, and H. M. Jaeger. Direct observation of dynamic shear jamming in dense suspensions. *Nature Vol. 532*, 2016.

[24] S. von Kann, J. H. Snoeijer, D. Lohse, and D. van der Meer. Nonmonotonic settling of a sphere in a cornstarch suspension. *Physical Review E Vol. 84, 060401*, 2011.

[25] P. N. Rowe, B. A. Patridge, E. Lyall, and G. M. Ardran. Bubbles in fluidized beds. *Nature Vol. 195, 278-279*, 1962.

[26] R. D. Wildman, J. M. Huntley, J. P. Hansen, D. J. Parker, and D. A. Allen. Single-particle motion in three-dimensional vibrofluidized granular beds. *Physical Review E Vol. 62, 3826-3835*, 2000.

[27] E. Han, I. R. Peters, and H. M. Jaeger. High-speed ultrasound imaging in dense suspensions reveals impact-activated solidification due to dynamic shear jamming. *Nature Communications Vol. 7:12243*, 2015.

[28] E. E. Ehrichs, H. M. Jaeger, G. S. Karczmar, J. B. Knight, V. Y. Kuperman, and S. R. Nagel. Granular convection observed by magnetic resonance imaging. *Science Vol. 267*, 1995.

[29] A. Penn, T. Tsuji, D. O. Brunner, C. M. Boyce, K. P. Pruessmann, and C. R. Mueller. Real-time probing of granular dynamics with magnetic resonance. *Science Advances Vol. 3*, 2017.

[30] D. W. McRobbie, E. A. Moore, M. J. Graves, and M. R. Prince. *MRI From Picture to Proton.* Cambridge University Press, 2006.

[31] Infiniti Research Limited. Global mri systems market report 2017-2021. *Global Information Inc.*, 2017.

[32] R. Stannarius. Magnetic resonance imaging of granular materials. *Review of Scientific Instruments Vol. 88, 051806*, 2017.

[33] I. I. Rabi. A new method of measuring nuclear magnetic moment. *Physical Review Vol. 53, 318*, 1938.

[34] A. Penn. *Real-time Magnetic Resonance Imaging of Granular Dynamics.* ETH Zurich, 2018.

[35] Y. Forterre and O. Pouliquen. Flows of dense granular media. *Annual Reviews in Fluid Mechanics Vol. 40. 1-24*, 2008.

[36] L. Sanfratello, E. Fukushima, and R. P. Behringer. Using mr elastography to image the 3d force chain structure of a quasi-static granular assembly. *Granular Matter Vol. 11:1-6*, 2008.

[37] X. Yang, C. Huan, D. Candela, R. W. Mair, and R. L. Walsworth. Measurements of grain motion in a dense, three-dimensional granular fluid. *Physical Review Letters Vol. 88*, 2002.

[38] H. Nyquist. Certain topics in telegraph transmission theory. *Transactions of the American Institute of Electrical Engineers Vol. 47, 617-644*, 1928.

[39] N. Bloembergen, E. M. Purcell, and R. V. Pound. Relaxation effects in nuclear magnetic resonance absorption. *Physical Review Vol. 73, 7*, 1948.

[40] S. K. Kwon, H. Kim, J. J. Song, C. G. Cho, S. Park, S. Choi, J. Ryu, S. H. Oh, and J. H. Lee. Vocal fold augmentation with injectable polycaprolactone microspheres/pluronic f127 hydrogel: Long-term in vivo study for the treatment of glottal insufficiency. *PLOS ONE*, 2014.

[41] J. L. Ulmer, V. P. Mathews, C. A. Hamilton, Elster A. D., and P. R. Moran. Magnetization transfer or spin-lock? an investigation of off-resonance saturation pulse imaging with varying frequency offsets. *American Journal of Dermatopathology 17:805–819*, 1996.

[42] K. P. Pruessmann, M. Weiger, M. B. Scheidegger, and P. Boesiger. Sense: Sensitivity encoding for fast mri. *Magnetic Resonance in Medicine 42:952–962*, 1999.

[43] Wenshuo Gao, Xiaoguang Zhang, Lei Yang, and Huizhong Liu. An improved sobel edge detection. In *2010 3rd IEEE International Conference on Computer Science and Information Technology (ICCSIT)*, volume 5, pages 67–71. IEEE, 2010.

[44] A. Savitzky and M. J. E. Golay. Smoothing and differentiation of data by simplified least squares procedures. *Analytical Chemistry, Vol. 36, No. 8*, 1964.

[45] R. W. Schafer. What is a savitzky-golay filter? *IEEE Signal Processing Magazine 111-117*, 2011.

[46] Vu Nguyen and Michael Blumenstein. An application of the 2d gaussian filter for enhancing feature extraction in off-line signature verification. In *2011 International Conference on Document Analysis and Recognition (ICDAR)*, pages 339–343. IEEE, 2011.

[47] Kai Briechle and Uwe D Hanebeck. Template matching using fast normalized cross correlation. In *Optical Pattern Recognition XII*, volume 4387, pages 95–103. International Society for Optics and Photonics, 2001.

[48] RE Carlson and FN Fritsch. Monotone piecewise bicubic interpolation. *SIAM journal on numerical analysis*, 22(2):386–400, 1985.

[49] Y. Madraki, S. Hormozi, G. Ovarlez, E. Guazzelli, and O. Pouliquen. Enhancing shear thickening. *Physical Review Fluids Vol. 2, 033301*, 2017.

[50] B. Liu, M. Shelley, and J. Zhang. Focused force transmission through an aqueous suspension of granules. *Physical Review Letters, Vol. 105, 188301*, 2010.